Revised version submitted to *Geochimica et Cosmochimica Acta*

# Correlated isotopic and chemical evidence for condensation origins of olivine in comet 81P/Wild 2 and in AOAs from CV and CO chondrites

Kohei Fukuda[a,*], Donald E. Brownlee[b], David J. Joswiak[b], Travis J. Tenner[c], Makoto Kimura[d], Noriko T. Kita[a].

[a] WiscSIMS, Department of Geoscience, University of Wisconsin-Madison, Madison, WI 53706, USA

[b] Department of Astronomy, University of Washington, Seattle, WA 98195, USA

[c] Chemistry Division, Nuclear and Radiochemistry, Los Alamos National Laboratory, MSJ514, Los Alamos, NM 87545, USA

[d] National Institute of Polar Research, Tokyo 190-8518, Japan

* Corresponding author.

Email: kfukuda2@wisc.edu (Kohei Fukuda)

**Abstract**

Magnesium stable isotope ratios and minor element abundances of five olivine particles from comet 81P/Wild 2 were examined by secondary ion mass spectrometry (SIMS). Wild 2 olivine particles exhibit only small variations in $\delta^{25}$Mg values from $-1.0\ ^{+0.4}/_{-0.5}$ ‰ to $0.6\ ^{+0.5}/_{-0.6}$ ‰ (2σ). This variation can be simply explained by mass-dependent fractionation from Mg isotopic compositions of the Earth and bulk meteorites, suggesting that Wild 2 olivine particles formed in the chondritic reservoir with respect to Mg isotope compositions. We also determined minor element abundances, and O and Mg isotope ratios of olivine grains in amoeboid olivine aggregates (AOAs) from Kaba (CV3.1) and DOM 08006 (CO3.01) carbonaceous chondrites. Our new SIMS minor element data reveal uniform, low FeO contents of ~0.05 wt% among AOA olivines from DOM 08006, suggesting that AOAs formed at more reducing environments in the solar nebula than previously thought. Furthermore, the SIMS-derived FeO contents of the AOA olivines are consistently lower than those obtained by electron microprobe analyses (~1 wt% FeO), indicating possible fluorescence from surrounding matrix materials and/or Fe,Ni-metals in AOAs during electron microprobe analyses. For Mg isotopes, AOA olivines show more negative mass-dependent fractionation ($-3.8 \pm 0.5‰ \leq \delta^{25}Mg \leq -0.2 \pm 0.3‰$; 2σ) relative to Wild 2 olivines. Further, these Mg isotope variations are correlated with their host AOA textures. Large negative Mg isotope fractionations in olivine are often observed in pore-rich AOAs, while those in compact AOAs tend to have near-chondritic Mg isotopic compositions. These observations indicate that pore-rich AOAs preserved their gas-solid condensation histories, while compact AOAs experienced thermal processing in the solar nebula after their condensation and aggregation. Importantly, one $^{16}$O-rich Wild 2 LIME olivine particle (T77/F50) shows negative Mg isotope fractionation ($\delta^{25}Mg = -0.8 \pm 0.4‰$, $\delta^{26}Mg = -1.4 \pm 0.9‰$; 2σ) relative to bulk chondrites. Minor element abundances of T77/F50 are in excellent agreement with those of olivines from pore-rich AOAs in DOM 08006. The observed similarity in O and Mg isotopes, and minor element abundances suggest that T77/F50 formed in an environment similar to AOAs,

probably near the proto-Sun, and then was transported to the Kuiper belt, where comet 81P/Wild 2 likely accreted.

## 1. Introduction

Particles collected from the Jupiter family comet 81P/Wild 2 (NASA Stardust mission) have provided unique opportunities to study materials from the outer Solar System, likely within the Kuiper Belt (Brownlee et al., 2006; 2012; 2014). Wild 2 particles consist of a variety of materials, including presolar grains (McKeegan et al., 2006; Messenger et al., 2009; Leitner et al., 2010, 2012) and organic matter (Sandford et al., 2006; Sandford, 2008; Matrajt et al., 2008) as well as numerous high temperature materials such as Ca, Al-rich inclusions (CAIs; e.g., McKeegan et al., 2006; Zolensky et al., 2006; Chi et al., 2009; Simon et al., 2008; Joswiak et al., 2012; 2017) and ferromagnesian silicates (Nakamura et al., 2008; Bridges et al., 2012; Joswiak et al., 2012; Nakashima et al., 2012; Ogliore et al., 2012; Frank et al., 2014; Gainsforth et al., 2015; Defouilloy et al., 2017). Determining the origins of such particles can shed light on dynamic properties of the solar protoplanetary disk, including transport and processing of comet precursors. For example, the existence of high temperature minerals in Wild 2 suggests that materials originating from the hotter inner part of the solar protoplanetary disk were transported outward to the cooler Kuiper Belt region and eventually accreted to comets (e.g., McKeegan et al., 2006; Ciesla, 2007; Nakamura et al., 2008; Brownlee et al., 2012). In addition, Nakashima et al. (2012) suggested that at least a fraction of the ferromagnesian silicates in comet Wild 2 formed in the outer regions of the asteroid belt, based on the observed similarity of oxygen isotope systematics between Wild 2 particles and chondrules from CR chondrites. Furthermore, Bridges et al. (2012) hypothesize an outer Solar System origin for some Wild 2 silicate particles that have similar oxygen isotope and elemental characteristics when compared to Al-rich chondrules from carbonaceous chondrites. Therefore, at least some Wild 2 silicate particles may

also hold information about the physicochemical conditions of the outer Solar System where comets accreted.

In the past decade, oxygen three-isotope ratios of forty-seven Wild 2 silicate particles larger than 2 μm have been acquired by secondary ion mass spectrometry (SIMS) (McKeegan et al., 2006; Nakamura et al., 2008; Nakamura-Messenger et al., 2011; Bridges et al., 2012; Nakashima et al., 2012; Ogliore et al., 2012, 2015; Joswiak et al., 2014; Gainsforth et al., 2015; Defouilloy et al., 2017; Chaumard et al., 2018), and they show a bimodal distribution on an oxygen three-isotope diagram (Fig. 1). The mass-independent fractionation of oxygen isotopes among Wild 2 particles are expressed as $\Delta^{17}O$ (= $\delta^{17}O - 0.52 \times \delta^{18}O$, where $\delta^{17,18}O$ = $[(^{17,18}O/^{16}O)_{sample}/(^{17,18}O/^{16}O)_{VSMOW} - 1] \times 1000$; VSMOW = Vienna Standard Mean Ocean Water; Baertschi, 1976), and range from –24‰ to +3‰ for all data with uncertainties smaller than 5‰. Among them, the $\Delta^{17}O$ values of thirty-six Wild 2 particles (≥ 2 μm) range from –7‰ to +3‰ (McKeegan et al., 2006; Nakamura et al., 2008; Nakashima et al., 2012; Ogliore et al., 2012, 2015; Joswiak et al., 2014; Gainsforth et al., 2015; Defouilloy et al., 2017; Chaumard et al., 2018), similar to those of chondrules found in chondrites (Tenner et al., 2018a). In contrast, seven Wild 2 particles show more $^{16}O$-rich oxygen isotopic characteristics ($\Delta^{17}O$ = –24‰ to –20‰). These seven particles are nearly pure forsterite or enstatite, some of which are low-iron, manganese-enriched (LIME) olivines and pyroxenes (Nakashima et al., 2012; Defouilloy et al., 2017; Chaumard et al., 2018). LIME olivines and pyroxenes (hereafter LIME silicates) have MnO/FeO (wt%) ratios much higher than 0.1 and low FeO contents (typically ≤ 1 wt%). As Mn is not stable as metal at solar nebula conditions, it likely condensed at ~1100 K, as $Mn_2SiO_4$ in solid solution with forsterite, and as $MnSiO_3$ with enstatite (Larimer, 1967; Wai and Wasson, 1977; Lodders, 2003). In contrast, Fe co-condenses as metal with forsterite (if the oxidation state is below the Fe-FeO buffer), meaning that high MnO/FeO ratios observed in LIME silicates suggest a condensation origin from the solar nebula (Klöck et al., 1989; Weisberg et al., 1993; 2004; Ebel et al., 2012). LIME silicates have been found in chondritic interplanetary dust particles (IDPs) (Klöck et al., 1989) that are believed to have a cometary origin (e.g., Bradley,

2003 and references therein), implying that LIME silicates may have been abundant nebular condensates and they were present in comet accretion regions. Thus, Wild 2 LIME silicates contain important clues for understanding the formation and transportation of solids in the early Solar System.

LIME silicates are also observed in amoeboid olivine aggregates (AOAs; e.g., Weisberg et al., 2004; Komatsu et al., 2015) that are the most common type of refractory inclusions in carbonaceous chondrites (e.g., Krot et al., 2004a and references therein; Sugiura et al., 2009; Ruzicka et al., 2012; Krot et al., 2014). Based on their irregularly-shaped, porous, and fine-grained textures, AOAs are thought to be aggregates of solids condensed from the solar nebula and appear to have avoided significant melting after aggregation (e.g., Grossman and Steele, 1976; Komatsu et al., 2001, 2009; Krot et al., 2004a and references therein; Weisberg et al., 2004; Sugiura et al., 2009; Han and Brearley, 2015). In addition, Mg stable isotope ratios of AOAs are indicative of a condensation origin. $\delta^{25}$Mg values of bulk AOAs (where $\delta^{25}Mg = [(^{25}Mg/^{24}Mg)_{sample}/(^{25}Mg/^{24}Mg)_{DSM\text{-}3} - 1] \times 1000$; per-mil deviation from Mg reference material DSM-3; Galy et al., 2003) range from –2.47‰ to –0.03‰ (Larsen et al., 2011; Olsen et al., 2011), some of which are negatively fractionated from those of bulk chondrites ($\delta^{25}Mg = -0.15 \pm 0.04$‰; Teng et al., 2010). In situ SIMS Mg isotope analyses of AOA olivines also show similar variations in $\delta^{25}$Mg values, as low as ~ –2.8‰ (MacPherson et al., 2012; Ushikubo et al., 2017; Marrocchi et al., 2019a). The light isotope enrichments observed in AOAs may be the result of disequilibrium condensation from solar nebula gas due to kinetic isotope fractionation (Richter, 2004). Note that AOAs from the least metamorphosed chondrites are $^{16}$O-rich ($\Delta^{17}O < -20$‰; Aléon et al., 2002; Fagan et al., 2004; Krot et al., 2004a; Itoh et al., 2007; Yurimoto et al., 2008 and references therein; Ushikubo et al., 2017; Komatsu et al., 2018). The similarities in oxygen isotope ratios and mineral chemistry (i.e., $^{16}$O-rich oxygen isotope signatures and the occurrence of LIME silicates) suggest a genetic link between Wild 2 LIME silicates and AOAs (Nakashima et al., 2012; Defouilloy et al., 2017). However, unlike AOAs, the petrological context of $^{16}$O-rich Wild 2 particles is not well understood because most particles have been found as single mineral

grains. If these particles formed by disequilibrium condensation, their Mg isotope ratios could be enriched in lighter isotopes (Richter, 2004), which could be used to trace condensation processes. Due to small particle sizes (< 10 μm), Mg isotope data from Wild 2 particles at sub-‰ precision are currently lacking, but would nonetheless be valuable for testing condensation hypotheses for $^{16}$O-rich Wild 2 particles.

Here, we report Mg three-isotope ratios and minor element concentrations of eight Wild 2 olivine particles (four that are $^{16}$O-rich and four that are $^{16}$O-depleted) in order to better understand their formation processes. To obtain high spatial resolution ( ≤ 2 μm) SIMS Mg isotope analyses, we upgraded the WiscSIMS Cameca IMS 1280 with a radio frequency (RF) plasma oxygen ion source (Hertwig et al., 2019) and applied an instrumental bias correction method that combines forsterite endmember values (= Mg/[Mg + Fe] molar %) and secondary ion $Mg^+/Si^+$ ratios (Fukuda et al., 2020). We also conducted SIMS O and Mg isotope analyses, and SIMS minor element analyses of olivine grains in AOAs from Kaba (CV3.1; Bonal et al., 2006) and the least metamorphosed CO chondrite DOM 08006 (classified as CO3.00 from Davidson et al., 2019, while we adopt CO3.01 from Fe,Ni-metal analyses of Tenner et al., 2018b), in order to compare their formation histories with those of Wild 2 particles.

## 2. Wild 2 Samples

Eight Wild 2 olivine particles were analyzed from four Stardust tracks (Track 57, 77, 149, and 175) including one particle from track 57 (T57/F10), four particles from track 77 (T77/F4, T77/F6, T77/F7, and T77/F50), two particles from track 149 (T149/F1 and T149/F11a), and one particle from track 175 (T175/F1). Secondary electron images of the eight Wild 2 olivine particles are shown in Fig. 2. Mineral chemistry and oxygen isotope ratios of these particles have been previously reported (Joswiak et al., 2012; Nakashima et al., 2012; Defouilloy et al., 2017; Chaumard et al., 2018). Oxygen isotope ratios of the eight Wild 2 particles

(Nakashima et al., 2012; Defouilloy et al., 2017; Chaumard et al., 2018) are shown in Fig. 1. Four of eight particles are $^{16}$O-rich (T57/F10, T77/F6, T77/F50, and T175/F1) while the other four particles are $^{16}$O-depleted (T77/F4, T77/F7, T149/F1, and T149/F11a). Fo contents (Fo = Mg/[Mg + Fe] molar %) of the $^{16}$O-rich particles range from 98.0 to 99.8, while $^{16}$O-depleted particles are more FeO-rich ($Fo_{60-85}$) (Joswiak et al., 2012; Defouilloy et al., 2017; Chaumard et al., 2018). Among the $^{16}$O-rich particles, T77/F6 and T77/F50 were found in the same bulbous track identified as T77 (type B track; Hörz et al., 2006; Burchell et al., 2008; Joswiak et al., 2012). It was suggested that the original projectile was a loose aggregate and that the two $^{16}$O-rich particles as well as the other $^{16}$O-rich particle in the same track (T77/F104) which are co-linearly aligned were derived from a single grain that fragmented during capture (Joswiak et al., 2012).

## 3. Analytical procedures

### 3.1. Electron microscopy

Two thin sections, Kaba USNM 1052-1 and DOM 08006, 50, were allocated from the Smithsonian Institution and NASA JSC, respectively. Backscattered electron (BSE) and secondary electron (SE) images of individual AOAs were obtained with a Hitachi S-3400 scanning electron microscope (SEM) at the University of Wisconsin-Madison (UW-Madison). Major and minor elements ($Na_2O$, MgO, $Al_2O_3$, $SiO_2$, $K_2O$, CaO, $TiO_2$, $Cr_2O_3$, MnO, and FeO) of minerals in AOAs were obtained with a Cameca SXFive FE electron-probe microanalyzer (EPMA) at UW-Madison. EPMA analyses were performed with an accelerating voltage of 15 kV and a beam current of 20 nA, with a 3 micron diameter beam. Off peak backgrounds were acquired, with 10 second counts on the background and 10 seconds on the peaks. The following reference materials (RMs) were used for olivine analyses: Burma jadeite (Na), synthetic forsterite (Mg, Si), Grass Valley anorthite (Al), NMNH 122142 Kakanui augite (Ca), microcline

(K), $TiO_2$ oxide (Ti), synthetic $Cr_2O_3$ (Cr), synthetic $Mn_2SiO_4$ (Mn), and synthetic FeO (Fe). For high-Ca pyroxene analyses, the same suite of RMs were used except for Mg and Si, which were calibrated using NMNH 122142 Kakanui augite. Probe for EPMA™ (PFE) software was used for data reduction. Calculated detection limits (99% confidence) for the measured oxides in wt% were $Na_2O$-0.02, MgO-0.02, $Al_2O_3$-0.03, $SiO_2$-0.03, $K_2O$-0.02, CaO-0.02, $TiO_2$-0.05, $Cr_2O_3$-0.07, MnO-0.05, and FeO-0.06 wt%.

Endmembers of olivine and pyroxene are expressed as Fo (= Mg/[Mg + Fe] molar %) and En (= Mg/[Mg + Fe + Ca] molar %), respectively. We also report Wo (= Ca/[Mg + Fe + Ca] molar %) as the Ca endmember for pyroxene. The Fo, En, and Wo contents were calculated by considering total iron as ferrous iron.

### 3.2. FIB marking

All Wild 2 particles studied here have been previously analyzed by SIMS for oxygen isotope ratios (Nakashima et al., 2012; Defouilloy et al., 2017; Chaumard et al., 2018) such that remaining areas for Mg isotope analyses were limited (typically 3 × 3 μm). In order to aim the primary ion beam precisely, we employed focused ion beam (FIB) marking to target areas prior to SIMS analyses (Nakashima et al., 2012; Defouilloy et al., 2017). FIB marking was performed with a field emission (FE) SEM equipped with a FIB system (Zeiss Auriga, UW-Madison), following procedures described in Defouilloy et al. (2017). After FIB marking, high-resolution SE images of all Wild 2 particles (Fig. 2 and Electronic Annex EA1) were obtained using the same instrument and were used for precise aiming of the primary ion beam.

### 3.3. Secondary ion mass spectrometry (SIMS)

Oxygen three-isotopes, Mg three-isotopes, and minor element analyses were performed with the WiscSIMS Cameca IMS 1280 equipped with the RF plasma ion source at UW-Madison. Five separate sessions (one for O isotopes, three for Mg isotopes, and one for minor elements) were conducted and analytical conditions were optimized for each session described below.

Following analytical sessions, SIMS pits were investigated by SEM (S3400 at UW-Madison) or FE-SEM (LEO 1530 at UW-Madison), of which images are shown in Electronic Annex EA1-3.

*3.3.1. SIMS oxygen isotope analyses*

For oxygen three-isotope analyses of olivine from Kaba and DOM 08006 AOAs, the primary $^{133}Cs^+$ ion beam was focused to a ~8 μm diameter spot at 0.7 nA. Secondary oxygen ions ($^{16}O^-$, $^{17}O^-$, and $^{18}O^-$) were detected simultaneously using multi-collector Faraday cups (FCs) (Kita et al., 2010). To improve precision of $\delta^{17}O$ analyses, the FC for $^{17}O^-$ employed a high gain feedback resistor ($10^{12}$ ohm) that can reduce thermal noise (Electronic Annex EA4-1). The other FCs for $^{16}O^-$ and $^{18}O^-$ employed $10^{10}$ ohm and $10^{11}$ ohm resistors, respectively. The mass resolving power (MRP) was set to ~2200 for $^{16}O^-$ and $^{18}O^-$, and 5000 for $^{17}O^-$. A single analysis took ~7 min, including 100 s of presputtering and baseline measurement, ~80 s for automated centering of secondary ion deflectors (DTFA-X, DTFA-Y), 200 s of integration (10 s × 20 cycles) of the secondary ion signals. At the end of each analysis, $^{16}O^1H^-$ was measured automatically to estimate the contribution of the tailing of $^{16}O^1H^-$ to the $^{17}O^-$ peak, which was always insignificant (<0.05‰ on $\delta^{17}O$; Electronic Annex EA4-1). A synthetic pure forsterite RM, HN-Ol ($\delta^{18}O$ = 8.90‰: Kita et al., 2010), was used as the bracketing standard. The typical secondary $^{16}O^-$ ion intensity when measuring the HN-Ol was $7.5 \times 10^8$ counts per second (cps). Ten to fifteen unknown analyses were bracketed by 8 analyses of the HN-Ol standard (4 before and 4 after the unknowns). The external reproducibility of the HN-Ol standard was typically 0.4‰, 0.9‰, and 0.9‰ (2SD) for $\delta^{18}O$, $\delta^{17}O$, and $\Delta^{17}O$, respectively. The external reproducibilities (2SD) for each bracket are assigned as the uncertainties of bracketed unknown analyses. Instrumental biases in $\delta^{18}O$ were calibrated based on the bracket HN-Ol analyses. Since all olivine grains in AOAs analyzed are near-pure forsterite ($>Fo_{99}$), no additional correction depending on Fo contents was applied.

*3.3.2. SIMS magnesium isotope analyses*

We conducted three sessions for Mg three-isotope analysis of olivine. For each session, the primary $O_2^-$ ion beam was accelerated by 23 kV (–13 kV at the ion source and +10 kV at the sample surface) to the sample surface and secondary $^{24}Mg^+$, $^{25}Mg^+$, and $^{26}Mg^+$ ions were detected simultaneously using multi-collector FCs (L′2, C, and H1). Secondary ion optics are similar to those described in Kita et al. (2012) and Ushikubo et al. (2013). The MRP at 10% peak height was set to ~2500 and contributions of $^{48}Ca^+$ and $^{24}Mg^1H^+$ to $^{24}Mg^+$ and $^{25}Mg^+$ peaks, respectively, were negligibly small (EA2 in Fukuda et al., 2020). As described below, the primary beam intensity (and size) was optimized depending on the size of unknown samples, which led to different secondary $Mg^+$ ion intensities. Therefore, the combinations of resistors for the multi-collector FCs were optimized for each session. Each analysis duration was ~8-12 min, including 100 s of presputtering, ~100 s for automated centering of the secondary ion deflectors, and ~300-500 s of integration (10 s × 30 cycles for AOA analyses and 10 s × 50 cycles for Wild 2 analyses) of secondary ion signals. The baselines of the three FC detectors were monitored during each presputtering step, and their values were averaged over eight analyses.

Data reduction procedures follow those from Ushikubo et al. (2017). Terrestrial reference $^{25}Mg/^{24}Mg$ and $^{26}Mg/^{24}Mg$ values (0.12663 and 0.13932, respectively; Catanzaro et al., 1966) were used to convert raw-measured, background-corrected ratios to delta notation ($\delta^{25}Mg_m$ and $\delta^{26}Mg_m$). The $\delta^{25}Mg$ and $\delta^{26}Mg$ matrix effects were calibrated based on analyses of ~13 olivine reference materials (RMs), of which Mg isotope ratios in DSM-3 scale (Galy et al., 2003) have been determined by solution nebulization multi-collector inductively coupled plasma mass spectrometry (SN-MC-ICP-MS) or laser ablation MC-ICP-MS (Fukuda et al., 2020). Recently, we found complex matrix effects related to SIMS Mg isotope analyses of olivine, leading to instrumental biases on $\delta^{25}Mg$ that could not be fit by a simple regression to Fo contents. Instead, we apply a calibration that uses a combination of $Mg^+/Si^+$ signal ratios and Fo contents of olivine (Fukuda et al., 2020). Specifically, instrumental biases are estimated as a function of $X = (^{24}Mg^+/^{28}Si^+)/Fo$, where $(^{24}Mg^+/^{28}Si^+)$ is the secondary ion $^{24}Mg^+/^{28}Si^+$ ratio obtained from SIMS minor element analysis (see section 3.3.3) and where Fo contents of unknown samples were

obtained with TEM-EDX (Wild 2 olivine; Joswiak et al., 2012; Nakashima et al., 2012; Defouilloy et al., 2017; Chaumard et al., 2018) or FE-EPMA (AOA olivine; this study).

Magnesium isotope ratios of unknowns are reported as $\delta^{25}Mg$ and $\delta^{26}Mg$ values in DSM-3 scale. The bias corrected $\delta^{25}Mg$ and $\delta^{26}Mg$ values are calculated as follows:

$$\delta^{i}Mg = [(1 + \delta^{i}Mg_{m}/1000)/(1 + \delta^{i}Mg_{bias}/1000) - 1] \times 1000$$

where $i$ = 25 or 26 and $\delta^{i}Mg_{bias}$ is the instrumental bias determined from the calibration curve (Electronic Annex EA5). Uncertainties in $\delta^{25}Mg$ and $\delta^{26}Mg$ are estimated by combining the analytical uncertainties and error of the fit to the instrumental bias correction. More details for the estimation of uncertainties are summarized in Electronic Annex EA5.

The mass-independent raw-measured $\Delta^{26}Mg_{m}$ is defined as $\Delta^{26}Mg_{m} = [(1 + \delta^{26}Mg_{m}/1000)/(1 + \delta^{25}Mg_{m}/1000)^{1/\beta} - 1] \times 1000$. We assume that natural and instrumental mass-dependent fractionations follow a power law function, where an applied $\beta$ value of 0.5128 was determined by vacuum evaporation experiments on melts of a Type B CAI bulk composition (Davis et al., 2015). $\Delta^{26}Mg_{m}$ values of olivine RMs obtained in the same analysis session were used to correct the non-mass dependent instrumental bias (see more details in Electronic Annex EA5). The mass-independent, bias-corrected $\Delta^{26}Mg$ of unknowns is defined as follows:

$$\Delta^{26}Mg = [(1 + \Delta^{26}Mg_{m\,(unknown)}/1000)/(1 + \Delta^{26}Mg_{m\,(RM)}/1000) - 1] \times 1000$$

where $\Delta^{26}Mg_{m\,(unknown)}$ and $\Delta^{26}Mg_{m\,(RM)}$ are $\Delta^{26}Mg_{m}$ of unknowns and $\Delta^{26}Mg_{m}$ of olivine RMs, respectively. Finally, $\delta^{26}Mg^{*}$ of unknowns are estimated as: $\delta^{26}Mg^{*} = \Delta^{26}Mg \times (1 + \delta^{25}Mg/1000)^{1/\beta}$ (Ushikubo et al., 2017). We note that natural mass-dependent fractionations in Wild 2 and AOA olivines may not follow this power law $\beta$ value, but that any potential $\delta^{26}Mg^{*}$ inaccuracy this causes is likely to be minimal. For example, if assuming kinetic Mg isotope fractionation ($\beta$ = 0.511; Young and Galy, 2004), the $\delta^{26}Mg^{*}$ of Wild 2 and AOA olivines only

298 change by a maximum of 0.03‰ within $\delta^{25}Mg$ values ranging from –3.8 to 0.6‰. This small
299 offset is well within our analytical uncertainties (~0.05-0.47‰, 2SD).
300 The Wild 2 olivine particles were analyzed in session 1 (S1; 2018 Oct). The primary $O_2^-$
301 beam was focused to 2 μm at 24 pA. All three FCs employed $10^{12}$ ohm resistors for detection of
302 $^{24, 25, 26}Mg^+$ ions. Prior to each analysis, secondary $^{25}Mg^+$ ion images of the Wild 2 olivine
303 particles were obtained by rastering the primary ion beam (24pA) over a 10 μm × 10 μm area in
304 order to identify the location of FIB marks. For this mode of operation, the secondary $^{25}Mg^+$ ions
305 were detected with a multi-collector electron multiplier (EM; L1) by applying X-deflection after
306 the secondary magnet (DSP2X), which is similar to previous techniques for oxygen and
307 magnesium isotope analyses of Wild 2 particles (Nakashima et al., 2012, 2015; Defouilloy et al.,
308 2017). One to four analyses were performed for each Wild 2 particle, bracketed by eight analyses
309 of the San Carlos olivine (hereafter SC-Ol) grains mounted in the same disks. In addition, twelve
310 other olivine RMs were measured for instrumental bias corrections (Electronic Annex EA4-2-1).
311 The typical $^{24}Mg^+$ count rate during measurement of SC-Ol was $4.6 \times 10^6$ cps. The standard
312 deviations of FC baselines over eight analyses were typically 120 cps for L′2, 90 cps for C, and
313 110 cps for H1, corresponding to $3 \times 10^{-5}$ relative to $^{24}Mg^+$ and $1.6 \times 10^{-4}$ relative to $^{25}Mg^+$ and
314 $^{26}Mg^+$ ion intensities. In this session, we estimated the time constant of each $10^{12}$ ohm feedback
315 resistor by monitoring the decay of secondary $^{24, 25, 26}Mg^+$ signals (i.e., after turning off the
316 primary beam) from SC-Ol (Electronic Annex EA4-5). The time constants of the three $10^{12}$ ohm
317 feedback resistors range from 0.49 to 0.74 seconds, which are similar to each other. Thus we did
318 not apply any tau corrections (e.g., Pettke et al., 2011). The external reproducibilities (2SD) of
319 $\delta^{25}Mg_m$, $\delta^{26}Mg_m$, and $\Delta^{26}Mg_m$ for the SC-Ol bracket standard were 0.25‰, 0.26‰ and 0.47‰,
320 respectively. The final uncertainties including error of the fit to the instrumental bias correction
321 were typically 0.58‰ 1.05‰, and 0.54‰ for $\delta^{25}Mg$, $\delta^{26}Mg$, and $\delta^{26}Mg^*$, respectively.
322 Olivine grains from Kaba AOA (K27) were analyzed in session 2 (S2; 2018 Oct). The
323 primary $O_2^-$ beam was focused to 10 μm at 2 nA. The FC for $^{24}Mg^+$ (L′2) employed a $10^{10}$ ohm
324 resistor, and the other two FCs for $^{25}Mg^+$ and $^{26}Mg^+$ (C and H1) employed $10^{11}$ ohm resistors.

SC-Ol grains were used as a bracketing standard. In addition, five Mg-rich olivine RMs (>$Fo_{94}$) listed in Electronic Annex EA4-2-2 were measured for instrumental bias corrections. The typical $^{24}Mg^+$ count rate for SC-Ol was $4.4 \times 10^8$ cps. The external reproducibilities (2SD) of $\delta^{25}Mg_m$, $\delta^{26}Mg_m$, and $\Delta^{26}Mg_m$ for the SC-Ol bracket standard were 0.08‰, 0.15‰ and 0.05‰, respectively. The final uncertainties including error of the fit to the instrumental bias correction were typically 0.31‰, 0.60‰, and 0.06‰ for $\delta^{25}Mg$, $\delta^{26}Mg$, and $\delta^{26}Mg^*$, respectively.

Olivine grains from DOM 08006 AOAs were analyzed in session 3 (S3; 2018 Dec). The primary $O_2^-$ beam was focused to ~5 μm at 160 pA. As for Wild 2 analyses, all three FCs employed $10^{12}$ ohm resistors for detection of $^{24,25,26}Mg^+$ ions. SC-Ol grains were used as a bracketing standard. An additional 11 olivine RMs, listed in Electronic Annex EA4-2-3, were measured for instrumental bias corrections. The typical $^{24}Mg^+$ count rate when measuring SC-Ol was $3.0 \times 10^7$ cps. External reproducibilities (2SD) of $\delta^{25}Mg_m$, $\delta^{26}Mg_m$, and $\Delta^{26}Mg_m$ for the SC-Ol bracket standard were 0.13‰, 0.22‰ and 0.19‰, respectively. The final uncertainties including error of the fit to the instrumental bias correction were typically 0.44‰ 0.88‰, and 0.23‰ for $\delta^{25}Mg$, $\delta^{26}Mg$, and $\delta^{26}Mg^*$, respectively.

*3.3.3. SIMS $Mg^+/Si^+$ ratios and minor element analyses*

$Mg^+/Si^+$ ratios and minor element (Ca, Cr, Mn, and Fe) concentrations were obtained using the same analytical conditions reported in Fukuda et al. (2020). Secondary $^{24}Mg^+$ ions were detected by an axial FC (FC2) with a $10^{11}$ ohm resistor. The other secondary ions ($^{23}Na^+$, $^{27}Al^+$, $^{28}Si^+$, $^{40}Ca^+$, $^{52}Cr^+$, $^{55}Mn^+$, $^{56}Fe^+$, and $^{60}Ni^+$), as well as mass 22.7 (used for stabilizing the magnetic field for $^{23}Na^+$), were detected by an axial EM that operated in magnetic peak jumping mode. Due to consumption of sample area from prior O and Mg isotope analyses of the Wild 2 olivine particles, we focused the primary $O_2^-$ beam down to 1.5 μm in diameter (6 pA) and aimed it inside the previous SIMS pits (~2 μm in diameter) from Mg isotope analyses. For AOAs from DOM 08006, the primary ion beam was also aimed inside previous SIMS pits (~5 μm in diameter) from Mg isotope analyses. Prior to each analysis, a secondary $^{24}Mg^+$ ion image of the

352 targeted SIMS pit was obtained by rastering the primary ion beam (6 pA) over a 10 × 10 μm area
353 in order to aim the primary ion beam inside the SIMS pit. The AOA (K27) from Kaba had
354 abundant areas for minor element analyses so that flat surface areas near the previous SIMS pits
355 from Mg isotope analyses were analyzed. SC-Ol grains were used as a running standard. An
356 additional 12 olivine standards (Electronic Annex EA4-3) were also measured to obtain
357 $^{24}Mg^{+}/^{28}Si^{+}$ ratios and to determine relative sensitivity factors (RSFs) of minor elements (Ca, Cr,
358 Mn, and Fe). The typical $^{24}Mg^{+}$ count rate for SC-Ol was ~$7.6 \times 10^5$ cps. We also conducted
359 multiple analyses of olivine RMs in order to compare the instrumental bias within previously
360 generated SIMS pits and flat surface areas (see more details in Electronic Annex EA5). A single
361 analysis was ~6 min in duration, including 100 s of presputtering, ~80 s for automated centering
362 of secondary ion deflectors, and 160 s of integration (32 s × 5 cycles) of secondary ion signals.
363 Detection limits were evaluated based on the measurement of synthetic pure forsterite RM (HN-
364 Ol), which is expected not to contain Ca, Cr, Mn, and Fe. The detection limits of CaO, $Cr_2O_3$,
365 MnO, and FeO were 0.002, 0.0001, 0.001, and 0.003 wt%, respectively.
366
367
368 **4. RESULTS**
369
370 **4.1. AOA petrography and mineral chemistry**
371 One AOA (K27) from Kaba and eight AOAs (501, 502, 503, 505, 511, 512, 513, and
372 514) from DOM 08006 were studied by SEM-EDS and FE-EPMA. All nine AOAs are
373 composed of forsteritic olivine, opaque minerals (Fe,Ni-metal and/or weathering products), and
374 Ca-, Al-rich portions (±spinel, ±anorthite, and Al-(Ti)-diopside). Low-Ca pyroxene is rare and
375 was identified in two out of nine AOAs (502 and 503). The mineralogical characteristics of the
376 nine AOAs are summarized in Table 1. The AOAs studied here are less than ~400 μm, except
377 for K27 from Kaba (~1.7 mm). Average elemental compositions (wt%) and Fo, En, and Wo
378 contents of AOA minerals are summarized in Table 2. Individual EPMA data and their analysis

379 locations are summarized in Electronic Annex EA4-4 and EA6, respectively. Olivine grains from
380 the nine AOAs have a narrow range of Fo content ($Fo_{99\text{-}100}$). CaO, $Cr_2O_3$, MnO, and FeO
381 contents of olivine grains vary by ~0.4, ~0.5, ~0.5, and ~1.1 wt%, respectively. As we discuss
382 later, FeO contents obtained with EPMA analyses might be overestimated due to secondary
383 fluorescence effects (e.g., Fournelle et al., 2005; Buse et al., 2018) from surrounding FeO
384 enhanced phases. En components of diopside in K27, 505, 511, and 513 range from 44.0 to 50.2.
385 $Al_2O_3$ and $TiO_2$ contents of these diopside grains range from 3.4 to 11.9 wt% and 0.2 to 2.9 wt%,
386 respectively.

387 The AOAs investigated show variations in abundances of pores, shapes of external
388 margins and ratios of minor minerals to olivine (Figs. 3-5). Three (K27, 505 and 513) show a
389 compact texture with little porosity in the forsterite-rich regions (Fig. 3). The other AOAs (e.g.,
390 502 and 503) are more porous and are irregularly shaped (Figs. 4-5). Detailed information for
391 each inclusion is summarized below.

392 AOA K27 from Kaba is the largest aggregate (~1.7 mm; Fig. 3a) studied here. It consists
393 of multiple nodules, and each nodule is composed of Ca-, Al-rich domains enclosed by sinuous
394 forsterite ($Fo_{99.5\text{-}100}$) and opaque minerals (Fig. 3b). Forsterite regions display dense textures with
395 little porosity between grain boundaries (Figs. 3b and c). Ca-, Al-rich domains have anorthite ±
396 spinel cores rimmed by Al-diopside (Fig. 3c). Spinel grains are anhedral and appear corroded by
397 the surrounding anorthite (Fig. 3c). Al-diopside occurs between anorthite and forsterite (Figs. 3b
398 and c).

399 AOA 513 from DOM 08006 (Fig. 3d) consists of multiple Ca-, Al-rich portions enclosed
400 by nearly pure forsterite grains ($Fo_{99.5\text{-}99.7}$) and rare Fe,Ni-metal. This AOA has anorthite ±
401 anhedral spinel cores rimmed by Al-diopside, which are enclosed by dense forsterite (Fig. 3e).
402 Al-diopside occurs between anorthite and forsterite (Fig. 3e). The mineralogy and texture of this
403 AOA are similar to those of Kaba AOA K27 (Figs. 3b and c).

404 AOA 505 from DOM 08006 (Fig. 3f) consists of spinel-diopside-rich nodules enclosed
405 by dense forsterite ($Fo_{99.7\text{-}99.9}$) with minor Fe,Ni-metal. This inclusion may also be classified as a

406 CAI with a thick forsterite rim. Spinel is separated from forsterite by a layer of Al-diopside (Fig.
407 3g).
408 AOA 502 from DOM 08006 is irregularly shaped and porous (Fig. 4a), consisting mostly
409 of forsterite ($Fo_{99.3-99.7}$), with minor Fe,Ni-metal and numerous irregularly shaped diffuse areas
410 (Figs. 4b-d). Rare low-Ca pyroxene is also observed (Figs. 4b and d), and forsterite regions of
411 this AOA are porous (Figs. 4b and c). SEM-EDS analyses indicate that the diffuse areas are
412 mixtures of tiny Al-diopside grains, and forsterite. Such diffuse areas are also observed in AOAs
413 from ALHA77307 (CO3.03) as brighter areas in BSE images than surrounding forsterite,
414 referred to as haloes by Sugiura et al. (2009). Forsterite grains within this AOA have the highest
415 MnO abundances (~0.5 wt%) among the nine AOAs studied here.
416 AOA 503 from DOM 08006 is a fine-grained, porous object (Fig. 4e), consisting mostly
417 of forsterite ($Fo_{99.4-99.8}$), with minor Fe,Ni-metal and numerous irregularly shaped Ca-, Al-rich
418 portions (tiny Al-diopside grains and an anorthitic halo; Fig. 4f). Rare low-Ca pyroxene is also
419 observed (Fig. 4g). The mineralogy and texture of this AOA is similar to those of AOA 502, but
420 MnO contents of forsterite grains are lower (~0.1 wt%).
421 AOA 501 from DOM 08006 (Fig. 5a) consists of forsterite ($Fo_{99.0-99.9}$), Fe,Ni-metal, and
422 numerous irregularly shaped, fine-grained Ca, Al-rich portions. Most of this AOA is composed
423 of porous forsterite with numerous irregularly shaped, fine-grained Ca, Al-rich portions (Fig.
424 5b). However, a region shown in Fig. 5c is less porous, and has nodule-like (Ca-, Al-rich core
425 and sinuous forsterite) textures, similar to characteristics observed in Kaba AOA K27 (e.g. Fig.
426 3b).
427 AOAs 511 and 512 from DOM 08006 are irregularly shaped objects (Figs. 5d and 5e,
428 respectively), consisting of forsterite ($Fo_{99.3-99.6}$), Ca-, Al-rich portions (Al-diopside and
429 anorthite), and minor Fe,Ni-metal. Ca, Al-rich diffuse areas (haloes) are observed in each AOA.
430 AOA 514 from DOM 08006 is a sub-rounded object (Fig. 5f), consisting of forsterite
431 ($Fo_{99.2-99.9}$) and irregularly shaped Ca-, Al-rich portions (Al-diopside and anorthite) that are

concentrated in the inner part of the AOA. Forsterite grains of the inner part of the AOA, along with Ca, Al-rich portions, are more porous relative to the outer regions of this AOA.

### 4.2. Oxygen isotope ratios of AOA olivines

We obtained 32 olivine oxygen isotope ratio data from eight of the nine AOAs studied here (the exception being AOA 512, due to small olivine grains). $\delta^{18}O$, $\delta^{17}O$, and $\Delta^{17}O$ values are reported in Table 3. Raw-measured O isotope ratios of AOA olivines are reported in Electronic Annex EA4-1. As shown in Fig. 6a, oxygen isotope ratios of all measured AOA olivines are $^{16}O$-rich ($\Delta^{17}O \leq -23‰$) and plot either on the Primitive Chondrule Mineral (PCM; Ushikubo et al., 2012; 2017) line or between the PCM and CCAM (Carbonaceous Chondrite Anhydrous Mineral; Clayton et al., 1977) lines. Individual olivine analyses from the eight AOAs have limited variations in $\delta^{18}O$ and $\Delta^{17}O$ values, ranging from –44.0‰ to –47.4‰ and –23.0‰ to –24.8‰, respectively. Subtle variations of oxygen isotope ratios are observed within each AOA (e.g., K27 and 514; Fig. 6a), but averaged oxygen isotope ratios of individual AOAs form a tight cluster on the PCM line (Fig. 6b), and are identical within uncertainties.

### 4.3. Magnesium isotope ratios of AOA and Wild 2 olivines

We obtained 36 olivine magnesium three-isotope ratio data from eight of the nine AOAs studied here. We did not acquire Mg isotope data from AOA 514 because large secondary deflector values (DTFA values > 50) had to be applied, and under such a condition $\delta^{25}Mg$ analyses are inaccurate due to additional instrument fractionation. Magnesium isotope ratios ($\delta^{25}Mg$ and $\delta^{26}Mg$) are listed in Table 4 and plotted in Fig. 7. Individual SIMS data including raw-measured Mg isotope ratios are reported in Electronic Annex EA4-2-6 and EA4-2-7. $\delta^{25}Mg$ values of AOA olivines range from $-3.8 \pm 0.5‰$ ($2\sigma$) to $-0.2 \pm 0.3‰$ ($2\sigma$). All Mg isotope analyses obtained in AOA olivines show a linear correlation between $\delta^{26}Mg$ and $\delta^{25}Mg$ (Fig. 7a). We also calculated logarithmic values ($\delta^{25}Mg'$ and $\delta^{26}Mg'$) that are converted from $\delta^{25}Mg$ and $^{26}Mg$ values using the following formula: $\delta^{i}Mg' = 1000 \times \ln(1 + \delta^{i}Mg/1000)$ (Electronic Annex

459 EA4-2-8). The logarithmic values are used to determine the slope and intercept in $\delta^{26}Mg'$ versus
460 $\delta^{25}Mg'$ space (Fig. 8), with values of 0.516 ± 0.012 (2σ) and –0.06 ± 0.04 (2σ), respectively
461 (using Isoplot 4.15 model 1; Ludwig, 2012). Variation in $\delta^{25}Mg$ and $\delta^{26}Mg$ within each AOA is
462 identified, which follows a line with the same slope of 0.516 (Figs. 7b-i). Among them, $\delta^{25}Mg$
463 and $\delta^{26}Mg$ values of AOA 501 are bimodally distributed on the slope 0.516 line (Fig. 7c).
464 Magnesium isotope ratios ($\delta^{25}Mg$ and $\delta^{26}Mg$) of Wild 2 olivine particles T57/F10,
465 T77/F4, T77/F50, T149/F1, and T175/F1 are listed in Table 5 and plotted in Fig. 9. Difficulties
466 with the analyses of three Wild 2 particles (T77/F6, T77/F7, and T149/F11a) or data reduction
467 problems prevented the reporting of bias-corrected $\delta^{25}Mg$ and $\delta^{26}Mg$ values. For analyses of
468 T77/F6 and T77/F7, ($Mg^+/Si^+/Fo$) values of these particles are outside the range of the
469 instrumental fractionation calibration curve, meaning we could not properly correct data for
470 instrumental mass fractionation. For T149/F11a, we observed that the Mg ion yields and $\delta^{25}Mg_m$
471 values changed significantly during the analysis. These changes were not observed among
472 olivine RM analyses, meaning we could not properly correct data for instrumental mass
473 fractionation. More detailed explanations for these three particles can be found in Electronic
474 Annex EA7. All individual data, including raw-measured Mg isotope ratios of the eight Wild 2
475 particles, are reported in Electronic Annex EA4-2-5. Regarding the five Wild 2 particles for
476 which Mg isotope ratios were successfully determined, they show slight variations in $\delta^{25}Mg$,
477 ranging from $-1.0\ ^{+0.4}/_{-0.5}$‰ (2σ) to $0.6\ ^{+0.5}/_{-0.6}$‰ (2σ). The Mg isotopic data from these five
478 Wild 2 particles fall on the same slope 0.516 line that is defined by individual AOA olivines
479 (Fig. 9). Particles T77/F50 and T149/F1 were analyzed multiple times (N = 3 and N = 4,
480 respectively) and do not show intra-grain variations in $\delta^{25}Mg$ and $\delta^{26}Mg$ values beyond
481 uncertainties (Table 5 and Fig. 9).
482 $\delta^{26}Mg^*$ values of AOA olivines and Wild 2 olivines are reported in Tables 4 and 5, and
483 are plotted against their $\delta^{25}Mg$ values in Fig. 10. $\delta^{26}Mg^*$ values of AOA olivines from Kaba and
484 DOM 08006 range from –0.15 ± 0.25‰ (2σ) to 0.17 ± 0.24‰ (2σ) and do not show resolvable
485 excesses in $^{26}Mg$ when compared to inferred Solar System initial $\delta^{26}Mg^*$ values (–0.040‰;

Jacobsen et al., 2008 or –0.016‰; Larsen et al., 2011). $\delta^{26}Mg^{*}$ values of Wild 2 olivines range from –0.41 ± 0.76‰ (2σ) to 0.31 ± 0.37‰ (2σ) and do not show resolvable excesses in $^{26}Mg$.

### 4.4. Minor element abundances of AOA and Wild 2 olivines obtained with SIMS

CaO, $Cr_2O_3$, MnO and FeO contents in AOA and Wild 2 olivines were determined with a spatial resolution of ~1.5 μm by SIMS (Tables 4 and 5). Olivines from Kaba and DOM 08006 AOAs show one or two orders of magnitude variation in CaO, $Cr_2O_3$, and MnO contents ranging from 0.03 to 0.28 wt%, 0.06 to 0.32 wt%, and 0.004 to 0.31 wt%, respectively. FeO contents in olivines from DOM 08006 AOAs do not show significant variation among the seven examples investigated (0.03-0.08 wt%; Fig. 11). In contrast, olivines from Kaba AOA K27 are more variable (0.06-0.58 wt%) than DOM 08006 AOAs (Fig. 11). MnO/FeO (wt%) ratios of 38 olivine analyses show a large variation (0.1-4.2) even within a single inclusion (e.g., 0.1-2.1 in AOA511; see Table 4).

CaO, $Cr_2O_3$, and MnO contents in five Wild 2 olivine particles (T57/F10, T77/F4, T77/F50, T149/F1, and T175/F1) range from 0.004 to 0.19 wt%, 0.07 to 0.53 wt%, and 0.06 to 0.66 wt%, respectively. The $^{16}O$-depleted, FeO-rich Wild 2 olivines (T77/F4 and T149/F1) have higher CaO contents (0.12-0.19 wt%) than the $^{16}O$-rich, FeO-poor Wild 2 olivines (0.004-0.04 wt%). The MnO/FeO (wt%) ratio of $^{16}O$-rich olivine from T77/F50 is 3.8, is consistent with LIME olivine (Klöck et al., 1989). The MnO/FeO (wt%) ratios of the other $^{16}O$-rich olivines (T57/F10 and T175/F1) are 0.38 and 0.37, respectively. $^{16}O$-depleted Wild 2 olivines T77/F4 and T149/F1 have very low MnO/FeO ratios (≤0.03) due to their abundant FeO contents.

## 5. DISCUSSION

### 5.1. Distribution of O isotopes at the AOA-forming regions

Ushikubo et al. (2017) conducted O isotope analyses of individual AOA minerals from the Acfer 094 (C-ungrouped 3.00) carbonaceous chondrite and observed subtle variations in O isotope ratios along slope ~1 lines (CCAM and PCM). Some AOA olivines studied here show similar detectable variability (Fig. 6a), indicating slight oxygen isotope variation of early solar nebular gas (Ushikubo et al., 2017). However, these variations are very small compared to the differences between O isotope ratios of AOAs and more $^{16}$O-depleted objects (e.g., chondrules). In fact, the averaged O isotope ratios of individual AOAs from Kaba and DOM 08006 cannot be distinguished from each other (Fig. 6b). Those of AOAs from Acfer 094 (Ushikubo et al., 2017) also plot within the range of Kaba and DOM 08006 AOAs (Fig. 6b). These observations indicate that AOAs from Kaba, DOM 08006, and Acfer 094 formed in a single $^{16}$O-rich gaseous reservoir (average $\Delta^{17}O = -23.9 \pm 0.5$‰; 2SD; N = 12; Ushikubo et al., 2017 and this study), probably near the proto-Sun (Krot et al., 2004) and were transported to accretion regions of each chondrite parent body.

In addition to AOAs, O isotope ratios of fine-grained CAIs from type 3.00-3.05 chondrites as well as spinel-hibonite inclusions (SHIBs) from CM chondrites are distributed between the CCAM and PCM lines with limited variations in $\Delta^{17}O$ from –24‰ to –22‰ (Kööp et al., 2016; Ushikubo et al., 2017). Regarding $\Delta^{17}O$ values, CAIs from the least metamorphosed CO and CR chondrites also exhibit consistently $^{16}$O-rich isotope characteristics ($\Delta^{17}O \leq -20$‰; Makide et al., 2009; Bodénan et al., 2014; Simon et al., 2019; Zhang et al., 2020). The O isotope similarity among refractory inclusions from thermally unmetamorphosed chondrites suggests that they formed in a homogeneously $^{16}$O-rich reservoir.

### 5.2. Distribution of Mg isotopes at the AOA- and Wild 2 olivine-forming regions

We observe large variation in Mg isotopes of AOA olivine (Fig. 7). Other types of refractory inclusions (i.e., CAIs) also exhibit isotopic variations in multiple elements, including Mg (e.g., Liu et al., 2009; Wasserburg et al., 2012; MacPherson et al., 2017; Park et al., 2017), which are sometimes attributed to nucleosynthetic anomalies. However, a nucleosynthetic origin

for the negative $\delta^{25}Mg$ and $\delta^{26}Mg$ values observed in AOA olivine seems unlikely because these values are linearly correlated with each other (Fig. 7), with a slope of ~0.5. Instead, this correlation is most likely the result of mass-dependent isotope fractionation. Based on theoretical studies, equilibrium and kinetic mass-dependent processes have different slopes in $\delta^{26}Mg'$ versus $\delta^{25}Mg'$ space (0.521 and 0.511, respectively; Young and Galy, 2004; Davis et al., 2015). The slope of the mass-dependent fractionation observed in the AOA olivines studied here (0.516 ± 0.012, 2σ; Fig. 8) is in between these expected slopes, and therefore cannot be distinguished as being the result of an equilibrium or kinetic process.

Teng et al. (2010) conducted Mg isotope analyses of 38 chondrites which show indistinguishable ratios ($\delta^{25}Mg = –0.15 \pm 0.04‰$, $\delta^{26}Mg = –0.28 \pm 0.07‰$, 2SD). In this study, the Mg isotope regression for AOA olivines is $\delta^{25}Mg' = (–0.06 \pm 0.04) + (0.516 \pm 0.012) \times \delta^{26}Mg'$ (Fig. 8). If using the $\delta^{26}Mg'$ value of bulk chondrites (Teng et al., 2010) in this formula, the calculated $\delta^{25}Mg'$ is –0.20 ± 0.04‰ (95% confidence limit), which is indistinguishable from that of the bulk chondrites within their uncertainties. This suggests that AOA olivines originated from a reservoir with a chondritic Mg isotope ratio.

Five Wild 2 particles show resolvable variability in Mg isotope ratios (Fig. 9). All Wild 2 olivine analyses fall on a mass-dependent fractionation line defined by individual AOA analyses (Fig. 9), suggesting Wild 2 olivine particles also derived from a chondritic Mg isotope reservoir. While uncertainties from comet particles are relatively larger, our data demonstrate for the first time that Mg isotopes are in agreement between Wild 2 comet olivine particles and other known Solar System solids.

### 5.3. Origin of AOAs: Condensation and thermal processing in the solar protoplanetary disk

#### 5.3.1. Variations in texture among AOAs

Earlier studies have hypothesized a condensation origin for AOAs based on textural and mineralogical signatures (Krot et al., 2004a and references therein). The porous and irregular shapes of some AOAs indicate that they are aggregates of olivine grains and were never completely molten (e.g., Grossman and Steele, 1976; Krot et al., 2004a and references therein). Also, the presence of silica in an AOA from the Yamato-793261 (CR) is indicative of gas-solid condensation (Komatsu et al., 2018). The AOAs studied here show textural variations (Figs. 3-5), allowing for interpreting their origins. Three of them (K27, 505 and 513) have a compact texture with little porosity in their forsterite portions (Fig. 3), similar to "compact AOAs" from Yamato-81020 (CO3.05) (Sugiura et al., 2009). In contrast, AOAs 502 and 503 are porous, irregularly shaped objects (Fig. 4), similar to "porous AOAs" reported in Sugiura et al. (2009). Compact and porous AOAs are found in other types of carbonaceous chondrites (e.g., Krot et al., 2004a; Weisberg et al., 2004; Ruzicka et al., 2012; Rubin, 2013; Krot et al., 2014; Han and Brearley, 2015; Komatsu et al., 2015), suggesting this textural variation is a general characteristic among AOAs. From our observations, we categorize the nine AOAs investigated here into two types of AOAs; (1) three AOAs, K27, 505, and 513 are categorized as compact AOAs, as they have almost no pores and show a concentric texture with spinel and/or anorthite at the core → Al-diopside → forsterite (Figs. 3c, e, g); and (2) those with pore-rich, irregular-shaped, ±fine-grained textures are categorized as pore-rich AOAs (501, 502, 503, 511, 512, 514; Figs. 4-5). Spinel grains are observed in compact AOAs, but are not present in pore-rich AOAs of this study. Conversely, diffuse Ca-Al-rich haloes are observed in pore-rich AOAs, but are not a feature of compact AOAs. Moreover, the pores within pore-rich AOAs have polygonal outlines (e.g., Figs. 4b-d and 4f-g), suggesting these AOAs avoided melting (Han and Brearley, 2015).

Many AOAs do not appear to be the result of simple condensation (e.g., Komatsu et al., 2009; 2015). As shown in Fig. 3, compact AOA olivines have low porosity textures, indicating that they experienced high-temperature annealing after their condensation and aggregation (e.g., Krot et al., 2004a; Sugiura et al., 2009; Komatsu et al., 2009; Han and Brearley, 2015). In addition, compact AOAs K27 and 513 contain 5-10 μm size anorthite that is rimmed by 5-10 μm

592 thick Al-diopside, which is in turn rimmed by olivine grains (Figs. 3c and 3e). This texture is not
593 consistent with a sequence that is predicted by equilibrium condensation calculations (Petaev and
594 Wood, 2005). Komatsu et al. (2009) performed heating experiments on mineral assemblages
595 similar to those of AOAs and suggested that Al-diopside in AOAs can be produced from a small
596 degree of melting of forsterite and anorthite. Based on the compact texture and the occurrence of
597 Al-diopside between forsterite and anorthite (Figs. 3c and 3e), it appears that some AOAs
598 experienced high-temperature annealing.
599 Similar occurrences of Al-diopside between forsterite and anorthite are also found among
600 pore-rich AOAs (e.g., Figs. 5b-c), but at much finer scales. In addition, minor low-Ca pyroxenes
601 are found in two pore-rich AOAs (502 and 503), which occur with Fe,Ni-metal (Figs. 4b, 4d,
602 4g). Similar textural occurrences of low-Ca pyroxene are present in AOAs from CR chondrites
603 (Krot et al., 2004b). The existence of low-Ca pyroxene suggests interaction with gaseous SiO or
604 direct condensation (Krot et al., 2004b). These observations indicate that some pore-rich AOAs
605 have also experienced high-temperature annealing, although to a smaller degree relative to
606 compact AOAs.
607
608 **5.3.2. Variations in minor element abundances among AOAs**
609 Among the AOAs investigated there is an inconsistency in FeO contents determined by
610 EPMA versus SIMS (Fig. 11). Previous studies employing EPMA found that AOA olivines from
611 the least metamorphosed chondrites have detectable FeO (~1 wt%; e.g., Krot et al., 2004a;
612 Weisberg et al., 2004; Itoh et al., 2007; Sugiura et al., 2009; Komatsu et al., 2015; 2018), most of
613 which are more enriched than concentrations predicted by equilibrium condensation calculations
614 (e.g., ~0.14 wt% at a total pressure of $10^{-4}$ bar and with a dust enrichment factor of 1 (nominal
615 solar composition); Sugiura et al., 2009). The enrichment in FeO suggests condensation of
616 olivine at more oxidizing conditions (= high dust/gas ratios) (e.g., Komatsu et al., 2015; 2018).
617 Our FE-EPMA-derived FeO contents from AOA olivines are variable (~0.05-1 wt%; open
618 symbols in Fig. 11), with some values that are also much higher than that predicted by Sugiura et

al. (2009). In contrast, our SIMS data reveal uniform olivine FeO contents of ~0.05 wt% among the AOAs studied (with a few exceptions for Kaba AOA K27; Fig. 11), which is consistent with equilibrium condensation calculations with a nominal solar composition gas from Sugiura et al. (2009). The uniform olivine FeO contents suggest that AOA olivine formed at more reducing conditions than previously thought. As higher FeO is mostly observed in porous AOAs, Sugiura et al. (2009) pointed out the possibility of contributions from FeO-bearing matrix materials during olivine EPMA analyses. Our present results also indicate that FeO contents of AOA olivine determined by EPMA analyses tend to be influenced by fluorescence from surrounding matrix materials and/or Fe,Ni-metals in AOAs, and that this may result in an overestimation of FeO contents and in an underestimation of MnO/FeO ratios in AOA olivine. The similar problem on EPMA analyses has also been pointed out by Wasson et al. (1994), who demonstrated that FeO contents in enstatite grains separated from EL6 meteorite chips are an order of magnitude lower than those in meteorite thin sections, suggesting a secondary fluorescence and/or double backscattering of electrons from surrounding opaque minerals. Therefore, we only refer to minor element abundances, including FeO contents, obtained by SIMS in the following discussion.

In Figure 12 CrO and MnO contents from SIMS olivine analyses are plotted as functions of CaO (Figs. 12a-b) and FeO (Figs. 12c-d), along with predicted values from Sugiura et al. (2009). Here we use CrO contents instead of $Cr_2O_3$ to compare SIMS data and predicted values from Sugiura et al. (2009). Generally, CrO (and possibly MnO) contents of AOA olivine are anti-correlated with CaO contents (Figs. 12a-b). Some olivines in pore-rich AOAs are enriched in Cr and Mn and are depleted in Ca relative to those in compact AOAs, but ~70% plot within a narrow range (CaO ~0.05-0.2 wt%; Figs. 12a-b). The correlations between textures and volatility controlled elemental abundances of AOAs are consistent with observations from Sugiura et al. (2009) and Komatsu et al. (2015), and indicate that compact AOAs are more refractory than pore-rich AOAs. As shown in Figs. 12c-d, plots of MnO and CrO versus FeO contents in AOA olivine are similar to those predicted by condensation models with a dust enrichment factor of 1 (nominal solar composition), except for some Kaba K27 AOA data. While all DOM 08006 data

646 show a limited range in FeO contents regardless of their textural variations (compact versus
647 pore-rich), it is possible that some Kaba AOA olivines were influenced by parent body alteration,
648 leading to subtle Fe addition. Using data from DOM 08006 alone, we find CrO, MnO, and FeO
649 compositions of AOA olivine are slightly offset, but broadly consistent with the condensation
650 paths calculated by Sugiura et al. (2009) (Figs. 12c-d). In contrast, when CrO and MnO are
651 plotted against CaO (Figs. 12a-b), they are clearly offset from the condensation paths, which is
652 similar to AOA data reported in Sugiura et al. (2009). These relationships could be the result of
653 two possibilities: (1) equilibrium condensation with lower dust/gas ratios (dust enrichment factor
654 < 1), or (2) disequilibrium condensation of AOA olivine. In the case of (1), the condensation
655 paths in Figs. 12c-d could be shifted to a lower side with respect to FeO contents (X-axis)
656 because disk environments with very low dust/gas ratios could have resulted in lower FeO
657 contents of condensed olivine without significant changes in MnO and CrO contents (Sugiura et
658 al., 2009; Komatsu et al., 2015). However, even in environments with lower dust/gas ratios, CaO
659 contents in AOA olivine may not be significantly reduced when compared to those predicted
660 from condensation calculations (Figs. 12a-b). In the case of (2), disequilibrium condensation
661 could explain low concentrations of CaO relative to those predicted from a model condensation
662 path. In the temperature range of equilibrium olivine condensation (e.g., 1300-1370 K at $10^{-4}$ bar
663 with a dust enrichment factor of 1), most Ca is predicted to be consumed by the formation of Ca-
664 Al-rich minerals that do not remain in the gas phase (Sugiura et al., 2009). Thus, if AOA olivine
665 condensed from the gas phase and was never equilibrated with pre-existing Ca-Al-rich minerals,
666 CaO contents in olivine would be lower than those expected by equilibrium condensation. In
667 contrast, Mn and Cr would have been largely in the gas phase, such that MnO and CrO
668 abundances versus CaO contents in AOA olivine would plot parallel to the equilibrium
669 condensation trajectories (Figs. 12a-d). Therefore, the observed offsets from condensation paths
670 indicate that AOAs formed by disequilibrium condensation.
671
672 **5.3.3. Kinetic isotope fractionation during condensation**

673 During condensation, mineral phases can become enriched in light isotopes due to
674 disequilibrium effects. For example, Richter (2004) modeled Mg isotope fractionation during
675 condensation and demonstrated that Mg isotopes of the condensate are enriched in lighter
676 isotopes when the ambient temperature changes faster than the condensation timescale. In this
677 condition, the pressure of Mg gas is greater than its saturation vapor pressure, which facilitates
678 disequilibrium condensation. This supersaturated condition could produce condensates enriched
679 in lighter isotopes.
680 Fig. 13a shows $\delta^{25}$Mg values for individual olivines from AOAs with different textures
681 (compact versus pore-rich). Compact AOAs are more limited in $\delta^{25}$Mg values (–1.2‰ to
682 chondritic), while pore-rich AOAs exhibit greater variability (–3.8‰ to chondritic). As pore-rich
683 AOAs may have experienced limited post-formation annealing, their larger and more negative
684 $\delta^{25}$Mg variations may have been caused by disequilibrium condensation processing. As
685 discussed earlier, variations of trace element abundances in AOA olivine suggest they are
686 controlled by volatility even though concentrations do not exactly follow equilibrium
687 condensation trajectories. The $\delta^{25}$Mg values in pore-rich AOA olivine correlate positively with
688 CrO and negatively with CaO contents, respectively (Figs. 13b and c), which could represent a
689 condensation trajectory in a cooling nebula gas.
690 A similar positive correlation between $\delta^{25}$Mg and MnO concentration is expected, but is
691 not clearly seen in Fig. 13d. Most AOAs have MnO contents < 0.1wt% and a large range of
692 $\delta^{25}$Mg. Equilibrium condensation calculations by Sugiura et al. (2009) predict that condensation
693 of Mn into olivine should occur at a lower temperature than Cr, and that the increase of MnO
694 with decreasing temperature is steeper than that of CrO (see Fig. 2 in Sugiura et al., 2009). If the
695 cooling rate is faster than the equilibrium condensation timescale (i.e., disequilibrium
696 condensation), and if the temperature is within the range of Mn condensation, Mn will not
697 sufficiently condense into olivine. Thus, relatively lower MnO contents are consistent with
698 kinetic mass-dependent isotope fractionation of Mg, due to supersaturated conditions during
699 condensation of olivine.

Isotope fractionation of condensing forsterite has been modeled as functions of the condensation temperature and timescale parameter $\varepsilon$ by Richter (2004),

$$\varepsilon = \frac{\tau_{cond}}{\tau_T} = \frac{\lambda_T V_c \rho_i \eta^{-\frac{1}{3}}}{A J_{i,0}} \quad (1)$$

where $\tau_{cond}$ and $\tau_T$ are timescales for condensation and for ambient temperature change, respectively, $V_c$ is the volume of the condensed phase, $\rho_i$ is the molar density of $i$ in the condensed phase, $A$ is the surface area, and $J_{i,0}$ is the free evaporation rate at a specified temperature and pressure. The timescale of $\tau_T$ is an inverse of the cooling rate $\lambda_T = -(1/T)dT/dt$. As expected by this relationship, when the cooling rate is much faster than the timescale for condensation (i.e., larger $\varepsilon$ value), it induces disequilibrium condensation and large isotopic fractionation by partial condensation. As a first approximation, the condensation temperature of AOA olivine is estimated by comparing the CrO content and the equilibrium condensation calculations at a total pressure of $10^{-4}$ bar and a dust enrichment factor of 1 (Sugiura et al., 2009). Fig. 14 shows $\delta^{25}$Mg values of AOA olivines as a function of the estimated condensation temperatures, which are compared to the $\delta^{25}$Mg trajectories during disequilibrium condensation modeled by Richter (2004). Since olivine crystallization would occur during disequilibrium condensation rather than during equilibrium condensation, the predicted temperatures are systematically higher than the actual temperatures depending on the extent of disequilibrium condensation. While there are uncertainties in our temperature estimates, pore-rich AOA olivine data are distributed between the two model disequilibrium condensation trajectories with $\varepsilon$ = 0.001 and 0.01, respectively (Fig. 14). The negative correlation among most pore-rich AOA data (except for two AOA 501 analyses) are in agreement with a small range of $\varepsilon$, suggesting that variations in $\delta^{25}$Mg values result from differences in the condensation temperature at a fairly constant cooling rate. Note that the isotopic fractionation calculations by Richter (2004) were done at a total pressure of $10^{-3}$ bar, which is one order of magnitude higher than that of the

condensation calculation by Sugiura et al. (2009) that we use to estimate condensation temperatures. The total pressure influences the parameter $J_{i,0}$ in Eq. (1) (see Richter, 2004 for more details), and decreases it by a factor of 3 when the total pressure is lowered by $10^{-1}$ bar; in turn, this leads to increase $\varepsilon$ by a factor of 3. Thus, it does not significantly affect our conclusion.

**5.3.4. Effect of high-temperature annealing**

If AOAs experienced high-temperature annealing in the solar nebula, Mg isotope signatures and correlated minor element concentrations that are seen in pore-rich AOA could have been modified from their primary values. At high temperatures, Cr could be lost and Mg isotope ratios could have exchanged with ambient gas (e.g., Solar $\delta^{25}$Mg ~0). Also, as a result of the presence of Ca-Al-rich phases in AOAs, Ca would likely have diffused into olivine (Sugiura et al., 2009). Such processes could have modified $\delta^{25}$Mg values of AOA olivine, making them negatively correlated with CrO and positively correlated with CaO. However, this is not observed for the AOA data in this study (Figs. 13b-c). In particular, the diffusivity of Cr in forsterite varies with Cr concentration, oxygen fugacity, and silica activity ($a_{SiO2}$) (Jollands et al., 2018). At the onset of olivine condensation (1370K at a total pressure of $10^{-4}$ bar and a dust enrichment factor of 1; Sugiura et al., 2009), the Cr diffusion rate in forsterite (along the c axis) ranges from $1 \times 10^{-18}$ to $2 \times 10^{-16}$ $m^2/s$ (Jollands et al., 2018), which is faster than the Mg diffusion rate in forsterite ($5 \times 10^{-19}$ $m^2/s$; Chakraborty, 2010). Hence, high-temperature annealing would likely have resulted in the loss of Cr from olivine before Mg isotopes exchanged with ambient gas. Thus, the positive correlation between $\delta^{25}$Mg and CrO contents in pore-rich AOAs (Fig. 13b) suggest that high-temperature annealing did not significantly modify the Mg isotope and chemical signatures of pore-rich AOAs, a finding which is consistent with textural observations, such as irregular shapes of these AOAs. Additionally, Ca diffusion in forsterite is comparable with that of Mg ($1 \times 10^{-19}$ $m^2/s$ at 1370 K along the c axis; Morioka, 1981; Coogan et al., 2005) meaning that the inverse relationship between $\delta^{25}$Mg and CaO

752 contents (Fig. 13c) also supports a conclusion that Mg isotope characteristics of pore-rich AOAs
753 have not been modified by annealing.
754 As previously mentioned, a positive correlation between $\delta^{25}$Mg and MnO contents (or
755 MnO/FeO ratios) is not apparent (Figs. 13d-e), which is likely the result of disequilibrium
756 condensation. Alternatively, high-temperature annealing could lead to a loss of Mn from olivine
757 grains. If this is the case, MnO contents as well as MnO/FeO ratios of some AOAs might have
758 been modified during the annealing. However, the Mn diffusion rate in forsterite, which is
759 influenced by oxygen fugacity and silica activity, ranges from $3 \times 10^{-20}$ to $1 \times 10^{-17}$ $m^2/s$ at 1370
760 K along the c axis (Jollands et al., 2016). This is similar to or slightly lower than the Mn-Mg
761 inter-diffusion rate, which was determined by Morioka (1981) to be $4.2 \times 10^{-17}$ $m^2/s$ at 1370 K
762 along the c axis. Therefore, low MnO contents of pore-rich AOAs might not be caused by loss of
763 Mn during high-temperature annealing.
764
765 **5.3.5. Formation of compact AOAs**
766 As mentioned above, $\delta^{25}$Mg values of compact AOAs are nearly uniform (Fig. 13a),
767 indicating partial isotope exchange with ambient gas during high-temperature annealing. Sugiura
768 et al. (2009) proposed that compact AOA textures resulted from either annealing of pre-existing
769 AOAs in the solar nebula or by slow cooling during condensation. Both hypotheses are
770 consistent with the $\delta^{25}$Mg uniformity in compact AOAs. If the former is the case, the duration of
771 annealing would likely have been much longer than that for pore-rich AOAs, and may have
772 induced Mg isotope exchange between AOA olivine and ambient gas. If the latter is the case, the
773 cooling rate of compact AOAs would have been sufficiently slower than that of pore-rich AOAs
774 (i.e., smaller $\varepsilon$ value). Such slow cooling could achieve near-equilibrium condensation, which
775 would suppress isotopic fractionation during condensation (e.g., dotted line, Fig. 14). This
776 scenario is also consistent with the observed uniformity in compact AOA olivine $\delta^{25}$Mg (Fig.
777 14). However, as discussed above, the mineralogical sequence observed in compact AOAs is
778 inconsistent with an equilibrium condensation sequence (Petaev and Wood, 2005; Komatsu et

al., 2009). In addition, minor element systematics in AOA olivines cannot be simply explained by equilibrium condensation (e.g., Fig. 12a). Therefore, long-term, high-temperature annealing of pre-existing AOAs appear to be the most likely scenario to explain the chemical, textural, and Mg isotopic signatures among compact AOAs, consistent with the conclusion of previous studies (e.g., Komatsu et al., 2001; Krot et al., 2004a; Han and Brearley, 2015; Marrocchi et al., 2019a). Regarding O isotope ratios, we do not find a resolvable difference between compact and pore-rich AOAs (Fig. 6b), suggesting that (1) the annealing process did not modify the O isotope ratios because of its slower diffusion rate than Mg (Ando et al., 1981), and/or (2) the annealing process occurred at $^{16}$O-rich environments similar to where pore-rich AOAs condensed.

One pore-rich AOA, 501 from DOM 08006, exhibits a bimodal distribution on a Mg three-isotope plot (Fig. 7c). The irregularly shaped Ca-Al-rich portions and abundant pores (Fig. 5b) indicate that the majority of this AOA has not experienced extensive annealing like compact AOAs. However, two Mg isotope analyses for AOA 501 do not follow the condensation trend observed in pore-rich AOAs (Figs. 13b-c), making it difficult to explain the $\delta^{25}$Mg variation in AOA 501 by a simple condensation process. The near-chondritic $\delta^{25}$Mg values are found only in the outer left portion of the AOA, which has a compact texture (SIMS pits #1 and #5 in Fig. 5c) compared to rest of the AOA (Fig. 5b). Thus, it is possible that Mg isotope ratios of the compact textured region exchanged with ambient gas during annealing. Porous and compact textures have also been found in a single AOA from Adelaide (ungrouped C), which does not show evidence for melting (AOA #34b; Krot et al., 2004b). This AOA mainly consists of porous forsterite regions with very fine-grained anorthite and Al-diopside, and these domains are surrounded by compact forsterite rims (see Fig. 4d in Krot et al., 2004b). As shown in Fig. 5c, Ca-Al-rich phases in the outer left part of the AOA 501 are concentrated centrally in this region, similar to nodules in compact AOA K27 (Fig. 3b). Note that, however, an analysis of the outer right portion of the AOA (location #7 in Electronic Annex EA3) reveals a negative Mg isotope ratio ($\delta^{25}$Mg = –3.1 ± 0.4‰; 2σ), meaning there is no systematic relationship between analysis locations and $\delta^{25}$Mg values in AOA 501. Furthermore, CrO contents of inner and outer regions

806 are similar to each other. Since Cr diffusion rate in forsterite is faster than the Mg diffusion rate
807 in forsterite, the similar CrO contents in both inner and outer regions may not support the Mg
808 isotope exchange with ambient gas during annealing. Similarly, we did not observe notable
809 differences in minor element abundances and oxygen isotope ratios among AOA 501 (Table 3
810 and 4).
811 Recently, Marrocchi et al. (2019a) conducted SIMS oxygen, magnesium, and silicon
812 isotope analyses of AOA olivine from Kaba (CV3.1), NWA 5958 (ungrouped C2, CM-like), and
813 MIL 07342 (CO3.0-3.2) and found large negative Si isotope fractionations in AOA olivine
814 (down to –5‰/amu). In contrast, Mg isotope ratios of these AOA olivines are near-chondritic to
815 positively fractionated (~2‰ in $\delta^{25}$Mg). Based on a model involving the condensation of olivine,
816 they concluded that AOA olivines formed by rapid condensation (~days to weeks) followed by
817 Mg isotope homogenization during thermal annealing that did not affect primary Si isotope
818 ratios, due to much lower diffusion rates of Si than Mg (Chakraborty, 2010). The textures of
819 these AOAs indicate they are similar to compact AOAs in our study and their near-chondritic
820 Mg isotope data are also generally consistent with this study. However, most $\delta^{25}$Mg values
821 reported in Marrocchi et al. (2019a) are slightly positively fractionated from the chondritic Mg
822 isotopic compositions, which is not observed in this work, indicating that some AOAs
823 experienced partial evaporative loss of Mg during annealing. Alternatively, this difference
824 between datasets could be the result of complex matrix effects for SIMS Mg isotope analyses of
825 olivine (Fukuda et al., 2020). Marrocchi et al. (2019a) also mentioned “complex” matrix effects
826 on Mg isotope analyses, though they did not use the correction scheme employed here. Our
827 preliminary results, that are calibrated using only Fo contents, also show slight positive $\delta^{25}$Mg
828 values of some AOA olivines (Fukuda et al., 2019a), similar to the results from Marrocchi et al.
829 (2019a). Therefore, a component of the observed positive fractionations in AOA olivine from
830 Marrocchi et al. (2019a) could be due to inaccurate corrections of SIMS matrix effects. For
831 example, when we apply our new calibration method, that combines Fo contents and $Mg^+/Si^+$
832 ratios, $\delta^{25}$Mg values do not show positive values, but instead range from –4‰ to bulk chondritic

Mg isotope ratios (Fig. 7). These $\delta^{25}$Mg values are in good agreement with $\delta^{29}$Si values of AOA olivine ($-5‰ < \delta^{29}Si < 0‰$) determined by Marrocchi et al. (2019a). This comparison is significant because similar $\delta^{25}$Mg and $\delta^{29}$Si values are predicted from theoretical calculations of isotope fractionation during disequilibrium condensation of olivine (Marrocchi et al., 2019a), supporting our conclusion that the pore-rich AOAs studied here preserved their primary condensation Mg isotopic fractionation characteristics.

### 5.4. Origin of $^{16}$O-rich Wild 2 olivine particles

Three Wild 2 particles studied here, T57/F10, T77/F50, and T175/F1, are forsteritic olivines (> $Fo_{98}$) with $^{16}$O-rich signatures (Nakashima et al., 2012; Defouilloy et al., 2017; Chaumard et al., 2018). TEM-EDX analyses revealed that one of the particles, T77/F50 is LIME olivine ($Fo_{99.8}$; Joswiak et al., 2012), which was confirmed by our SIMS-derived MnO/FeO (wt%) ratio of this particle ($3.8 \pm 0.2$; $2\sigma$). Magnesium isotope data from T77/F50 are negatively fractionated ($\delta^{25}Mg = -0.8 \pm 0.4‰$, $\delta^{26}Mg = -1.4 \pm 0.9‰$, 2SD; average values) relative to a chondritic composition. These values are similar to negative Mg isotope fractionations observed in some AOAs (Fig. 9), suggesting that the T77/F50 particle is linked to AOA olivines. In addition, minor element systematics of T77/F50 and their relationship with $\delta^{25}$Mg are similar to those of pore-rich AOAs (Figs. 12a-d and Figs. 13b-e, respectively). In particular, the $\delta^{25}$Mg and minor element values of T77/F50 cannot be distinguished from those of AOA 502, which is the most porous example studied here (Figs. 4a-d). Furthermore, the $\Delta^{17}$O value of T77/F50 ($-23.9 \pm 1.6‰$, 2SD; Nakashima et al., 2012), is identical to that of AOA 502 ($\Delta^{17}O = -24.2 \pm 0.8‰$, 2SD) within uncertainties. Thus, the chemical and isotopic agreement between T77/F50 and at least one pore-rich AOA indicates that T77/F50 likely formed by disequilibrium condensation from the solar nebula, within an AOA-forming region providing strong evidence for some materials in comet Wild 2 and chondrites to be sourced from similar nebular regions.

T175/F1 is also a nearly pure forsterite particle ($Fo_{99.8}$) with a $\Delta^{17}$O value of $-23.3 \pm 1.4‰$ (2SD; Chaumard et al., 2018). However, unlike T77/F50, T175/F1 is not negatively

fractionated in its Mg isotopes, beyond analytical uncertainties. On plots comparing $\delta^{25}$Mg-CrO-MnO, T175/F1 falls within the range of compact AOAs (Figs. 13b and d-e), suggesting they are related. Note that, however, the CaO content of T175/F1 (38 ± 3 ppm; 2σ) is remarkably lower than those of AOAs (Fig. 13c). The FeO content of T175/F1 is slightly higher than AOAs from DOM 08006 and is more consistent with Kaba compact AOA K27 (Figs. 12c-d). The slight enrichment in FeO suggests that either (1) minor Fe addition occurred after initial formation, like Kaba AOA K27, or (2) T175/F1 condensed at a higher dust/gas ratio (dust enrichment factor > 1). In either case, it is difficult to explain the depletion of CaO compared to AOA olivines, meaning T175/F1 may have a different origin than AOA olivines and T77/F50. $^{16}$O-rich, FeO-poor olivines are also found in chondrules as relict materials (e.g., Ushikubo et al., 2012; Marrocchi et al., 2019b), but their CaO contents are similar to those of AOAs (Marrocchi et al., 2019b), meaning a link between T175/F1 and relict olivine is unlikely. Matrix materials of chondrites also include $^{16}$O-rich, FeO-poor olivines (e.g., Nagashima et al., 2015). The average Ca content of matrix olivine grains from the Kakangari meteorite is 0.13 ± 0.56 wt% (Nagashima et al., 2015), which is higher than that of T175/F1 by a factor of ~30, indicative of an origin that is different than that of T175/F1 olivine.

Frank et al. (2014) conducted minor element analyses of more than forty Wild 2 olivine particles by TEM-EDX. Of six aerogel tracks (T57, T61, T111, T112, T130, and T154) with forsteritic olivine (> $Fo_{95}$), four (T57, T61, T111, and T112) have CaO-poor olivine (< 0.09 wt%). Among them, T61 terminal particles have low FeO (< 0.10 wt%), MnO and $Cr_2O_3$ (< 0.07 wt%), and CaO (< 0.09 wt%), which are similar to concentrations observed in T175/F1. Frank et al. (2014) also conducted minor element analyses of olivines from various types of chondrites. Since forsteritic olivines with very low CaO are not found in chondrites, Frank et al. (2014) suggested a link between T61 terminal olivine particles and olivines from aubrites. If this is also the case for T175/F1, it implies highly reducing, $^{16}$O-rich environments existed in the solar protoplanetary disk at the time of T175/F1 formation.

T57/F10 olivine also has $^{16}$O-rich oxygen isotopic characteristics ($\Delta^{17}O = -22.0 \pm 1.3‰$, 2SD; Nakashima et al., 2012) with a slight enrichment in FeO (1.75 ± 0.06 wt%; 2σ) compared to the other two $^{16}$O-rich Wild 2 and AOA olivines (~ 0.58 wt%) discussed above. This particle is not LIME olivine (MnO/FeO wt% = 0.38 ± 0.02; 2σ), though the MnO content is distinctively higher (MnO = 0.66 ± 0.02 wt%; 2σ) than those of the other two $^{16}$O-rich Wild 2 and AOA olivines (Fig. 12b). The $Cr_2O_3$ content is also slightly higher (CrO = 0.42 ± 0.05 wt%; 2σ) than those of the other two $^{16}$O-rich Wild 2 and AOA olivines. Hence, T57/F10 olivine is relatively enriched in the moderately to slightly refractory elements Mn, Cr, and Fe. We note that T57/F10 exhibits slightly positive $\delta^{25}$Mg and $^{26}$Mg values ($\delta^{25}Mg = 0.6\ ^{+0.5}/_{-0.6}‰$, $\delta^{26}Mg = 1.4\ ^{+1.0}/_{-1.3}‰$; 2σ) that are not observed in AOA olivines (Fig. 9). Therefore, if T57/F10 olivine formed by condensation, it likely occurred under different conditions relative to those of AOA olivines studied here. For example, Komatsu et al. (2015) modeled equilibrium condensation under various dust/gas ratios (dust enrichment factor = ~ 0.1-100) and predict that FeO and MnO contents, as well as the MnO/FeO ratio of T57/F10 are explained by equilibrium condensation at a higher dust/gas ratio (dust enrichment factor = ~20), and at relatively lower temperatures (< 1200 K). If we assume T57/F10 olivine formed by equilibrium condensation with a dust enrichment factor of ~20, most olivine (~90%) is predicted to have condensed at temperatures near 1500K (Komatsu et al., 2015), meaning that the fraction of olivines condensed at lower temperatures (< 1200 K) like T57/F10 would be very minor. In contrast, olivine grains with similar chemical compositions are commonly reported from Wild 2 particles, chondrite matrices (Frank et al., 2014), and IDPs (Klöck et al., 1989), indicative of their ubiquitous presence in the outer Solar System, which is inconsistent with the minor fraction predicted by equilibrium condensation calculation (Komatsu et al., 2015). Alternatively, a volatile-rich olivine like T57/F10 could have experienced a complex thermal history, involving re-equilibration with surrounding gas (Komatsu et al., 2015). Although oxygen isotope ratios of primary matrix minerals in chondrites are not well investigated due to their extremely small sizes (≤ 1 μm), Nagashima et al. (2015) reported $^{16}$O-rich matrix olivine grains from the Kakangari meteorite.

This suggests a link between T57/F10 and matrix olivine grains. Further studies that combined oxygen and magnesium isotope analyses, and minor element abundance measurements could provide important constraints on relationships between cometary and interplanetary dust particles, and fine-grained materials in chondrite matrices.

### 5.5. Origin of $^{16}$O-depleted Wild 2 olivine particles

Olivine particles T77/F4 and T149/F1 are FeO-rich ($Fo_{60}$ for T77/F4; Joswiak et al., 2012 and $Fo_{85}$ for T149/F1; Defouilloy et al., 2017) and have $^{16}$O-depleted oxygen isotopic signatures ($\Delta^{17}O = -1.5 \pm 1.2$‰ (2SD) for T77/F4; Nakashima et al., 2012 and $\Delta^{17}O = -1.7 \pm 1.5$‰ (2σ) for T149/F1; Defouilloy et al., 2017). $\delta^{25}$Mg values of T77/F4 and T149/F1 are $-0.2\ ^{+0.8}/_{-0.5}$‰ (2σ) and –0.5 ± 0.3 ‰ (2SD; average value), respectively, both of which are near-chondritic values. As discussed earlier for $^{16}$O-rich Wild 2 olivines, near-chondritic Mg isotope ratios can be explained by equilibrium condensation. However, FeO contents of T77/F4 and T149/F1 are too high compared to those expected by equilibrium condensation (e.g., Komatsu et al., 2015), meaning such an origin is unlikely. Alternatively, FeO-rich and $^{16}$O-depleted oxygen isotopic signatures are well explained by formation at high dust/gas ratios (dust enrichment factor = ~2500) in the protoplanetary disk (Tenner et al., 2015). In addition, the Fo contents and oxygen isotope ratios of T77/F4 and T149/F1 olivines are similar to those of type II chondrule olivines from CR and CH chondrites, indicative of a possible genetic link (Nakashima et al., 2012; Defouilloy et al., 2017). The $\delta^{25}$Mg values of T77/F4 and T149/F1 are within the range of those of bulk chondrules (e.g., Bouvier et al., 2013; Van Kooten et al., 2016; Olsen et al., 2016; Chen et al., 2018), supporting a link between Wild 2 $^{16}$O-depleted particles and type II chondrules in chondrites. Note that these high precision Mg stable isotope data are from bulk chondrule analyses, not from chondrule olivine themselves. Future high precision Mg isotope analyses of chondrule olivines will give an opportunity to discuss their relations with $^{16}$O-depleted Wild 2 olivines.

### 5.6. Implications for dust transportation in the solar protoplanetary disk

Magnesium isotope and minor element analyses of Wild 2 olivine particles suggest they underwent a variety of nebular processing. For example, oxygen and magnesium isotopes, and chemical compositions of Wild 2 LIME olivine T77/F50 are in excellent agreement with those of pore-rich AOA olivines from the DOM 08006 (CO3.01) carbonaceous chondrite. The Mg isotope ratios of T77/F50 are negatively fractionated, indicating this particle formed by disequilibrium condensation from the solar nebula. Since characteristic nebular temperatures beyond 5 astronomical units (AU) should not exceed 200 K (e.g., Desch et al., 2018), the condensation of T77/F50 from comet-forming regions (~ tens of AU) seems unlikely. Instead, it is more likely that T77/F50 condensed within the inner protoplanetary disk (< 1 AU), as ambient temperatures would have exceeded 1000 K during early Solar System evolution (Desch et al., 2018). This would also explain the $^{16}$O-rich signatures of some Wild 2 olivine particles, as measurements of solar wind infer the proto-Sun was $^{16}$O-rich (McKeegan et al., 2011). Therefore, the presence of $^{16}$O-rich "condensed" olivine in comet 81P/Wild 2 provides evidence for material transport from the inner part of the Solar System outward, to comet-forming regions.

Mechanisms for such transportation have been hypothesized by several studies (Ciesla., 2007; Nakamura et al., 2008; Hughes and Armitage, 2010; Nakashima et al., 2012; Joswiak et al., 2017), in order to explain the presence of $^{16}$O-rich CAI-like materials in comet 81P/Wild 2 (McKeegan et al., 2006; Simon et al., 2008; Matzel et al., 2010). Al-Mg isotope analyses of two $^{16}$O-rich CAI-like materials in comet 81P/Wild 2, Coki and Inti, indicate the absence of live $^{26}$Al at the time of their formation (Ishii et al., 2010; Matzel et al., 2010), in which the $^{26}$Al/$^{27}$Al upper limit of Coki was determined to be $< 1 \times 10^{-5}$. The absence of live $^{26}$Al at the time of $^{16}$O-rich Wild 2 materials indicates that they formed either (1) very early (i.e., before injection and homogenization of $^{26}$Al in the Solar System), or (2) late formation (> 1.7 Myr after CAIs: Matzel et al., 2010) after the decay of $^{26}$Al if using a canonical $(^{26}Al/^{27}Al)_0$ of $5.2 \times 10^{-5}$ (Jacobsen et al., 2008; Larsen et al., 2011), and assuming a homogeneous distribution of $^{26}$Al in the early Solar System. In the case of (1), transport was efficient enough to deliver the earliest formed materials

to the outer Solar System, which is consistent with earliest formed CAIs to be transported into the outer part of the solar protoplanetary disk (Yang and Ciesla, 2012; Fukuda et al., 2019b; Larsen et al., 2020). In the case of (2), no evidence of live $^{26}$Al within $^{16}$O-rich Wild 2 materials indicates, conversely, that transport was not efficient enough to deliver the earliest formed materials with the canonical $(^{26}Al/^{27}Al)_0$ values from inner (< 1 AU) to the outer Solar System (~30 AU). In either case, the presence of the AOA-like olivine (T77/F50) could place important constraints on the efficiency of such transportation processes as well as residence time of dust in the solar protoplanetary disk. Due to the absence of Al-rich phases (e.g., anorthite) associated with the $^{16}$O-rich olivine particles studied here, we cannot constrain the initial abundances of $^{26}$Al when T77/F50 formed. However, Al-Mg isotope analyses of AOAs from primitive chondrites suggest they formed around a time similar to the formation of CV3 CAIs ($^{26}Al/^{27}Al$ ~$5 \times 10^{-5}$ ; Itoh et al., 2007; Sugiura and Krot, 2007; MacPherson et al., 2012; Ushikubo et al., 2017), except for some AOAs in CH chondrites, which could have recorded admixing of $^{26}$Al in the earliest stage of the Solar System evolution and/or might have experienced thermal annealing by an impact-generated plume (Krot et al., 2014). On the basis of chemical and isotopic similarities between T77/F50 and AOA olivines from DOM 08006, T77/F50 may also have formed at the same time as CAIs and AOAs, suggesting that the efficiency of the transportation processes was sufficient to transport solid particles from the inner (< 1 AU) to the outer Solar System (~30 AU) at the earliest stage of the Solar System evolution. Recently, Neveu and Vernazza (2019) conducted thermal evolution simulations for IDP-like bodies including D-type asteroids that may have formed within comet-forming regions (Fujiya et al., 2019), and predicted accretion of IDP-like bodies at least 5-6 Myr after the formation of CAIs in CV3 chondrites. If true, the presence of AOA-like olivine in the comet 81P/Wild 2 would indicate that the residence time of dust particles exceeded 5-6 Myr during the earliest stages of the Solar System evolution.

## 6. CONCLUSIONS

994

995 Magnesium isotope ratios and minor element abundances of $^{16}$O-rich and $^{16}$O-depleted
996 Wild 2 olivine particles were investigated by SIMS. Oxygen and Mg isotope ratios and minor
997 element abundances of AOA olivines from Kaba and DOM 08006 carbonaceous chondrites were
998 also determined in order to compare with those of $^{16}$O-rich Wild 2 olivine particles.
999 Oxygen isotope data from Kaba and DOM 08006 AOA olivine are identical within
1000 uncertainties; they are also in agreement with oxygen isotope data from Acfer 094 AOAs. These
1001 results indicate AOAs originated from a single homogeneous reservoir.
1002 SIMS minor element analyses reveal uniform FeO contents of olivine in AOAs from
1003 DOM 08006 (~0.05 wt%), suggesting AOAs formed at more reducing environments in the solar
1004 nebula than previously thought. In contrast, EPMA-derived FeO contents of the same AOA
1005 olivine are systematically higher than those obtained by SIMS analyses, indicating that EPMA-
1006 derived FeO contents of AOA olivine tend to be influenced by fluorescence from surrounding
1007 matrix materials and/or Fe,Ni-metals in AOAs.
1008 Magnesium isotopes of Kaba and DOM 08006 AOA olivines are negatively mass-
1009 dependently fractionated down to –3.8‰ from the chondritic value, indicative of a
1010 disequilibrium condensation origin for some AOAs. Olivine grains from compact AOAs show
1011 limited variations in $\delta^{25}$Mg ranging from –1.2‰ to –0.2‰. In contrast, larger variations in
1012 $\delta^{25}$Mg, ranging from –3.8‰ to –0.4‰, are observed in olivine grains from pore-rich AOAs. The
1013 latter data are positively correlated with their CrO contents, suggesting that the variation in Mg
1014 isotope ratios was related to condensation temperature during formation. In contrast, the limited
1015 variation in $\delta^{25}$Mg of compact AOAs likely resulted from partial isotope exchange with ambient
1016 gas through high-temperature annealing.
1017 Magnesium isotope ratios of five Wild 2 olivine particles are consistent with mass-
1018 dependent fractionation from a chondritic Mg isotopic composition, indicating that Wild 2
1019 olivine particles formed in the chondritic reservoir with respect to Mg isotope compositions.
1020 Three $^{16}$O-rich Wild 2 olivines have small variations in $\delta^{25}$Mg, ranging from –1.0‰ to 0.6‰.

Considering their minor element abundances, these particles may have experienced complex thermal histories including condensation followed by annealing. Two $^{16}$O-depleted Wild 2 olivines have near-chondritic Mg isotope ratios, supporting an origin that is similar to meteoritic chondrules.

One $^{16}$O-rich Wild 2 LIME olivine particle, T77/F50, shows agreement in terms of chemical and isotopic compositions with olivines in pore-rich AOAs from DOM 08006, suggesting that T77/F50 formed by disequilibrium condensation near the proto-Sun. If this is the case, this olivine particle likely traveled to the outer solar protoplanetary disk and then was accreted during the formation of comet 81P/Wild 2.

**ACKNOWLEDGEMENTS**

We are grateful to Guillaume Siron and Kouki Kitajima for valuable comments on data reduction procedures. We thank Naoji Sugiura for providing condensation model results, Richard K. Noll, Guillaume Siron, Bil Schneider for FIB marking and SEM observations, John H. Fournelle and Guillaume Siron for assistance with EPMA analysis, and Michael J. Spicuzza for technical assistance with SIMS operation. We also thank Timothy J. Fagan and an anonymous reviewer for constructive comments that improved the quality of the paper, and Audrey Bouvier for prompt editorial handling. This work is supported by the NASA Laboratory Analysis of Returned Samples (LARS) program (NNX16AG80G). WiscSIMS is partly supported by NSF Instrumentation and Facility (IF) Program (EAR-1658823). The upgrade of the RF plasma source is supported by the NASA LARS and Planetary Major Equipment (PME) Programs (NNX16AG80G) and the NSF IF Program (EAR-1355590). Support for FIB instrumentation was provided by NSF through the University of Wisconsin Materials Research Science and Engineering Center (DMR-1720415).

1048

1049 **REFERENCES**

1050

1051 Aléon J., Krot A. N. and McKeegan K. D. (2002) Calcium-aluminum-rich inclusions and
1052 amoeboid olivine aggregates from the CR carbonaceous chondrites. *Meteorit. Planet. Sci.*
1053 **37**, 1729–1755.
1054 Ando K., Kurokawa H. and Oishi Y. (1981) Self-diffusion coefficient of oxygen in Single-
1055 crystal forsterite. *J. Am. Ceram. Soc.* **64**, C30.
1056 Baertschi P. (1976) Absolute $^{18}O$ content of standard mean ocean water. *Earth Planet. Sci. Lett.*
1057 **31**, 341–344.
1058 Bodénan J. D., Starkey N. A., Russell S. S., Wright I. P. and Franchi I. A. (2014) An oxygen
1059 isotope study of Wark-Lovering rims on type A CAIs in primitive carbonaceous chondrites.
1060 *Earth Planet. Sci. Lett.* **401**, 327–336.
1061 Bonal L., Quirico E., Bourot-Denise M. and Montagnac G. (2006) Determination of the
1062 petrologic type of CV3 chondrites by Raman spectroscopy of included organic matter.
1063 *Geochim. Cosmochim. Acta* **70**, 1849–1863.
1064 Bouvier A., Wadhwa M., Simon S. B. and Grossman L. (2013) Magnesium isotopic fractionation
1065 in chondrules from the Murchison and Murray CM2 carbonaceous chondrites. *Meteorit.*
1066 *Planet. Sci.* **48**, 339–353.
1067 Bradley J. P. (2003) Interplanetary dust particles. In *Treatise on Geochemistry* (eds. H. Holland
1068 and K. Turekian). Elsevier, Oxford. pp. 689–711.
1069 Bridges J. C., Changela H. G., Nayakshin S., Starkey N. A. and Franchi I. A. (2012) Chondrule
1070 fragments from Comet Wild2 : Evidence for high temperature processing in the outer Solar
1071 System. *Earth Planet. Sci. Lett.* **341**–**344**, 186–194.
1072 Brownlee D. E. (2014) The Stardust mission : Analyzing samples from the edge of the Solar
1073 System. *Annu. Rev. Earth Planet. Sci.* **42**, 179–205.
1074 Brownlee D. E., Tsou P., Aléon J., Alexander C. M. O. D., Araki T., Bajt S., Baratta G. A.,

Bastien R., Bland P., Bleuet P., Borg J., Bradley J. P., Brearley A., Brenker F., Brennan S., Bridges J. C., Browning N. D., Brucato J. R., Bullock E., Burchell M. J., Busemann H., Butterworth A., Chaussidon M., Cheuvront A., Chi M., Cintala M. J., Cordier P., Daghlian C., Dai Z., Hendecourt L. D., Djouadi Z., Economou T. E., Fakra S., Fairey S. A. J., Fallon S., Gillet P., Gilmour J., Glavin D. P., Gounelle M., Grady M. M., Huth J., Hutcheon I. D., Ignatyev K., Ishii H., Ito M., Jurewicz A., Kearsley A. T., Keller L. P., Khodja H., Kilcoyne A. L. D., Matrajt G., Mckeegan K., Meibom A., Mennella V., Messenger K., Perkins D., Perronnet M., Pianetta P., Rao W., Rietmeijer F. J. M., Schwandt C. S., See T. H., Schlutter D., Simionovici A., Simon S., Sitnitsky I., Snead C. J., Wooden D., Wopenka B., Wozniakiewicz P. and Wright I. (2006) Comet 81P/Wild 2 under a microscope. *Science* **314**, 1711–1716.

Brownlee D. E., Joswiak D. J. and Matrajt G. (2012) Overview of the rocky component of Wild 2 comet samples: Insight into the early solar system, relationship with meteoritic materials and the differences between comets and asteroids. *Meteorit. Planet. Sci.* **470**, 453–470.

Burchell M. J., Fairey S. A. J., Wozniakiewicz P., Brownlee D. E., Hörz F., Kearsley A. T., See T. H., Tsou P., Westphal A., Green S. F., Trigo-Rodríguez J. M. and Domingúez G. (2008) Characteristics of cometary dust tracks in Stardust aerogel and laboratory calibrations. *Meteorit. Planet. Sci.* **43**, 23–40.

Buse B., Wade J., Llovet X., Kearns S. and Donovan J. J. (2018) Secondary fluorescence in WDS: The role of spectrometer positioning. *Microsc. Microanal.* **24**, 604–611.

Catanzaro E. J., Murphy T. J., Garner E. L. and Shields W. R. (1966) Absolute isotopic abundance ratios and atomic weight of magnesium. *J. Res. Natl. Bur. Stand. Sect. A Phys. Chem.* **70A**, 453–458.

Chakraborty S. (2010) Diffusion coefficients in olivine, wadsleyite and ringwoodite. *Rev. Mineral. Geochemistry* **72**, 603–639.

Chaumard N., Defouilloy C., Joswiak D. J., Brownlee D. E., Westphal A. J. and Kita N. T. (2018) Oxygen three-isotope ratios of particles from the comet 81P/Wild 2: Systemtaic

within individual tracks. *49th Lunar Planet. Sci. Conf.*, 2163.

Chen H. W., Claydon J. L., Elliott T., Coath C. D., Lai Y. J. and Russell S. S. (2018) Chronology of formation of early solar system solids from bulk Mg isotope analyses of CV3 chondrules. *Geochim. Cosmochim. Acta* **227**, 19–37.

Chi M., Ishii H. A., Simon S. B., Bradley J. P., Dai Z., Joswiak D., Browning N. D. and Matrajt G. (2009) The origin of refractory minerals in comet 81P/Wild 2. *Geochim. Cosmochim. Acta* **73**, 7150–7161.

Ciesla F. J. (2007) Outward transport of high-temperature materials around the midplane of the solar nebula. *Science* **318**, 613–615.

Clayton R. N. and Mayeda T. K. (1977) Correlated oxygen and magnesium isotope anomalies in Allende Inclusions, I: Oxygen. *Geophys. Res. Lett.* **4**, 295–298.

Clayton R. N., Onuma N., Grossman L. and Mayeda T. K. (1977) Distribution of the pre-solar component in Allende and other carbonaceous chondrites. *Earth Planet. Sci. Lett.* **34**, 209–224.

Clayton R. N., Mayeda T. K., Goswami J. N. and Olsen E. J. (1991) Oxygen isotope studies of ordinary chondrites. *Geochim. Cosmochim. Acta* **55**, 2317–2337.

Coogan L. A., Hain A., Stahl S. and Chakraborty S. (2005) Experimental determination of the diffusion coefficient for calcium in olivine between 900°C and 1500°C. *Geochim. Cosmochim. Acta* **69**, 3683–3694.

Davidson J., Alexander C. M. O., Stroud R. M., Busemann H. and Nittler L. R. (2019) Mineralogy and petrology of Dominion Range 08006: A very primitive CO3 carbonaceous chondrite. *Geochim. Cosmochim. Acta* **265**, 259–278.

Davis A. M., Richter F. M., Mendybaev R. A., Janney P. E., Wadhwa M. and McKeegan K. D. (2015) Isotopic mass fractionation laws for magnesium and their effects on26Al–26Mg systematics in solar system materials. *Geochim. Cosmochim. Acta* **158**, 245–261.

Defouilloy C., Nakashima D., Joswiak D. J., Brownlee D. E., Tenner T. J. and Kita N. T. (2017) Origin of crystalline silicates from Comet 81P/Wild 2: Combined study on their oxygen

isotopes and mineral chemistry. *Earth Planet. Sci. Lett.* **465**, 145–154.

Desch S. J., Kalyaan A. and Alexander C. M. O. (2018) The effect of Jupiter's formation on the distribution of refractory elements and inclusions in meteorites. *Astrophys. J. Suppl. Ser.* **238**, 11.

Ebel D. S., Weisberg M. K. and Beckett J. R. (2012) Thermochemical stability of low-iron, manganese-enriched olivine in astrophysical environments. *Meteorit. Planet. Sci.* **47**, 585–593.

Fagan T. J., Krot A. N., Keil K. and Yurimoto H. (2004) Oxygen isotopic evolution of amoeboid olivine aggregates in the reduced CV3 chondrites Efremovka, Vigarano, and Leoville. *Geochim. Cosmochim. Acta* **68**, 2591–2611.

Fournelle J. H., Kim S. and Perepezko J. H. (2005) Monte Carlo simulation of Nb Kα secondary fluorescence in EPMA: Comparison of PENELOPE simulations with experimental results. *Surf. Interface Anal.* **37**, 1012–1016.

Frank D. R., Zolensky M. E. and Le L. (2014) Olivine in terminal particles of Stardust aerogel tracks and analogous grains in chondrite matrix. *Geochim. Cosmochim. Acta* **142**, 240–259.

Fujiya W., Hoppe P., Ushikubo T., Fukuda K., Lindgren P., Lee M. R., Koike M., Shirai K. and Sano Y. (2019) Migration of D-type asteroids from the outer Solar System inferred from carbonate in meteorites. *Nat. Astron.* **3**, 910–915.

Fukuda K., Joswiak D. J., Brownlee D. E., Beard B. L., Spicuzza M. J., Tenner T. J., Kimura M. and Kita N. T. (2019a) The relationship between oxygen and magnesium isotope ratios in olivine from the comet 81P/Wild 2: A comparison with AOAs in primitive meteorites. *50th Lunar Planet. Sci. Conf.*, 1989.

Fukuda K., Hiyagon H., Fujiya W., Takahata N., Kagoshima T. and Sano Y. (2019b) Origin of the short-lived radionuclide $^{10}$Be and its implications for the astronomical setting of CAI formation in the solar protoplanetary disk. *Astrophys. J.* **886**, 11pp.

Fukuda K., Beard B. L., Dunlap D. R., Spicuzza M. J., Fournelle J. H., Wadhwa M. and Kita N. T. (2020) Magnesium isotope analysis of olivine and pyroxene by SIMS: Evaluation of

matrix effects. *Chem. Geol.* **540**, 119482.

Gainsforth Z., Butterworth A. L., Stodolna J., Westphal A. J., Huss G. R., Nagashima K., Ogliore R., Brownlee D. E., Joswiak D., Tyliszczak T. and Simionovici A. S. (2015) Constraints on the formation environment of two chondrule-like igneous particles from comet 81P/Wild 2. *Meteorit. Planet. Sci.* **50**, 976–1004.

Galy A., Yoffe O., Janney P. E., Williams R. W., Cloquet C., Alard O., Halicz L., Wadhwa M., Hutcheon I. D., Ramon E. and Carignan J. (2003) Magnesium isotope heterogeneity of the isotopic standard SRM980 and new reference materials for magnesium-isotope-ratio measurements. *J. Anal. At. Spectrom.* **18**, 1352.

Grossman L. and Steele I. M. (1976) Amoeboid olivine aggregates in the Allende meteorite. *Geochim. Cosmochim. Acta* **40**, 149-155.

Han J. and Brearley A. J. (2015) Microstructural evidence for complex formation histories of amoeboid olivine aggregates from the ALHA77307 CO3.0 chondrite. *Meteorit. Planet. Sci.* **50**, 904–925.

Hertwig A. T., Kimura M., Ushikubo T., Defouilloy C. and Kita N. T. (2019) The $^{26}$Al-$^{26}$Mg systematics of FeO-rich chondrules from Acfer 094: Two chondrule generations distinct in age and oxygen isotope ratios. *Geochim. Cosmochim. Acta* **253**, 111–126.

Hölz F., Ron B., Borg J., Bradley J. P., Bridges J. C., Brownlee D. E., Burchell M. J., Chi M., Cintala M. J., Dai Z. R., Djouadi Z., Dominguez G., Economou T. E., Fairey S. A. J., Floss C., Franchi I. A., Graham G. A., Green S. F., Heck P., Hoppe P., Huth J., Ishii H., Kearsley A. T., Kissel J., Leitner J., Leroux H., Marhas K., Messenger K., Schwandt C. S., See T. H., Snead C., Stadermann F. J., Stephan T., Stroud R., Teslich N., Trigo-Rodríguez J. M., Tuzzolino A. J., Troadec D., Tsou P., Warren J., Westphal A., Wozniakiewicz P., Wright I. and Zinner E. (2006) Impact features on Stardust : Implications for Comet 81P / Wild 2 dust. *Science.* **314**, 1716–1719.

Hughes A. L. H. and Armitage P. J. (2010) Particle transport in evolving protoplanetary disks: Implications for results from Stardust. *Astrophys. J.* **719**, 1633–1653.

1183 Ishii H., Stadermann F. J., Floss C., Joswiak D. J., Bradley J. P., Teslich N., Brownlee D. E.,
1184 Matrajt G., Macpherson G. J. and McKeegan K. D. (2010) Lack of evidence for in situ
1185 decay of Aluminum-26 in comet 81P/Wild 2 CAI-like refractory particles "Inti" and
1186 "Coki." *40th Lunar Planet. Sci. Conf.*, 2317.
1187 Itoh S., Russell S. S. and Yurimoto H. (2007) Oxygen and magnesium isotopic compositions of
1188 amoeboid olivine aggregates from the Semarkona LL3.0 chondrite. *Meteorit. Planet. Sci.*
1189 **42**, 1241–1247.
1190 Jacobsen B., Yin Q.-Z., Moynier F., Amelin Y., Krot A. N., Nagashima K., Hutcheon I. D. and
1191 Palme H. (2008) $^{26}$Al-$^{26}$Mg and $^{207}$Pb-$^{206}$Pb systematics of Allende CAIs: Canonical solar
1192 initial $^{26}$Al/$^{27}$Al ratio reinstated. *Earth Planet. Sci. Lett.* **272**, 353–364.
1193 Jollands M. C., Hermann J., St. O'Neill H. C., Spandler C. and Padrón-Navarta J. A. (2016)
1194 Diffusion of Ti and some divalent cations in olivine as a function of temperature, oxygen
1195 fugacity, chemical potentials and crystal orientation. *J. Petrol.* **57**, 1983–2010.
1196 Jollands M. C., O'Neill H. S. C., Van Orman J., Berry A. J., Hermann J., Newville M. and
1197 Lanzirotti A. (2018) Substitution and diffusion of $Cr^{2+}$ and $Cr^{3+}$ in synthetic forsterite and
1198 natural olivine at 1200–1500 °C and 1 bar. *Geochim. Cosmochim. Acta* **220**, 407–428.
1199 Joswiak D. J., Brownlee D. E., Matrajt G., Westphal A. J., Snead C. J. and Gainsforth Z. (2012)
1200 Comprehensive examination of large mineral and rock fragments in Stardust tracks:
1201 Mineralogy, analogous extraterrestrial materials, and source regions. *Meteorit. Planet. Sci.*
1202 **47**, 471–524.
1203 Joswiak D. J., Nakashima D., Brownlee D. E., Matrajt G., Ushikubo T., Kita N. T., Messenger S.
1204 and Ito M. (2014) Terminal particle from Stardust track 130: Probable Al-rich chondrule
1205 fragment from comet Wild 2. *Geochim. Cosmochim. Acta* **144**, 277–298.
1206 Joswiak D. J., Brownlee D. E., Nguyen A. N. and Messenger S. (2017) Refractory materials in
1207 comet samples. *Meteorit. Planet. Sci.* **52**, 1612–1648.
1208 Kita N. T., Nagahara H., Tachibana S., Tomomura S., Spicuzza M. J., Fournelle J. H. and Valley
1209 J. W. (2010) High precision SIMS oxygen three isotope study of chondrules in LL3

chondrites: Role of ambient gas during chondrule formation. *Geochim. Cosmochim. Acta* **74**, 6610–6635.

Kita N. T., Ushikubo T., Knight K. B., Mendybaev R. A., Davis A. M., Richter F. M. and Fournelle J. H. (2012) Internal $^{26}$Al-$^{26}$Mg isotope systematics of a Type B CAI: Remelting of refractory precursor solids. *Geochim. Cosmochim. Acta* **86**, 37–51.

Klöck W., Thomas K. L., McKay D. S. and Palme H. (1989) Unusual olivine and pyroxene composition in interplanetary dust and unequilibrated ordinary chondrites. *Nature* **339**, 126–128.

Komatsu M., Krot A. N., Petaev M. I., Ulyanov A. A., Keil K. and Miyamoto M. (2001) Mineralogy and petrography of amoeboid olivine aggregates from the reduced CV3 chondrites Efremovka, Leoville and Vigarano: Products of nebular condensation, accretion and annealing. *Meteorit. Planet. Sci.* **36**, 629–641.

Komatsu M., Mikouchi T. and Miyamoto M. (2009) High-temperature annealing of amoeboid olivine aggregates: Heating experiments on olivine-anorthite mixtures. *Polar Sci.* **3**, 31–55.

Komatsu M., Fagan T. J., Mikouchi T., Petaev M. I. and Zolensky M. E. (2015) LIME silicates in amoeboid olivine aggregates in carbonaceous chondrites: Indicator of nebular and asteroidal processes. *Meteorit. Planet. Sci.* **50**, 1271–1294.

Komatsu M., Fagan T. J., Krot A. N., Nagashima K., Petaev M. I., Kimura M. and Yamaguchi A. (2018) First evidence for silica condensation within the solar protoplanetary disk. *Proc. Natl. Acad. Sci.* **115**, 7497–7502.

Kööp L., Nakashima D., Heck P. R., Kita N. T., Tenner T. J., Krot A. N., Nagashima K., Park C. and Davis A. M. (2016) New constraints on the relationship between $^{26}$Al and oxygen, calcium, and titanium isotopic variation in the early Solar System from a multielement isotopic study of spinel-hibonite inclusions. *Geochim. Cosmochim. Acta* **184**, 151–172.

Krot A. N., Petaev M. I., Russell S. S., Itoh S., Fagan T. J., Yurimoto H., Chizmadia L., Weisberg M. K., Komatsu M., Ulyanov A. A. and Keil K. (2004a) Amoeboid olivine aggregates and related objects in carbonaceous chondrites: Records of nebular and asteroid

processes. *Chemie der Erde* **64**, 185–239.

Krot A. N., Petaev M. I. and Yurimoto H. (2004b) Amoeboid olivine aggregates with low-Ca pyroxenes: A genetic link between refractory inclusions and chondrules? *Geochim. Cosmochim. Acta* **68**, 1923–1941.

Krot A. N., Park C. and Nagashima K. (2014) Amoeboid olivine aggregates from CH carbonaceous chondrites. *Geochim. Cosmochim. Acta* **139**, 131–153.

Larimer J. W. (1967) Chemical fractionations in meteorites-I. Condensation of the elements. *Geochim. Cosmochim. Acta* **31**, 1215–1238.

Larsen K. K., Trinquier A., Paton C., Schiller M., Wielandt D., Ivanova M. A., Connelly J. N., Nordlund Å., Krot A. N. and Bizzarro M. (2011) Evidence for magnesium isotope heterogeneity in the solar protoplanetary disk. *Astrophys. J. Lett.* **735**, 7pp.

Larsen K. K., Wielandt D., Schiller M., Krot A. N. and Bizzarro M. (2020) Episodic formation of refractory inclusions in the Solar System and their presolar heritage. *Earth Planet. Sci. Lett.* **535**, 116088.

Leitner J., Hoppe P. and Heck P. R. (2010) Fisrt discovery of presolar material of possible supernova origin in impact residues from comet 81P/Wild 2. *41th Lunar Planet. Sci. Conf.*, 1607.

Leitner J., Heck P. R., Hoppe P. and Huth J. (2012) The C-, N- and O-isotopic composition of cometary dust from comet 81P/Wild 2. *43rd Lunar Planet. Sci. Conf.*, 1839.

Liu M. C., McKeegan K. D., Goswami J. N., Marhas K. K., Sahijpal S., Ireland T. R. and Davis A. M. (2009) Isotopic records in CM hibonites: Implications for timescales of mixing of isotope reservoirs in the solar nebula. *Geochim. Cosmochim. Acta* **73**, 5051–5079.

Lodders K. (2003) Solar system abundances and condensation temperatures of the elements. *Astrophys. J.* **591**, 1220–1247.

Ludwig K. R. (2012) User's Manual for Isoplot 3.75. Berkley Geochronology Center, Special Publication, pp. 1–75.

MacPherson G. J., Kita N. T., Ushikubo T., Bullock E. S. and Davis A. M. (2012) Well-resolved

variations in the formation ages for Ca-Al-rich inclusions in the early Solar System. *Earth Planet. Sci. Lett.* **331**–**332**, 43–54.

MacPherson G. J., Bullock E. S., Tenner T. J., Nakashima D., Kita N. T., Ivanova M. A., Krot A. N., Petaev M. I. and Jacobsen S. B. (2017) High precision Al–Mg systematics of forsterite-bearing Type B CAIs from CV3 chondrites. *Geochim. Cosmochim. Acta* **201**, 65–82.

Makide K., Nagashima K., Krot A. N., Huss G. R., Hutcheon I. D. and Bischoff A. (2009) Oxygen- and magnesium-isotope compositions of calcium-aluminum-rich inclusions from CR2 carbonaceous chondrites. *Geochim. Cosmochim. Acta* **73**, 5018–5050.

Marrocchi Y., Villeneuve J., Jacquet E., Piralla M. and Chaussidon M. (2019a) Rapid condensation of the first Solar System solids. *Proc. Natl. Acad. Sci.* **116**, 23461–23466.

Marrocchi Y., Euverte R., Villeneuve J., Batanova V., Welsch B., Ferrière L. and Jacquet E. (2019b) Formation of CV chondrules by recycling of amoeboid olivine aggregate-like precursors. *Geochim. Cosmochim. Acta* **247**, 121–141.

Matrajt G., Ito M., Wirick S., Messenger S., Brownlee D. E. and Joswiak D. (2008) Carbon investigation of two Stardust particles : A TEM , NanoSIMS , and XANES study. *Meteorit. Planet. Sci.* **43**, 315–334.

Matzel J. E. P., Ishii H. A., Joswiak D. J., Hutcheon I. D., Bradley J. P., Brownlee D. E., Weber P. K., Teslich N., Matrajt G., McKeegan K. D. and MacPherson G. J. (2010) Constraints on the formation age of cometary material from the NASA Stardust mission. *Science* **328**, 483–486.

McKeegan K. D., Aléon J., Bradley J., Brownlee D. E., Busemann H., Butterworth A., Chaussidon M., Fallon S., Floss C., Gilmour J., Gounelle M., Graham G., Guan Y., Heck P. R., Hoppe P., Hutcheon I. D., Huth J., Ishii H., Ito M., Jacobsen S. B., Kearsley A., Leshin L. A., Liu M. C., Lyon I., Marhas K. K., Marty B., Matrajt G., Meibom A., Messenger S., Mostefaoui S., Mukhopadhyay S., Nakamura-Messenger K., Nittler L., Palma R., Pepin R. O., Papanastassiou D. A., Robert F., Schlutter D., Snead C. J., Stadermann F. J., Stroud R., Tsou P., Westphal A., Young E. D., Ziegler K., Zimmermann L. and Zinner E. (2006)

1291 Isotopic compositions of cometary matter returned by stardust. *Science* **314**, 1724–1728.
1292 McKeegan K. D., Kallio A. P. A., Heber V. S., Jarzebinski G., Mao P. H., Coath C. D., Kunihiro
1293 T., Wiens R. C., Nordholt J. E., Moses R. W., Reisenfeld D. B., Jurewicz A. J. G. and
1294 Burnett D. S. (2011) The oxygen isotopic composition of the sun inferred from captured
1295 solar wind. *Science* **332**, 1528–1532.
1296 Messenger S., Joswiak D. J., Ito M., Matrajt G. and Brownlee D. E. (2009) Discovery of presolar
1297 SiC from comet WILD-2. *40th Lunar Planet. Sci. Conf.*, 1790.
1298 Morioka M. (1981) Cation diffusion in olivine-II. Ni-Mg, Mn-Mg, Mg and Ca. *Geochim.*
1299 *Cosmochim. Acta* **45**, 1573–1580.
1300 Nagashima K., Krot A. N. and Huss G. R. (2015) Oxygen-isotope compositions of chondrule
1301 phenocrysts and matrix grains in Kakangari K-grouplet chondrite: Implication to a
1302 chondrule-matrix genetic relationship. *Geochim. Cosmochim. Acta* **151**, 49–67.
1303 Nakamura-Messenger K., Keller L. P., Clemett S. J., Messenger S. and Ito M. (2011)
1304 Nanometer-scale anatomy of entire Stardust tracks. *Meteorit. Planet. Sci.* **46**, 1033–1051.
1305 Nakamura T., Noguchi T., Tsuchiyama A., Ushikubo T., Kita N. T., Valley J. W., Zolensky M.
1306 E., Kakazu Y., Sakamoto K., Mashio E., Uesugi K. and Nakano T. (2008) Chondrulelike
1307 objects in short-period Comet 81P/Wild 2. *Science* **321**, 1664–1667.
1308 Nakashima D., Ushikubo T., Joswiak D. J., Brownlee D. E., Matrajt G., Weisberg M. K.,
1309 Zolensky M. E. and Kita N. T. (2012) Oxygen isotopes in crystalline silicates of comet
1310 Wild 2: A comparison of oxygen isotope systematics between Wild 2 particles and
1311 chondritic materials. *Earth Planet. Sci. Lett.* **357**–**358**, 355–365.
1312 Nakashima D., Ushikubo T., Kita N. T., Weisberg M. K., Zolensky M. E. and Ebel D. S. (2015)
1313 Late formation of a comet Wild 2 crystalline silicate particle, Pyxie, inferred from Al-Mg
1314 chronology of plagioclase. *Earth Planet. Sci. Lett.* **410**, 54–61.
1315 Neveu M. and Vernazza P. (2019) IDP-like asteroids formed later than 5 Myr after Ca–Al-rich
1316 inclusions. *Astrophys. J.* **875**, 30.
1317 Ogliore R. C., Huss G. R., Nagashima K., Butterworth A. L., Gainsforth Z., Stodolna J.,

1318 Westphal A. J., Joswiak D. and Tyliszczak T. (2012) Incorporation of a late-forming
1319 chondrule into comet Wild 2. *Astrophys. J. Lett.* **745**, 1–5.
1320 Ogliore R. C., Nagashima K., Huss G. R., Westphal A. J., Gainsforth Z. and Butterworth A. L.
1321 (2015) Oxygen isotopic composition of coarse- and fine-grained material from comet
1322 81P/Wild 2. *Geochim. Cosmochim. Acta* **166**, 74–91.
1323 Olsen M. B., Krot A. N., Larsen K., Paton C., Wielandt D., Schiller M. and Bizzarro M. (2011)
1324 Whole-rock $^{26}$Al-$^{26}$Mg systematics of amoeboid olivine aggregates from the oxidized CV3
1325 carbonaceous chondrite Allende. *Meteorit. Planet. Sci.* **46**, 1688–1702.
1326 Olsen M. B., Wielandt D., Schiller M., Van Kooten E. M. M. E. and Bizzarro M. (2016)
1327 Magnesium and $^{54}$Cr isotope compositions of carbonaceous chondrite chondrules – Insights
1328 into early disk processes. *Geochim. Cosmochim. Acta* **191**, 118–138.
1329 Park C., Nagashima K., Krot A. N., Huss G. R., Davis A. M. and Bizzarro M. (2017) Calcium-
1330 aluminum-rich inclusions with fractionation and unidentified nuclear effects (FUN CAIs):
1331 II. Heterogeneities of magnesium isotopes and $^{26}$Al in the early Solar System inferred from
1332 in situ high-precision magnesium-isotope measurements. *Geochim. Cosmochim. Acta* **201**,
1333 6–24.
1334 Petaev M. I. and Wood J. a. (2005) Meteoritic constraints on temperatures, pressures, cooling
1335 rates, chemical compositions, and modes of condensation in the solar nebula. In *Chondrites*
1336 *and the Protoplanetary disk, ASP Conference Series* (eds. A. N. Krot, E. R. D. Scott, and B.
1337 Reipurth). Astronomical Society of the Pacific, San Francisco, California. pp. 373–406.
1338 Pettke T., Oberli F., Audétat A., Wiechert U., Harris C. R. and Heinrich C. A. (2011)
1339 Quantification of transient signals in multiple collector inductively coupled plasma mass
1340 spectrometry: Accurate lead isotope ratio determination by laser ablation of individual fluid
1341 inclusions. *J. Anal. At. Spectrom.* **26**, 475–492.
1342 Richter F. M. (2004) Timescales determining the degree of kinetic isotope fractionation by
1343 evaporation and condensation. *Geochim. Cosmochim. Acta* **68**, 4971–4992.
1344 Rubin A. E. (2013) An amoeboid olivine inclusion (AOI) in CK3 NWA 1559, comparison to

AOIs in CV3 Allende, and the origin of AOIs in CK and CV chondrites. *Meteorit. Planet. Sci.* **48**, 432–444.

Ruzicka A., Floss C. and Hutson M. (2012) Amoeboid olivine aggregates (AOAs) in the Efremovka, Leoville and Vigarano (CV3) chondrites: A record of condensate evolution in the solar nebula. *Geochim. Cosmochim. Acta* **79**, 79–105.

Sandford S. A. (2008) Terrestrial analysis of the organic component of comet dust. *Annu. Rev. Anal. Chem.*, 549–578.

Sandford S. A., Aleon J., Alexander C. M. O. '., Araki T., Bajt S., Baratta G. A., Borg J., Bradley J. P., Brownlee D. E., Brucato J. R., Burchell M. J., Busemann H., Butterworth A., Clemett S. J., Cody G., Colangeli L., Cooper G., Hendecourt L. D., Djouadi Z., Dworkin J. P., Ferrini G., Fleckenstein H., Flynn G. J., Franchi I. A., Fries M., Gilles M. K., Glavin D. P., Gounelle M., Grossemy F., Jacobsen C., Keller L. P., Kilcoyne A. L. D., Leitner J., Matrajt G., Meibom A., Mennella V., Mostefaoui S., Nittler L. R., Palumbo M. E., Papanastassiou D. A., Robert F., Rotundi A., Snead C. J., Spencer M. K., Stadermann F. J., Steele A., Stephan T., Tsou P., Tyliszczak T., Westphal A. J., Wirick S., Wopenka B., Yabuta H., Zare R. N. and Zolensky M. E. (2006) Organics captured from comet 81P/Wild 2 by the Stardust spacecraft. *Science* **314**, 1720–1724.

Simon S. B., Joswiak D. J., Ishii H. A., Bradley J. P., Chi M., Grossman L., Aléon J., Brownlee D. E., Fallon S., Hutcheon I. D., Matrajt G. and Mckeegan K. D. (2008) A refractory inclusion returned by Stardust from comet 81P/Wild 2. *Meteorit. Planet. Sci.* **43**, 1861–1877.

Simon S. B., Krot A. N. and Nagashima K. (2019) Oxygen and Al-Mg isotopic compositions of grossite-bearing refractory inclusions from CO3 chondrites. *Meteorit. Planet. Sci.* **54**, 1362–1378.

Sugiura N. and Krot A. N. (2007) $^{26}$Al-$^{26}$Mg systematics of Ca-Al-rich inclusions, amoeboid olivine aggregates, and chondrules from the ungrouped carbonaceous chondrite Acfer 094. *Meteorit. Planet. Sci.* **42**, 1183–1195.

1372 Sugiura N., Petaev M. I., Kimura M., Miyazaki A. and Hiyagon H. (2009) Nebular history of
1373 amoeboid olivine aggregates. *Meteorit. Planet. Sci.* **44**, 559–572.
1374 Teng F. Z., Li W. Y., Ke S., Marty B., Dauphas N., Huang S., Wu F. Y. and Pourmand A. (2010)
1375 Magnesium isotopic composition of the Earth and chondrites. *Geochim. Cosmochim. Acta*
1376 **74**, 4150–4166.
1377 Tenner T. J., Nakashima D., Ushikubo T., Kita N. T. and Weisberg M. K. (2015) Oxygen isotope
1378 ratios of FeO-poor chondrules in CR3 chondrites: Influence of dust enrichment and $H_2O$
1379 during chondrule formation. *Geochim. Cosmochim. Acta* **148**, 228–250.
1380 Tenner T. J., Ushikubo T., Nakashima D., Schrader D. L., Weisberg M. K., Kimura M. and Kita
1381 N. T. (2018a) Oxygen Isotope Characteristics of Chondrules from Recent Studies by
1382 Secondary Ion Mass Spectrometry. In *Chondrules* (eds. S. S. Russell, H. C. Connolly, and
1383 A. N. Krot). Cambridge University Press. pp. 196–246.
1384 Tenner T. J., Kimura M. and Kita N. T. (2018b) Further characterizing the extent of
1385 metamorphism within the Dominion Range 08006 CO3 chondrite. *49th Lunar Planet. Sci.*
1386 *Conf.* 1510.
1387 Ushikubo T., Kimura M., Kita N. T. and Valley J. W. (2012) Primordial oxygen isotope
1388 reservoirs of the solar nebula recorded in chondrules in Acfer 094 carbonaceous chondrite.
1389 *Geochim. Cosmochim. Acta* **90**, 242–264.
1390 Ushikubo T., Nakashima D., Kimura M., Tenner T. J. and Kita N. T. (2013) Contemporaneous
1391 formation of chondrules in distinct oxygen isotope reservoirs. *Geochim. Cosmochim. Acta*
1392 **109**, 280–295.
1393 Ushikubo T., Tenner T. J., Hiyagon H. and Kita N. T. (2017) A long duration of the $^{16}O$-rich
1394 reservoir in the solar nebula, as recorded in fine-grained refractory inclusions from the least
1395 metamorphosed carbonaceous chondrites. *Geochim. Cosmochim. Acta* **201**, 103–122.
1396 Van Kooten E. M. M. E., Wielandt D., Schiller M., Nagashima K., Thomen A., Larsen K. K.,
1397 Olsen M. B., Nordlund Å., Krot A. N. and Bizzarro M. (2016) Isotopic evidence for
1398 primordial molecular cloud material in metal-rich carbonaceous chondrites. *Proc. Natl.*

1399 *Acad. Sci.* **113**, 2011–2016.
1400 Wai C. M. and Wasson J. T. (1977) Nebular condensation of moderately volatile elements and
1401 their abundances in ordinary chondrites. *Earth Planet. Sci. Lett.* **36**, 1–13.
1402 Wasserburg G. J., Wimpenny J. and Yin Q.-Z. (2012) Mg isotopic heterogeneity, Al-Mg
1403 isochrons, and canonical $^{26}Al/^{27}Al$ in the early solar system. *Meteorit. Planet. Sci.* **47**, 1980–
1404 1997.
1405 Wasson J. T., Gregory K. W. and Rubin A. E. (1994) Equilibration temperatures of EL
1406 chondrites: A major downward revision in the ferrosilite contents of enstatite. *Meteoritics*
1407 **29**, 658–662.
1408 Weisberg M. K., Prinz M., Clayton R. N. and Mayeda T. K. (1993) The CR (Renazzo-type)
1409 carbonaceous chondrite group and its implications. *Geochim. Cosmochim. Acta* **57**, 1567–
1410 1586.
1411 Weisberg M. K., Connolly H. C. and Ebel D. S. (2004) Petrology and origin of amoeboid olivine
1412 aggregates in CR chondrites. *Meteorit. Planet. Sci.* **39**, 1741–1753.
1413 Yang L. and Ciesla F. J. (2012) The effects of disk building on the distributions of refractory
1414 materials in the solar nebula. *Meteorit. Planet. Sci.* **47**, 99–119.
1415 Young E. D. and Galy A. (2004) The isotope geochemistry and cosmochemistry of magnesium.
1416 *Rev. Mineral. Geochemistry* **55**, 197–230.
1417 Young E. D. and Russell S. S. (1998) Oxygen reservoirs in the early solar nebula inferred from
1418 an Allende CAI. *Science.* **282**, 452–455.
1419
1420 Yurimoto H., Krot A. N., Choi B.-G., Aléon J., Kunihiro T. and Brearley A. J. (2008) Oxygen
1421 Isotopes of Chondritic Components. *Rev. Mineral. Geochemistry* **68**, 141–186.
1422 Zhang M., Bonato E., King A. J., Russell S. S., Tang G. and Lin Y. (2020) Petrology and oxygen
1423 isotopic compositions of calcium-aluminum-rich inclusions in primitive CO3.0-3.1
1424 chondrites. *Meteorit. Planet. Sci.* **55**, 911–935.
1425 Zolensky M. E., Zega T. J., Yano H., Wirick S., Westphal A. J., Weisberg M. K., Weber I.,

Warren J. L., Velbel M. A., Tsuchiyama A., Tsou P., Toppani A., Tomioka N., Tomeoka K., Teslich N., Taheri M., Susini J., Stroud R., Stephan T., Stadermann F. J., Snead C. J., Simon S. B., Simionovici A., See T. H., Robert F., Rietmeijer F. J. M., Rao W., Perronnet M. C., Dimitri A. Papanastassiou 23, Kyoko Okudaira 3, Kazumasa Ohsumi 24, Ohnishi I., Nakamura-Messenger K., Nakamura T., Mostefaoui S., Mikouchi T., Meibom A., Matrajt G., Marcus M. A., Leroux H., Lemelle L., Le L., Lanzirotti A., Langenhorst F., Krot A. N., Keller L. P., Kearsley A. T., Joswiak D. J., Jacob D., Ishii H., Harvey R., Hagiya K., Grossman L., Grossman J. N., Graham G. A., Gounelle M., Gillet P., Genge M., Flynn G. J., Ferroir T., Fallon S., Ebel D. S., Dai Z. R., Cordier P., Clark B., Chi M., Butterworth A. L., Brownlee D. E., Bridges J. C., Brennan S., Brearley A., Bradley J. P., Bleuet P., Bland P. A. and Bastien R. (2006) Mineralogy and petrology of comet 81P/Wild 2 nucleus samples. *Science* **314**, 1735–1739.

**Figure captions**

**Fig. 1.** Oxygen three-isotope ratios of Wild 2 crystalline silicate particles larger than 2 μm with uncertainties of $\Delta^{17}O$ smaller than 5‰. TF, Y&R, CCAM, and PCM represent terrestrial fractionation (Clayton et al., 1991), the Young and Russell (Young and Russell, 1998), the carbonaceous chondrite anhydrous mineral (Clayton et al., 1977), and primitive chondrule mineral (Ushikubo et al., 2012; 2017) lines, respectively. Average values for each particle are shown. Data from [1] McKeegan et al. (2006), [2] Nakamura et al. (2008), [3] Ogliore et al. (2012, 2015), [4] Bridges et al. (2012), [5] Joswiak et al. (2014), [6] Gainsforth et al. (2015), [7] Nakashima et al. (2012), [8] Defouilloy et al. (2017), [9] Chaumard et al. (2018). Two particles, Torajiro and Gozen-sama, that show heterogeneous O isotope ratios within a single particle (Nakamura et al., 2008) are not shown.

1453 **Fig. 2.** SE images of the eight comet 81P/Wild 2 olivine particles before (a-g) and after (h) SIMS
1454 Mg isotope analyses. (a-d) $^{16}$O-rich olivine particles (a) T57/F10, (b) T77/F6, (c) T77/F50, (d)
1455 T175/F1. (e-h) $^{16}$O-depleted olivine particles (e) T77/F4, (f) T77/F7, (g) T149/F11a (and
1456 T149/F11b; not used in this study), (h) T149/F1. For all images, SIMS pits of previous oxygen
1457 isotope analyses are visible (Nakashima et al., 2012; Defouilloy et al., 2017; Chaumard et al.,
1458 2018). FIB marks for Mg isotope analyses can be seen as squares at the surface of the grains (a-
1459 g). For T149/F1, SIMS pits for 6 oxygen isotope analyses (Defouilloy et al., 2017) and four Mg
1460 isotope analyses (this study; #1-4) are visible. Additional images can be found in Electronic
1461 Annex EA1.
1462
1463 **Fig. 3.** BSE images of compact AOAs from Kaba and DOM 08006. (a-c) K27 from Kaba, (d-e)
1464 513 from DOM 08006, (f-g) 505 from DOM 08006. Mineral phases shown are olivine (Ol),
1465 anorthite (An), spinel (Sp) and Al diopside (Al-di).
1466
1467 **Fig. 4.** BSE images of pore-rich, low-Ca pyroxene-bearing AOAs from DOM 08006. (a-d) 502,
1468 (e-g) 503. Mineral phases shown are olivine (Ol), low-Ca pyroxene (Lpx), Al diopside (Al-di),
1469 anorthite (An) and Fe,Ni-metal (FeNi). Pores, and haloes that represent diffuse area consisting of
1470 mixtures of tiny Al-diopside grains and forsterite, are indicated.
1471
1472 **Fig. 5.** BSE images of pore-rich AOAs from DOM 08006. (a) 501, (b) pore-rich lithology in 501,
1473 (c) compact lithology in 501, (d) 511, (e) 512, (f) 514. The locations of Mg isotope analyses for
1474 pore-rich and compact lithologies in AOA 501 are indicated in (b-c). Mineral phases shown are
1475 olivine (Ol), Al-diopside (Al-di) and anorthite (An).
1476
1477 **Fig. 6.** Oxygen three-isotope ratios of the eight AOA olivines from Kaba (K27) and DOM 08006
1478 (501, 502, 503, 505, 511, 513, 514). All measured data (= individual olivine analyses) are shown
1479 in (a). The insert in (a) shows detail of the analyses highlighted by the dotted box. Average $\delta^{17,}$

$^{18}O$ values of each AOA are shown in (b), though for three AOAs (502, 503, 511) only a single analysis was collected. For comparison, data for AOAs from Acfer 094 (Ushikubo et al., 2017) are also shown in (b). Reference lines are the terrestrial fractionation (TF), the carbonaceous chondrite anhydrous mineral (CCAM), the Young and Russell (Y&R), and the primitive chondrule mineral (PCM) lines. Errors are 2SD for data obtained in this study. Errors for Acfer 094 data are propagated, as described in Ushikubo et al. (2017).

**Fig. 7.** Magnesium-three isotope ratios of the eight AOA olivines from Kaba and DOM 08006. All measured data are shown in (a). (b-i) Individual AOA diagrams from Kaba (b) and DOM 08006 (c-i). Square symbols represent the Mg isotope ratios of bulk chondrites ([1] Teng et al., 2010). Solid lines represent a best-fit line for all the measured data determined by a least squares fitting (Ludwig, 2012). Errors are 2σ.

**Fig. 8.** Relationships between $\delta^{25}Mg'_{DSM-3}$ and $\delta^{26}Mg'_{DSM-3}$ values of individual AOA olivine analyses. The square symbol represents the Mg isotope ratios of bulk chondrites ([1] Teng et al., 2010). The solid line represents a linear regression line (Isoplot model 1; Ludwig, 2012) for all AOA data (N = 36) obtained in this study. The dotted curves are error envelopes that show 95% confidence limits. Note that uncertainties of $\delta^{25}Mg'_{DSM-3}$ and $\delta^{26}Mg'_{DSM-3}$ values were not propagated from those related to instrumental mass fractionation. See more details in Electronic Annex EA5.

**Fig. 9.** Magnesium-three isotope ratios of the five Wild 2 olivine particles studied. The red square symbol represents the Mg isotope ratios of bulk chondrites ([1] Teng et al., 2010). All measured AOA data (Fig. 7a) are shown for comparison. Errors for Wild 2 olivine data are 2σ. For clarity, errors for AOA data are not shown.

**Fig. 10.** $\delta^{26}Mg^{*}$-$\delta^{25}Mg_{DSM-3}$ plot for AOA olivines (Kaba and DOM 08006) and the five Wild 2 olivine particles studied.

**Fig. 11.** FeO contents (wt%) of AOA olivines from Kaba and DOM 08006. Data obtained with FE-EPMA (open symbols) and SIMS (closed symbols) are shown. Data obtained with FE-EPMA might be overestimated due to secondary fluorescence effects (see section 5.3.2). The dotted line represents the detection limit (0.05 wt%) for FE-EPMA analyses.

**Fig. 12.** Minor element systematics of $^{16}O$-rich Wild 2 olivine particles (T57/F10, T77/F50, and T175/F1) and AOA olivines from Kaba and DOM 08006 obtained by SIMS. (a and c) CrO contents as functions of (a) CaO and (c) FeO. (b and d) MnO contents as functions of (b) CaO and (d) FeO. Equilibrium condensation trajectories at $10^{-4}$ bar with dust enrichment factor = 1 (nominal solar composition shown by solid curve), 2 (dashed curve), and 5 (dotted curve) calculated by Sugiura et al. (2009) are shown for comparison. Data for T57/F10 are not shown in (c) and (d) because of its high FeO content (1.75 wt%).

**Fig. 13.** Relationships among Mg isotope ratios and minor element abundances of $^{16}O$-rich Wild 2 olivine particles T57/F10, T77/F50, and T175/F1, and AOA olivines from Kaba and DOM 08006 obtained by SIMS. Open circle symbols represent AOA olivines with compact textures (compact AOA), while closed circle, diamond, and half-closed square symbols represent AOA olivines with pore-rich textures (pore-rich AOA; see section 5.3.1 for details). The dotted lines represent the Mg isotope ratio of bulk chondrites (Teng et al., 2010). (a) $\delta^{25}Mg_{DSM-3}$ values of three $^{16}O$-rich Wild 2 particles and AOA olivines with different textures (compact versus pore-rich). (b-e) $\delta^{25}Mg_{DSM-3}$ values as functions of (b) CrO, (c) CaO, (d) MnO contents (wt%) and (e) MnO/FeO (wt%) ratio. Errors are 2σ.

**Fig. 14.** $\delta^{25}Mg_{DSM-3}$ values as a function of estimated condensation temperatures for $^{16}O$-rich Wild 2 olivine particles T57/F10, T77/F50, and T175/F1, and AOA olivines from Kaba and DOM 08006. Condensation trajectories of $\delta^{25}Mg$ as a function of condensation temperature and the timescale parameter $\varepsilon$ modeled by Richter (2004) are shown for comparison (solid line with $\varepsilon$ = 0.01 and dotted line with $\varepsilon$ = 0.001). Fractions of magnesium condensed as forsterite with $\varepsilon$ = 0.01 are also shown at the top of the plot. Condensation temperatures (X axis for each data point) are estimated by comparing CrO contents obtained by SIMS and an equilibrium condensation calculation at $10^{-4}$ bar with a dust enrichment factor of 1 (nominal solar composition) from Sugiura et al. (2009). Although negative Mg isotope fractionations suggest formation by disequilibrium condensation, we assume the CrO contents of olivine reflect their condensation temperatures (see section 5.3.3 for more details). This assumption may result in additional uncertainties of estimated temperatures.

**Appendices**

Electronic Annex EA1: SE images of Wild 2 olivine particles after (1) FIB marking, (2) Mg isotope analysis, and (3) Minor element analysis

Electronic Annex EA2: Position of SIMS measurements on AOAs (Oxygen isotopes)

Electronic Annex EA3: Position of SIMS measurements on AOAs (Magnesium isotopes and minor elements)

Electronic Annex EA4: Research data (EA4-1. SIMS O isotope data; EA4-2. SIMS Mg isotope data; EA4-3. SIMS major and minor element analyses data; EA4-4. EPMA data; EA4-5. Time-constant values for three $\Omega^{12}$ ohm feedback resisters)

Electronic Annex EA5: SIMS data reduction procedure

Electronic Annex EA6: Position of EPMA measurements on AOAs

Electronic Annex EA7: Descriptions for SIMS analyses of T77/F6, T77/F7, and T149/F11a

Table 1
Mineralogy of AOAs from Kaba (CV3.1) and DOM 08006 (CO3.01) carbonaceous chondrites

| Chondrite | AOA name | AOA texture | fo | FeNi | Ca-, Al-rich portions | | | | LIME ol[b] | lpx |
|---|---|---|---|---|---|---|---|---|---|---|
| | | | | | Al-(Ti)-di | an | sp | halo[a] | | |
| Kaba | K27 | compact | + | + | + | + | + | − | − | − |
| DOM 08006 | 501 | pore-rich | + | + | + | + | − | + | + | − |
| DOM 08006 | 502 | pore-rich | + | + | + | + | − | + | + | + |
| DOM 08006 | 503 | pore-rich | + | + | + | + | − | + | + | + |
| DOM 08006 | 505 | compact | + | + | + | − | + | − | + | − |
| DOM 08006 | 511 | pore-rich | + | + | + | + | − | + | + | − |
| DOM 08006 | 512 | pore-rich | + | + | + | + | − | + | + | − |
| DOM 08006 | 513 | compact | + | + | + | + | + | − | − | − |
| DOM 08006 | 514 | pore-rich | + | + | + | + | − | + | − | − |

[a] Diffuse area that appears to be brighter in BSE images than surrounding forsterite. See section 4.1.
[b] Olivine grains with MnO/FeO (wt%) ≥ 1. The MnO/FeO ratios are calculated from SIMS data in Table 4, except for AOA 514. The MnO/FeO ratios of olivine grains from AOA 514 are calculated from FE-EPMA data due to an absence of SIMS minor element data.
fo = forsterite, FeNi = Fe,Ni-metal and/or weathering products, Al-(Ti)-di = Al-(Ti) diopside, an = anorthite, sp = spinel, LIME ol = LIME olivine, lpx = low-Ca pyroxene

Table 2
Fo, En, and Wo contents and average elemental compositions (wt%) of minerals in Kaba and DOM 08006 AOAs obtained with electron microprobe.

| Chondrite | AOA name | Mineral[a] | Fo[b] | 1SD | En[b] | 1SD | Wo[b] | 1SD | No. of analyses | $Na_2O$ | MgO | $Al_2O_3$ | $SiO_2$ | $K_2O$ | CaO | $TiO_2$ | $Cr_2O_3$ | MnO | FeO | Total |
|---|---|---|---|---|---|---|---|---|---|---|---|---|---|---|---|---|---|---|---|---|
| Kaba | K27 | fo | 99.9 | 0.1 | | | | | 15 | b.d. | 57.17 | 0.06 | 42.31 | b.d. | 0.15 | 0.06 | 0.20 | 0.10 | 0.19 | 100.23 |
| Kaba | K27 | hpx | | | 48.9 | 1.4 | 51.1 | 1.4 | 2 | b.d. | 17.15 | 5.32 | 50.88 | b.d. | 24.88 | 1.94 | 0.11 | b.d. | b.d. | 100.29 |
| DOM 08006 | 501 | fo | 99.5 | 0.3 | | | | | 12 | b.d. | 57.04 | 0.06 | 42.24 | b.d. | 0.19 | 0.05 | 0.16 | 0.11 | 0.49 | 100.34 |
| DOM 08006 | 502 | fo | 99.5 | 0.2 | | | | | 7 | b.d. | 57.14 | 0.05 | 42.35 | b.d. | 0.07 | 0.10 | 0.34 | 0.27 | 0.48 | 100.81 |
| DOM 08006 | 503 | fo | 99.7 | 0.1 | | | | | 7 | b.d. | 57.61 | 0.05 | 42.50 | b.d. | 0.09 | 0.06 | 0.22 | 0.10 | 0.34 | 100.96 |
| DOM 08006 | 505 | fo | 99.8 | 0.1 | | | | | 7 | b.d. | 57.56 | 0.04 | 42.15 | b.d. | 0.11 | 0.06 | 0.20 | 0.12 | 0.18 | 100.41 |
| DOM 08006 | 505 | hpx | | | 50.1 | 0.1 | 49.6 | 0.2 | 3 | b.d. | 18.12 | 3.87 | 53.00 | b.d. | 24.92 | 0.28 | 0.09 | b.d. | 0.20 | 100.48 |
| DOM 08006 | 511 | fo | 99.5 | 0.1 | | | | | 7 | b.d. | 57.36 | 0.04 | 42.17 | b.d. | 0.12 | 0.05 | 0.13 | 0.16 | 0.54 | 100.56 |
| DOM 08006 | 511 | hpx | | | 45.1 | 1.6 | 54.3 | 1.4 | 2 | b.d. | 14.90 | 10.17 | 47.95 | b.d. | 24.90 | 2.07 | 0.10 | b.d. | 0.35 | 100.44 |
| DOM 08006 | 511 | an | | | | | | | 1 | 0.03 | 0.55 | 35.94 | 42.55 | b.d. | 19.84 | 0.07 | 0.08 | b.d. | 0.37 | 99.43 |
| DOM 08006 | 512 | fo | 99.7 | 0.1 | | | | | 7 | b.d. | 57.35 | 0.08 | 42.32 | b.d. | 0.09 | 0.08 | 0.27 | 0.15 | 0.27 | 100.61 |
| DOM 08006 | 513 | fo | 99.6 | 0.1 | | | | | 7 | b.d. | 57.32 | 0.04 | 42.44 | b.d. | 0.33 | 0.05 | 0.10 | b.d. | 0.40 | 100.69 |
| DOM 08006 | 513 | hpx | | | 47.9 | 1.1 | 51.4 | 1.2 | 4 | b.d. | 16.63 | 6.85 | 50.15 | b.d. | 24.83 | 1.38 | 0.10 | b.d. | 0.46 | 100.40 |
| DOM 08006 | 514 | fo | 99.7 | 0.2 | | | | | 7 | b.d. | 57.40 | 0.07 | 42.36 | b.d. | 0.35 | 0.07 | 0.07 | b.d. | 0.33 | 100.65 |

[a] fo = forsterite, hpx = high-Ca pyroxene, an = anorthite
[b] Fo = Mg/(Mg + Fe) molar %, En = Mg/(Mg + Fe + Ca) molar %, Wo = Ca/(Mg + Fe + Ca) molar %.

Table 3
Oxygen isotope ratios of AOA olivines from Kaba and DOM 08006

| Sample/Location #[a] | $\delta^{18}O$ (‰) | Unc. (2σ) | $\delta^{17}O$ (‰) | Unc. (2σ) | $\Delta^{17}O$ (‰) | Unc. (2σ) |
|---|---|---|---|---|---|---|
| Kaba (CV3.1) | | | | | | |
| K27 | | | | | | |
| #1 | -44.6 | 0.5 | -47.0 | 0.9 | -23.8 | 1.0 |
| #2 | -45.1 | 0.5 | -47.2 | 0.9 | -23.7 | 1.0 |
| #3 | -44.0 | 0.5 | -46.8 | 0.9 | -24.0 | 1.0 |
| #4 | -45.2 | 0.5 | -47.2 | 0.9 | -23.7 | 1.0 |
| #5 | -45.7 | 0.5 | -46.8 | 0.9 | -23.0 | 1.0 |
| #6 | -45.4 | 0.5 | -47.1 | 0.9 | -23.5 | 1.0 |
| #7 | -45.6 | 0.4 | -48.2 | 0.7 | -24.5 | 0.7 |
| #8 | -45.1 | 0.4 | -48.1 | 0.7 | -24.7 | 0.7 |
| #9 | -45.6 | 0.4 | -48.3 | 0.7 | -24.6 | 0.7 |
| #10 | -46.1 | 0.4 | -47.7 | 0.7 | -23.7 | 0.7 |
| Average & 2SD | -45.2 | 1.2 | -47.5 | 1.2 | -23.9 | 1.1 |
| DOM 08006 (CO3.01) | | | | | | |
| 501 | | | | | | |
| #1 | -46.4 | 0.2 | -47.4 | 0.9 | -23.3 | 0.8 |
| #2 | -45.7 | 0.2 | -47.7 | 0.9 | -23.9 | 0.8 |
| #3 | -46.2 | 0.2 | -47.9 | 0.9 | -23.9 | 0.8 |
| #4 | -45.9 | 0.2 | -48.1 | 0.9 | -24.2 | 0.8 |
| #5 | -46.5 | 0.2 | -47.7 | 0.9 | -23.5 | 0.8 |
| Average & 2SD | -46.1 | 0.7 | -47.8 | 0.5 | -23.8 | 0.7 |
| 502 | | | | | | |
| #1 | -46.2 | 0.2 | -48.2 | 0.9 | -24.2 | 0.8 |
| 503 | | | | | | |
| #1 | -45.9 | 0.2 | -47.5 | 0.9 | -23.7 | 0.8 |
| 505 | | | | | | |
| #1 | -46.5 | 0.4 | -48.0 | 0.7 | -23.8 | 0.7 |
| #2 | -45.9 | 0.4 | -47.3 | 0.7 | -23.5 | 0.7 |
| #3 | -46.4 | 0.4 | -48.1 | 0.7 | -24.0 | 0.7 |
| Average & 2SD | -46.3 | 0.7 | -47.8 | 0.8 | -23.8 | 0.5 |
| 511 | | | | | | |
| #1 | -45.4 | 0.4 | -47.7 | 0.7 | -24.1 | 0.7 |
| 513 | | | | | | |
| #1 | -45.5 | 0.2 | -48.0 | 0.9 | -24.3 | 0.8 |
| #2 | -46.0 | 0.2 | -48.3 | 0.9 | -24.4 | 0.8 |
| #3 | -45.9 | 0.2 | -47.7 | 0.9 | -23.9 | 0.8 |
| #4 | -45.6 | 0.2 | -47.5 | 0.9 | -23.8 | 0.8 |
| Average & 2SD | -45.8 | 0.4 | -47.9 | 0.7 | -24.1 | 0.6 |
| 514 | | | | | | |
| #1 | -45.5 | 0.4 | -47.7 | 0.7 | -24.0 | 0.7 |
| #2 | -45.9 | 0.4 | -47.7 | 0.7 | -23.8 | 0.7 |
| #3 | -45.8 | 0.4 | -48.1 | 0.7 | -24.3 | 0.7 |
| #4 | -47.4 | 0.4 | -49.1 | 0.7 | -24.5 | 0.7 |
| #5 | -45.5 | 0.4 | -47.9 | 0.7 | -24.2 | 0.7 |
| #6 | -45.6 | 0.4 | -48.6 | 0.7 | -24.8 | 0.7 |
| #7 | -45.8 | 0.4 | -47.9 | 0.7 | -24.1 | 0.7 |
| Average & 2SD | -45.9 | 1.3 | -48.1 | 1.1 | -24.3 | 0.7 |

[a] Analysis points are shown in Electronic Annex EA2.

Table 4
Magnesium isotope ratios and minor elemental abundances of AOA olivine from Kaba and DOM 08006 obtained with SIMS

| Sample/Location #[a] | $\delta^{25}Mg_{DSM-3}$ (‰) | Unc. (+/−) (2σ) | | $\delta^{26}Mg_{DSM-3}$ (‰) | Unc. (+/−) (2σ) | | $\delta^{26}Mg^{*}$ (‰) | Unc. (2σ) | CaO (wt%) | Unc. (2σ) | $Cr_2O_3$ (wt%) | Unc. (2σ) | FeO (wt%) | Unc. (2σ) | MnO (wt%) | Unc. (2σ) | MnO/FeO | Unc. (2σ) |
|---|---|---|---|---|---|---|---|---|---|---|---|---|---|---|---|---|---|---|
| Kaba (CV3.1) | | | | | | | | | | | | | | | | | | |
| K27 | | | | | | | | | | | | | | | | | | |
| #3[b] | -0.39 | 0.30 | 0.31 | -0.68 | 0.59 | 0.59 | 0.04 | 0.06 | 0.128 | 0.004 | 0.110 | 0.007 | 0.324 | 0.017 | 0.027 | 0.002 | 0.08 | 0.01 |
| #4 | -0.42 | 0.31 | 0.31 | -0.78 | 0.60 | 0.60 | -0.01 | 0.06 | 0.150 | 0.005 | 0.081 | 0.005 | 0.064 | 0.002 | 0.008 | 0.002 | 0.13 | 0.04 |
| #5 | -0.25 | 0.30 | 0.31 | -0.48 | 0.59 | 0.59 | -0.03 | 0.06 | 0.158 | 0.005 | 0.083 | 0.005 | 0.065 | 0.003 | 0.008 | 0.001 | 0.12 | 0.02 |
| #6 | -0.51 | 0.30 | 0.33 | -0.95 | 0.59 | 0.62 | 0.00 | 0.06 | 0.230 | 0.022 | 0.057 | 0.004 | 0.116 | 0.003 | 0.009 | 0.001 | 0.08 | 0.01 |
| #7 | -0.64 | 0.31 | 0.31 | -1.21 | 0.60 | 0.60 | -0.01 | 0.06 | 0.202 | 0.017 | 0.113 | 0.007 | 0.072 | 0.003 | 0.024 | 0.001 | 0.34 | 0.02 |
| #8 | -0.69 | 0.31 | 0.31 | -1.12 | 0.60 | 0.60 | 0.16 | 0.06 | 0.136 | 0.005 | 0.105 | 0.007 | 0.081 | 0.003 | 0.007 | 0.002 | 0.09 | 0.02 |
| #9[b] | -0.23 | 0.32 | 0.32 | -0.38 | 0.61 | 0.61 | 0.01 | 0.06 | 0.089 | 0.006 | 0.138 | 0.012 | 0.184 | 0.006 | 0.098 | 0.004 | 0.53 | 0.03 |
| Average & 2SD | -0.45 | 0.35 | 0.35 | -0.80 | 0.63 | 0.63 | 0.02 | 0.13 | 0.156 | 0.094 | 0.098 | 0.037 | 0.129 | 0.192 | 0.026 | 0.066 | 0.20 | 0.59 |
| DOM 08006 (CO3.01) | | | | | | | | | | | | | | | | | | |
| 501 | | | | | | | | | | | | | | | | | | |
| #1_outer left part[c] | -0.42 | 0.44 | 0.44 | -0.55 | 0.87 | 0.87 | 0.17 | 0.24 | 0.119 | 0.003 | 0.188 | 0.006 | 0.072 | 0.003 | 0.088 | 0.001 | 1.21 | 0.06 |
| #2 | -3.31 | 0.44 | 0.44 | -6.27 | 0.86 | 0.86 | 0.09 | 0.24 | 0.082 | 0.002 | 0.177 | 0.010 | 0.073 | 0.002 | 0.108 | 0.004 | 1.49 | 0.07 |
| #3 | -2.90 | 0.40 | 0.40 | -5.50 | 0.80 | 0.80 | 0.10 | 0.24 | 0.165 | 0.005 | 0.100 | 0.005 | 0.058 | 0.002 | 0.032 | 0.003 | 0.55 | 0.05 |
| #4 | -3.30 | 0.42 | 0.42 | -6.21 | 0.84 | 0.84 | 0.15 | 0.24 | 0.189 | 0.004 | 0.072 | 0.003 | 0.052 | 0.001 | 0.028 | 0.002 | 0.54 | 0.04 |
| #5_outer left part[c] | -0.66 | 0.43 | 0.43 | -1.20 | 0.85 | 0.85 | 0.01 | 0.24 | 0.151 | 0.005 | 0.117 | 0.005 | 0.071 | 0.003 | 0.078 | 0.007 | 1.10 | 0.11 |
| #6 | -3.79 | 0.45 | 0.45 | -7.27 | 0.92 | 0.92 | 0.05 | 0.21 | 0.128 | 0.003 | 0.093 | 0.004 | 0.059 | 0.002 | 0.051 | 0.003 | 0.87 | 0.06 |
| #7 | -3.08 | 0.46 | 0.46 | -5.85 | 0.93 | 0.93 | 0.05 | 0.21 | 0.142 | 0.003 | 0.163 | 0.005 | 0.073 | 0.002 | 0.093 | 0.003 | 1.28 | 0.05 |
| Average (outer left) & 2SD | -0.54 | 0.34 | 0.34 | -0.87 | 0.93 | 0.93 | 0.09 | 0.24 | 0.135 | 0.046 | 0.153 | 0.100 | 0.072 | 0.003 | 0.083 | 0.014 | 1.16 | 0.21 |
| Average (#2-4 & #6-7) & 2SD | -3.28 | 0.67 | 0.67 | -6.22 | 1.32 | 1.32 | 0.09 | 0.08 | 0.142 | 0.081 | 0.121 | 0.093 | 0.063 | 0.019 | 0.063 | 0.073 | 0.99 | 1.19 |
| 502 | | | | | | | | | | | | | | | | | | |
| #1 | -0.62 | 0.44 | 0.44 | -1.16 | 0.85 | 0.85 | -0.05 | 0.24 | 0.033 | 0.001 | 0.320 | 0.011 | 0.063 | 0.002 | 0.074 | 0.003 | 1.18 | 0.06 |
| #2 | -0.58 | 0.44 | 0.44 | -0.87 | 0.85 | 0.85 | 0.14 | 0.24 | 0.045 | 0.002 | 0.316 | 0.010 | 0.078 | 0.004 | 0.084 | 0.004 | 1.08 | 0.08 |
| #3 | -0.59 | 0.41 | 0.41 | -0.92 | 0.77 | 0.77 | 0.13 | 0.24 | 0.037 | 0.002 | 0.321 | 0.011 | 0.075 | 0.002 | 0.314 | 0.015 | 4.20 | 0.23 |
| #4 | -0.50 | 0.40 | 0.40 | -0.90 | 0.77 | 0.77 | -0.03 | 0.24 | 0.037 | 0.001 | 0.295 | 0.010 | 0.072 | 0.002 | 0.283 | 0.002 | 3.92 | 0.10 |
| Average & 2SD | -0.57 | 0.11 | 0.11 | -0.96 | 0.26 | 0.26 | 0.05 | 0.21 | 0.038 | 0.010 | 0.313 | 0.017 | 0.072 | 0.013 | 0.189 | 0.255 | 2.62 | 3.57 |
| 503 | | | | | | | | | | | | | | | | | | |
| #1 | -1.72 | 0.45 | 0.45 | -3.34 | 0.93 | 0.93 | -0.07 | 0.21 | 0.039 | 0.001 | 0.212 | 0.008 | 0.062 | 0.003 | 0.088 | 0.002 | 1.42 | 0.07 |
| #2 | -1.85 | 0.44 | 0.44 | -3.48 | 0.91 | 0.91 | 0.06 | 0.21 | 0.063 | 0.001 | 0.164 | 0.006 | 0.061 | 0.002 | 0.024 | 0.002 | 0.40 | 0.04 |
| #3 | -2.06 | 0.46 | 0.46 | -3.87 | 0.94 | 0.94 | 0.05 | 0.21 | 0.052 | 0.003 | 0.195 | 0.008 | 0.063 | 0.002 | 0.042 | 0.002 | 0.67 | 0.05 |
| #4 | -2.26 | 0.47 | 0.47 | -4.24 | 0.94 | 0.94 | 0.06 | 0.21 | 0.052 | 0.002 | 0.152 | 0.005 | 0.072 | 0.004 | 0.067 | 0.003 | 0.93 | 0.07 |
| Average & 2SD | -1.97 | 0.48 | 0.48 | -3.74 | 0.81 | 0.81 | 0.03 | 0.13 | 0.051 | 0.020 | 0.181 | 0.039 | 0.065 | 0.010 | 0.055 | 0.056 | 0.86 | 0.87 |
| 505 | | | | | | | | | | | | | | | | | | |
| #1 | -0.86 | 0.46 | 0.46 | -1.51 | 0.94 | 0.94 | 0.08 | 0.21 | 0.060 | 0.001 | 0.259 | 0.010 | 0.080 | 0.004 | 0.135 | 0.006 | 1.70 | 0.11 |
| #2 | -0.68 | 0.40 | 0.40 | -1.18 | 0.84 | 0.84 | 0.13 | 0.21 | 0.079 | 0.003 | 0.128 | 0.004 | 0.058 | 0.003 | 0.026 | 0.002 | 0.45 | 0.05 |
| #3 | -1.17 | 0.42 | 0.42 | -2.30 | 0.88 | 0.88 | -0.06 | 0.21 | 0.066 | 0.002 | 0.179 | 0.006 | 0.062 | 0.002 | 0.073 | 0.002 | 1.18 | 0.05 |
| #4 | -1.06 | 0.41 | 0.41 | -2.15 | 0.86 | 0.86 | -0.10 | 0.21 | 0.075 | 0.003 | 0.129 | 0.004 | 0.057 | 0.002 | 0.019 | 0.002 | 0.33 | 0.03 |
| Average & 2SD | -0.94 | 0.44 | 0.44 | -1.79 | 1.05 | 1.05 | 0.02 | 0.22 | 0.070 | 0.017 | 0.174 | 0.087 | 0.064 | 0.021 | 0.063 | 0.108 | 0.99 | 1.71 |
| 511 | | | | | | | | | | | | | | | | | | |
| #1 | -2.36 | 0.44 | 0.44 | -4.49 | 0.86 | 0.86 | 0.08 | 0.25 | 0.090 | 0.002 | 0.096 | 0.006 | 0.046 | 0.003 | 0.020 | 0.003 | 0.44 | 0.06 |
| #2 | -2.91 | 0.48 | 0.48 | -5.57 | 0.92 | 0.92 | 0.00 | 0.25 | 0.077 | 0.002 | 0.123 | 0.005 | 0.044 | 0.003 | 0.090 | 0.005 | 2.02 | 0.16 |
| #3 | -2.52 | 0.43 | 0.43 | -5.02 | 0.85 | 0.85 | -0.15 | 0.25 | 0.101 | 0.002 | 0.128 | 0.007 | 0.044 | 0.001 | 0.095 | 0.002 | 2.14 | 0.08 |
| #4 | -3.34 | 0.46 | 0.46 | -6.41 | 0.89 | 0.89 | 0.03 | 0.25 | 0.109 | 0.005 | 0.113 | 0.007 | 0.056 | 0.003 | 0.005 | 0.001 | 0.09 | 0.01 |
| Average & 2SD | -2.78 | 0.87 | 0.87 | -5.37 | 1.64 | 1.64 | -0.01 | 0.20 | 0.094 | 0.027 | 0.115 | 0.020 | 0.048 | 0.011 | 0.052 | 0.093 | 1.10 | 1.97 |
| 512 | | | | | | | | | | | | | | | | | | |
| #1 | -1.09 | 0.47 | 0.47 | -1.96 | 0.94 | 0.94 | 0.05 | 0.21 | 0.040 | 0.001 | 0.273 | 0.009 | 0.068 | 0.002 | 0.215 | 0.003 | 3.18 | 0.10 |
| #2 | -1.10 | 0.47 | 0.47 | -1.97 | 0.94 | 0.94 | 0.06 | 0.21 | 0.037 | 0.001 | 0.233 | 0.008 | 0.068 | 0.002 | 0.088 | 0.002 | 1.28 | 0.05 |
| #3 | -1.25 | 0.46 | 0.46 | -2.30 | 0.92 | 0.92 | 0.03 | 0.21 | 0.032 | 0.001 | 0.245 | 0.008 | 0.066 | 0.002 | 0.048 | 0.002 | 0.73 | 0.04 |
| Average & 2SD | -1.15 | 0.18 | 0.18 | -2.08 | 0.38 | 0.38 | 0.05 | 0.04 | 0.036 | 0.008 | 0.250 | 0.029 | 0.067 | 0.003 | 0.117 | 0.174 | 1.74 | 2.59 |
| 513 | | | | | | | | | | | | | | | | | | |
| #1 | -0.47 | 0.42 | 0.42 | -0.78 | 0.82 | 0.82 | 0.13 | 0.25 | 0.269 | 0.006 | 0.055 | 0.003 | 0.042 | 0.003 | 0.0039 | 0.0009 | 0.09 | 0.02 |
| #2 | -0.83 | 0.45 | 0.45 | -1.44 | 0.87 | 0.87 | 0.12 | 0.25 | 0.249 | 0.006 | 0.062 | 0.004 | 0.032 | 0.001 | 0.0046 | 0.0011 | 0.14 | 0.03 |
| #3 | -0.57 | 0.44 | 0.44 | -1.02 | 0.86 | 0.86 | 0.06 | 0.25 | 0.283 | 0.007 | 0.078 | 0.004 | 0.039 | 0.001 | 0.0040 | 0.0005 | 0.10 | 0.01 |
| Average & 2SD | -0.62 | 0.37 | 0.37 | -1.08 | 0.67 | 0.67 | 0.10 | 0.08 | 0.267 | 0.035 | 0.065 | 0.017 | 0.038 | 0.010 | 0.004 | 0.001 | 0.11 | 0.04 |

[a] Analysis points are shown in Electronic Annex EA3.
[b] Average values are listed for minor element data. Individual data are reported in Electronic Annex EA4-3-3.
[c] These data are obtained from an outer left part of AOA 501, which shows compact textures relative to the most part of this AOA.

Table 5
Magnesium isotope ratios and minor elemental abundances of Wild 2 olivine particles obtained with SIMS

| Sample/Location #[a] | $\delta^{25}Mg_{DSM-3}$ (‰) | Unc. (+/−) (2σ) | | $\delta^{26}Mg_{DSM-3}$ (‰) | Unc. (+/−) (2σ) | | $\delta^{26}Mg^{*}$ (‰) | Unc. (2σ) | CaO (wt%) | Unc. (2σ) | $Cr_2O_3$ (wt%) | Unc. (2σ) | FeO (wt%) | Unc. (2σ) | MnO (wt%) | Unc. (2σ) | MnO/FeO | Unc. (2σ) |
|---|---|---|---|---|---|---|---|---|---|---|---|---|---|---|---|---|---|---|
| $^{16}$O-depleted particles | | | | | | | | | | | | | | | | | | |
| T77/F4 | | | | | | | | | | | | | | | | | | |
| #1 | -0.17 | 0.77 | 0.51 | -0.46 | 1.17 | 0.87 | -0.07 | 0.43 | 0.186 | 0.015 | 0.07 | 0.01 | 29.72 | 0.99 | 0.481 | 0.005 | 0.016 | 0.001 |
| T149/F1 | | | | | | | | | | | | | | | | | | |
| #1 | -0.53 | 0.70 | 0.70 | -0.74 | 1.05 | 1.05 | -0.06 | 0.76 | 0.115 | 0.009 | 0.51 | 0.05 | 12.24 | 0.41 | 0.332 | 0.008 | 0.027 | 0.001 |
| #2 | -0.40 | 0.70 | 0.70 | -0.78 | 1.05 | 1.05 | -0.33 | 0.76 | 0.116 | 0.009 | 0.53 | 0.06 | 12.84 | 0.43 | 0.342 | 0.008 | 0.027 | 0.001 |
| #3 | -0.36 | 0.70 | 0.70 | -0.77 | 1.05 | 1.05 | -0.41 | 0.76 | --- | --- | --- | --- | --- | --- | --- | --- | --- | --- |
| #4 | -0.70 | 0.70 | 0.70 | -0.87 | 1.05 | 1.05 | 0.16 | 0.76 | --- | --- | --- | --- | --- | --- | --- | --- | --- | --- |
| Average & 2SD | -0.50 | 0.30 | 0.30 | -0.79 | 0.11 | 0.11 | -0.16 | 0.52 | 0.116 | 0.001 | 0.52 | 0.03 | 12.54 | 0.85 | 0.337 | 0.014 | 0.027 | 0.002 |
| $^{16}$O-rich particles | | | | | | | | | | | | | | | | | | |
| T57/F10 | | | | | | | | | | | | | | | | | | |
| #1 | 0.56 | 0.47 | 0.63 | 1.40 | 0.97 | 1.30 | 0.15 | 0.45 | 0.043 | 0.003 | 0.42 | 0.05 | 1.75 | 0.06 | 0.664 | 0.016 | 0.38 | 0.02 |
| T77/F50 | | | | | | | | | | | | | | | | | | |
| #1 | -0.97 | 0.41 | 0.49 | -1.68 | 0.76 | 1.01 | 0.08 | 0.71 | --- | --- | --- | --- | --- | --- | --- | --- | --- | --- |
| #2 | -0.93 | 0.41 | 0.49 | -1.69 | 0.76 | 1.01 | -0.01 | 0.70 | 0.031 | 0.002 | 0.31 | 0.03 | 0.065 | 0.003 | 0.247 | 0.004 | 3.80 | 0.16 |
| #3 | -0.60 | 0.41 | 0.49 | -0.94 | 0.76 | 1.01 | 0.11 | 0.70 | --- | --- | --- | --- | --- | --- | --- | --- | --- | --- |
| Average & 2SD | -0.83 | 0.40 | 0.40 | -1.44 | 0.87 | 0.87 | 0.06 | 0.13 | | | | | | | | | | |
| T175/F1 | | | | | | | | | | | | | | | | | | |
| #1 | -0.48 | 0.51 | 0.62 | -0.47 | 1.04 | 1.26 | 0.31 | 0.37 | 0.0038 | 0.0003 | 0.15 | 0.02 | 0.151 | 0.015 | 0.055 | 0.004 | 0.37 | 0.05 |

[a] Analysis points are shown in Electronic Annex EA1.

Fig. 1

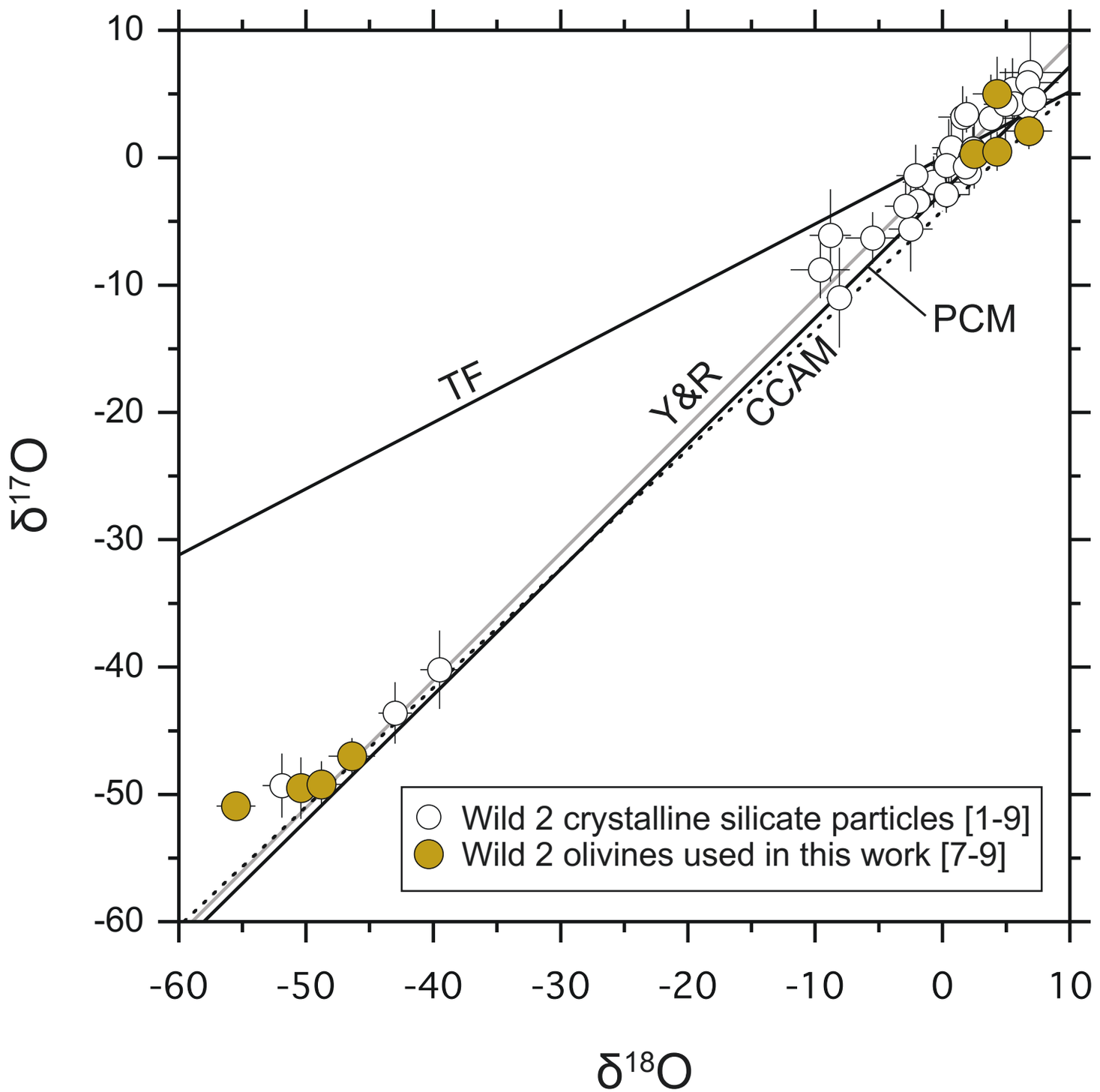
10
0
-10
-20
-30
-40
-50
-60
-60
-50
-40
-30
-20
-10
0
10
δ17O
δ18O
TF
Y&R
CCAM
PCM
Wild 2 crystalline silicate particles [1-9]
Wild 2 olivines used in this work [7-9]

Fig. 2

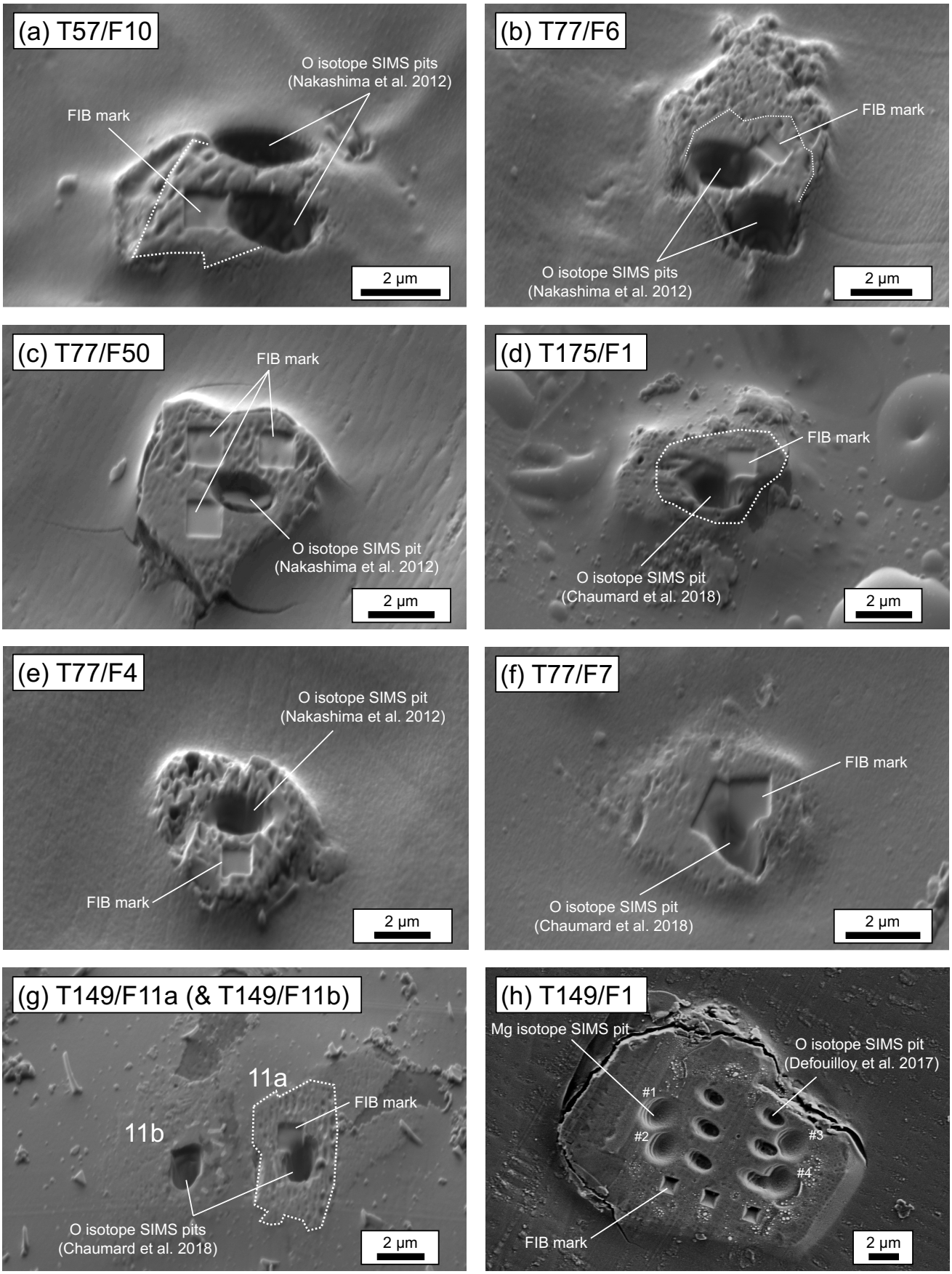
(a) T57/F10
O isotope SIMS pits
(Nakashima et al. 2012)
FIB mark
2 μm
(b) T77/F6
FIB mark
O isotope SIMS pits
(Nakashima et al. 2012)
2 μm
(c) T77/F50
FIB mark
O isotope SIMS pit
(Nakashima et al. 2012)
2 μm
(d) T175/F1
FIB mark
O isotope SIMS pit
(Chaumard et al. 2018)
2 μm
(e) T77/F4
O isotope SIMS pit
(Nakashima et al. 2012)
FIB mark
2 μm
(f) T77/F7
FIB mark
O isotope SIMS pit
(Chaumard et al. 2018)
2 μm
(g) T149/F11a (& T149/F11b)
11a
11b
FIB mark
O isotope SIMS pits
(Chaumard et al. 2018)
2 μm
(h) T149/F1
Mg isotope SIMS pit
O isotope SIMS pit
(Defouilloy et al. 2017)
#1
#2
#3
#4
FIB mark
2 μm

Fig. 3

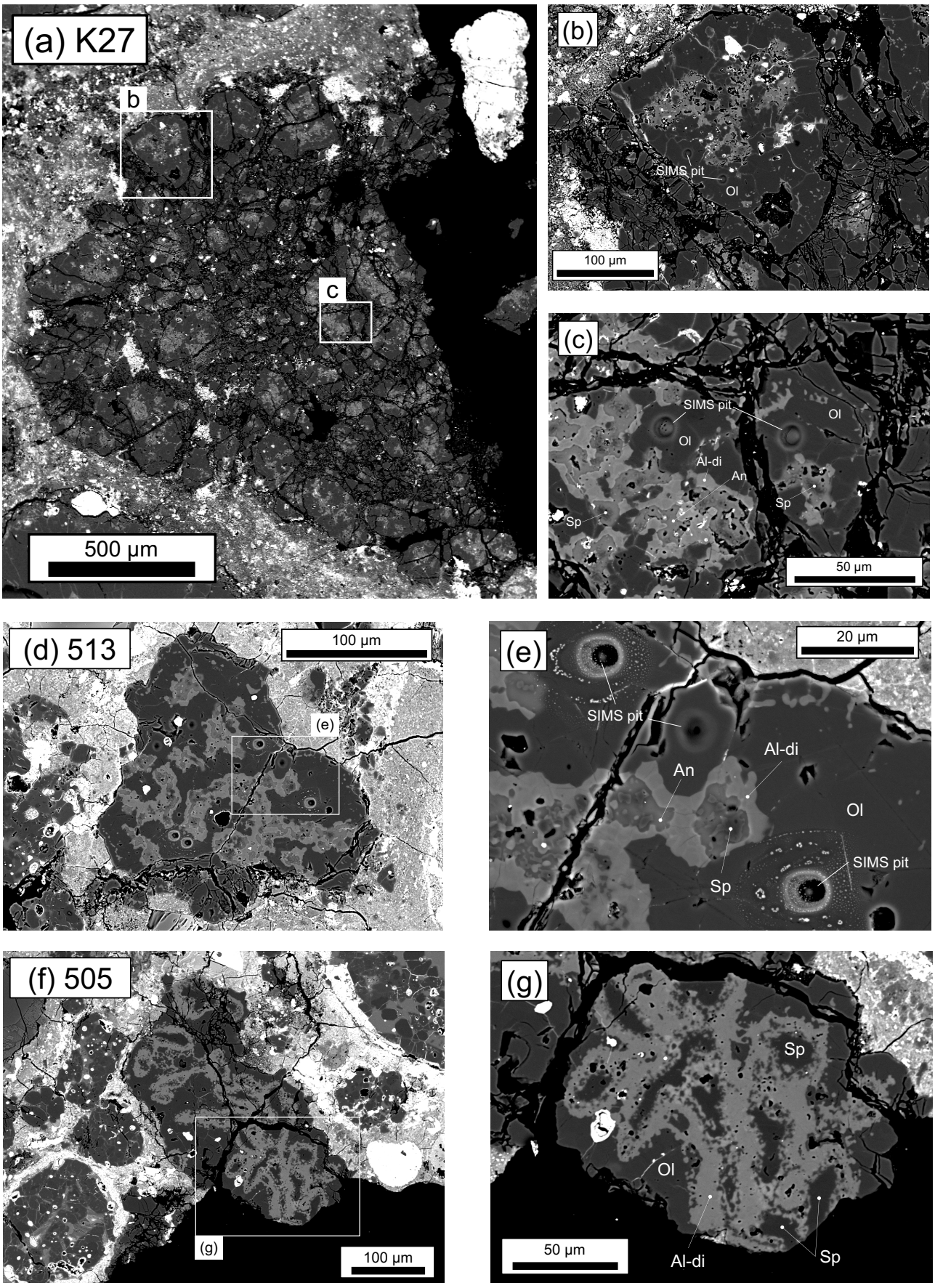
(a) K27
b
c
500 μm
(b)
SIMS pit
Ol
100 μm
(c)
SIMS pit
Ol
Ol
Al-di
An
Sp
Sp
50 μm
(d) 513
100 μm
(e)
(e)
20 μm
SIMS pit
Al-di
An
Ol
Sp
SIMS pit
(f) 505
(g)
100 μm
(g)
Sp
Ol
50 μm
Al-di
Sp

Fig. 4

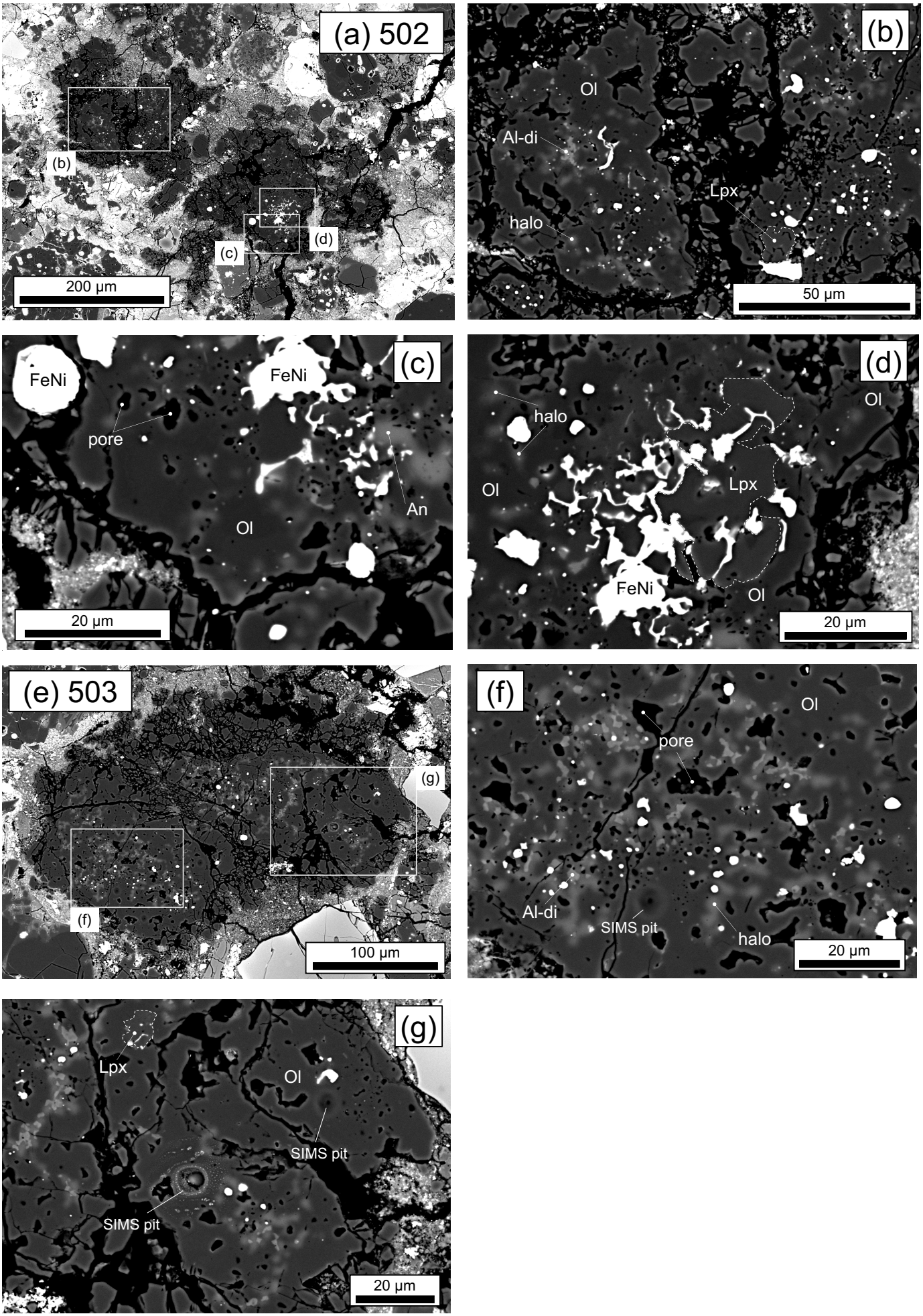
(a) 502
(b)
(c)
(d)
200 μm
(b)
Ol
Al-di
Lpx
halo
50 μm
FeNi
FeNi
(c)
pore
An
Ol
20 μm
halo
(d)
Ol
Ol
Lpx
FeNi
Ol
20 μm
(e) 503
(g)
(f)
100 μm
(f)
Ol
pore
Al-di
SIMS pit
halo
20 μm
(g)
Lpx
Ol
SIMS pit
SIMS pit
20 μm

Fig. 5

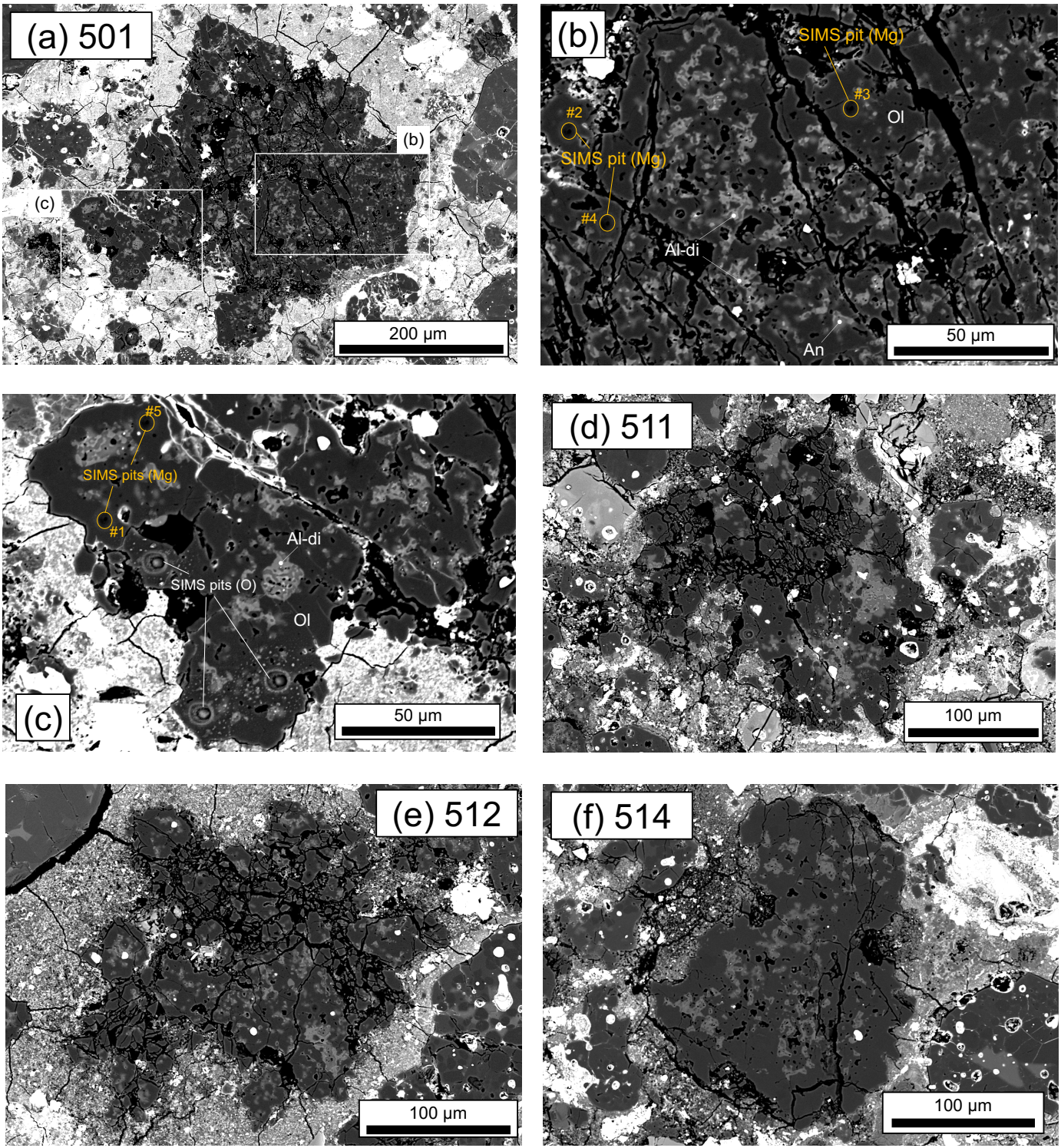
(a) 501
(b)
(c)
200 μm
(b)
SIMS pit (Mg)
#3
#2
Ol
SIMS pit (Mg)
#4
Al-di
An
50 μm
#5
SIMS pits (Mg)
#1
Al-di
SIMS pits (O)
Ol
(c)
50 μm
(d) 511
100 μm
(e) 512
100 μm
(f) 514
100 μm

Fig. 6

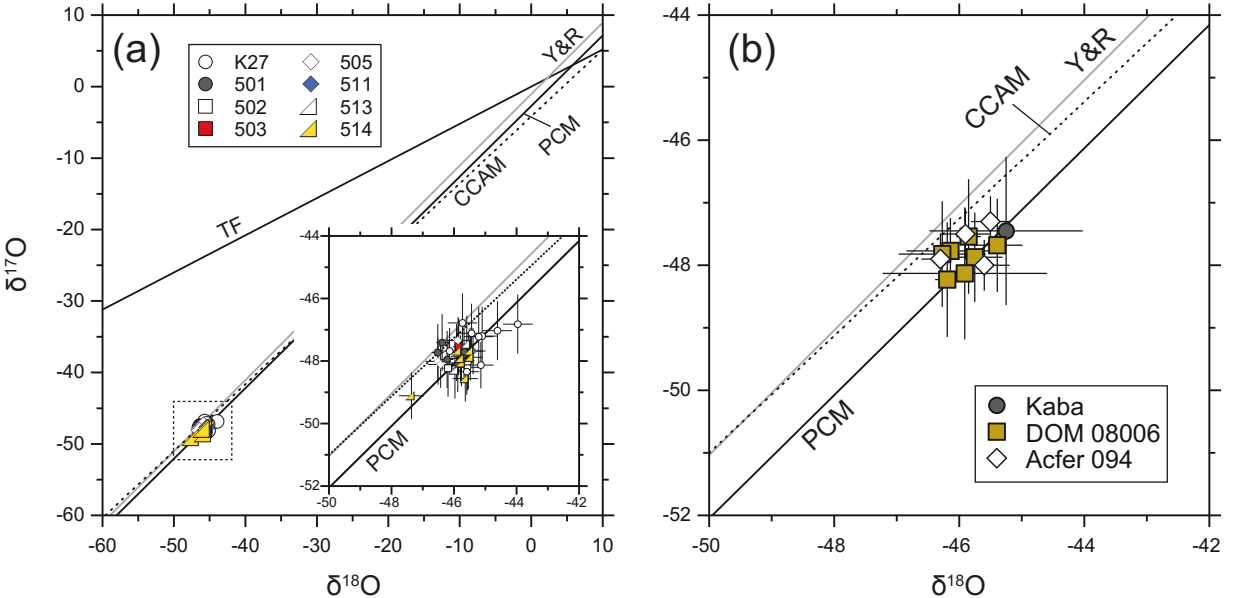
(a)
K27
501
502
503
505
511
513
514
TF
Y&R
CCAM
PCM
δ17O
δ18O
(b)
Kaba
DOM 08006
Acfer 094

Fig. 7

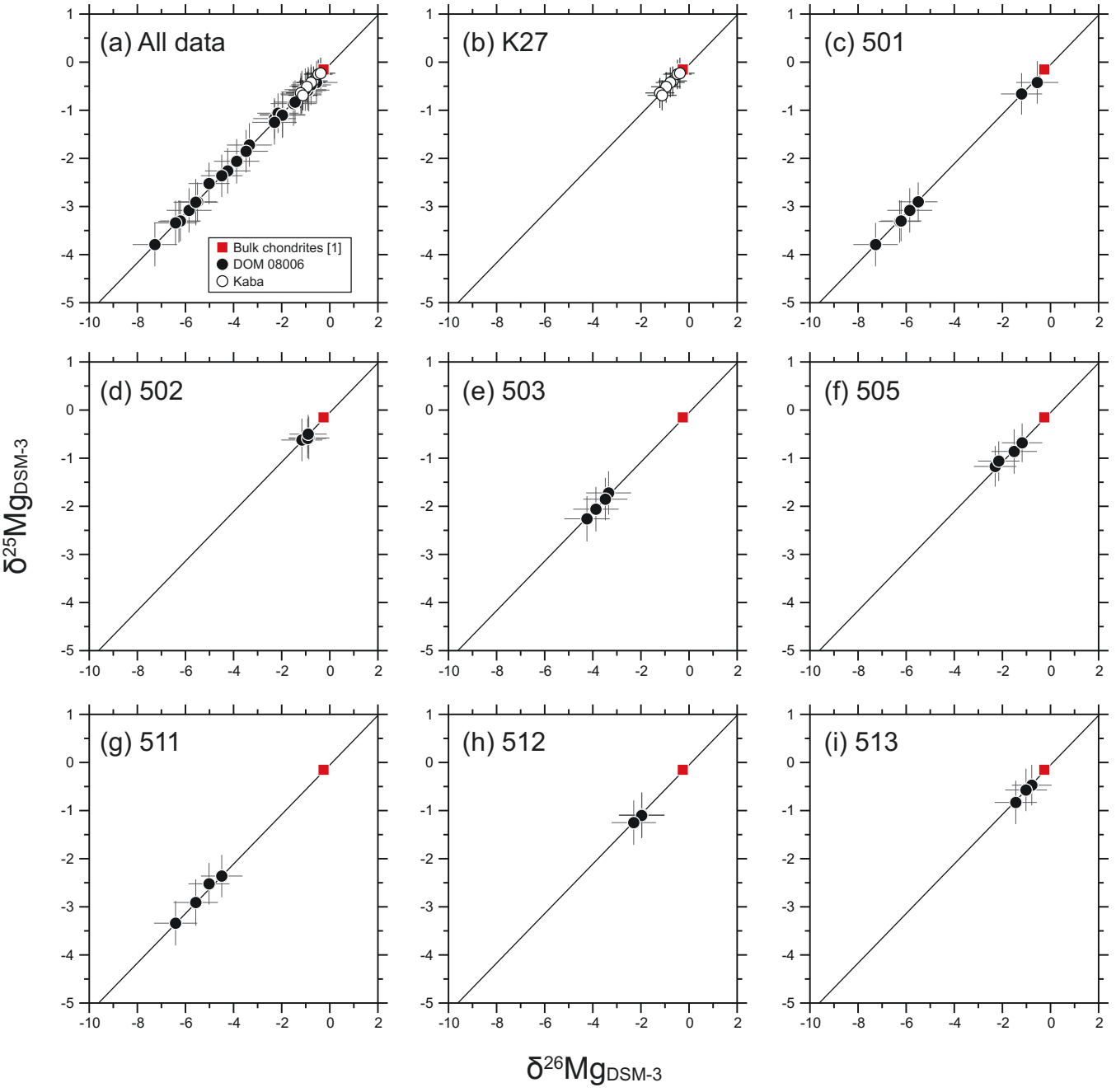
(a) All data
(b) K27
(c) 501
(d) 502
(e) 503
(f) 505
(g) 511
(h) 512
(i) 513
Bulk chondrites [1]
DOM 08006
Kaba
δ25MgDSM-3
δ26MgDSM-3

Fig. 8

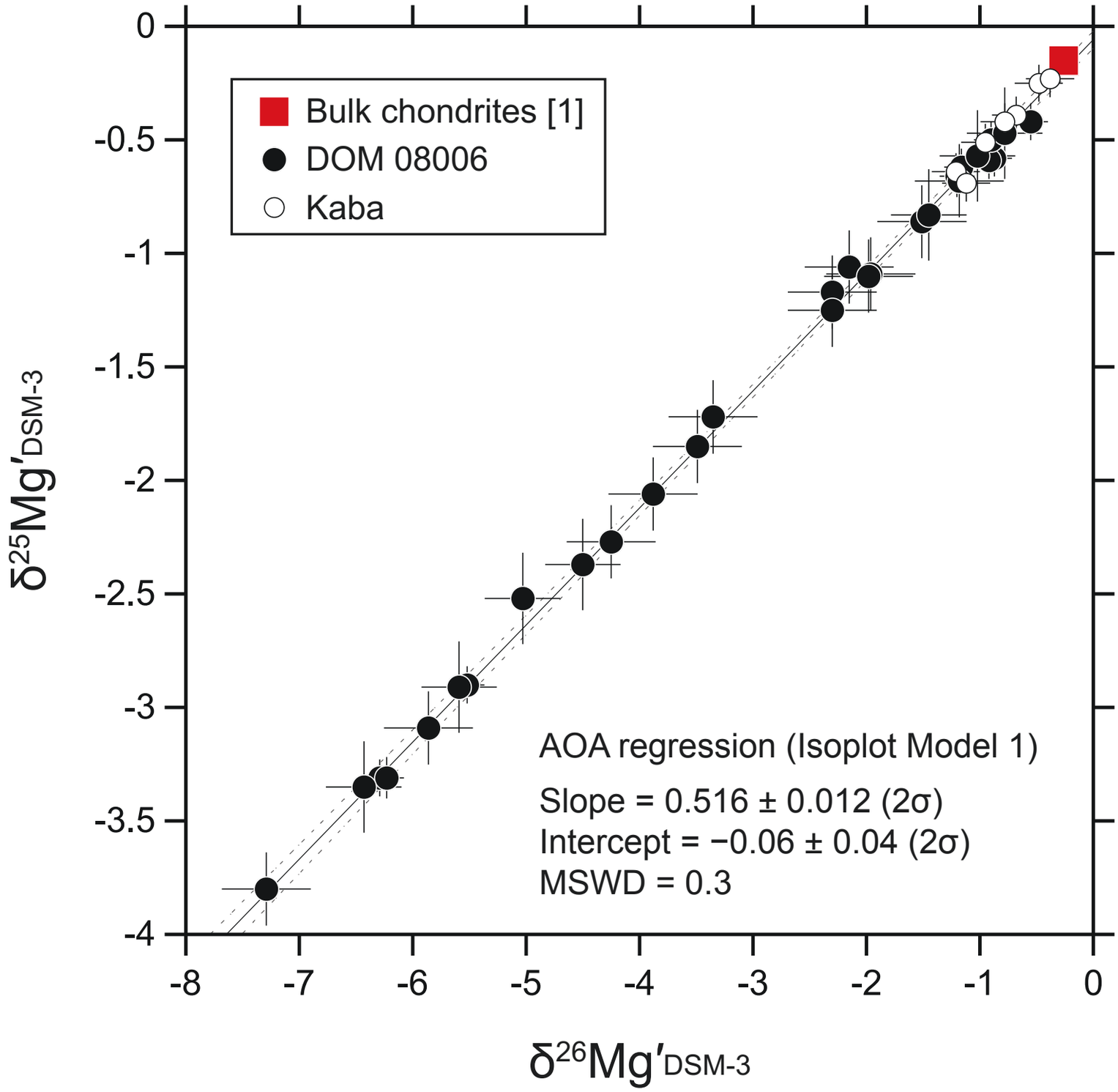
Bulk chondrites [1]
DOM 08006
Kaba
AOA regression (Isoplot Model 1)
Slope = 0.516 ± 0.012 (2σ)
Intercept = −0.06 ± 0.04 (2σ)
MSWD = 0.3
δ25Mg′DSM-3
δ26Mg′DSM-3
0
-0.5
-1
-1.5
-2
-2.5
-3
-3.5
-4
-8
-7
-6
-5
-4
-3
-2
-1
0

Fig. 9

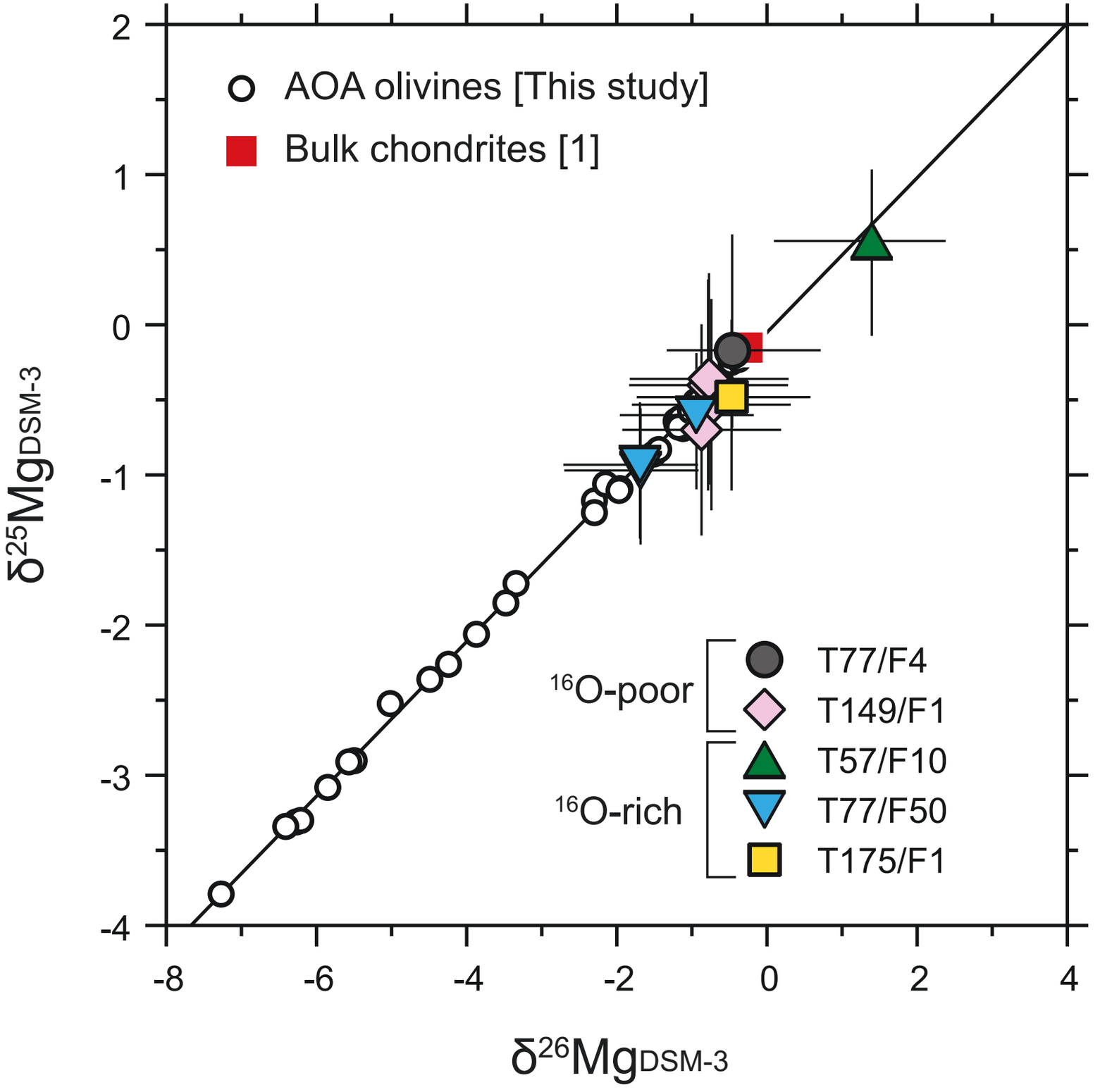
AOA olivines [This study]
Bulk chondrites [1]
$^{16}$O-poor
T77/F4
T149/F1
$^{16}$O-rich
T57/F10
T77/F50
T175/F1
$\delta^{25}Mg_{DSM-3}$
$\delta^{26}Mg_{DSM-3}$
2
1
0
-1
-2
-3
-4
-8
-6
-4
-2
0
2
4

Fig. 10

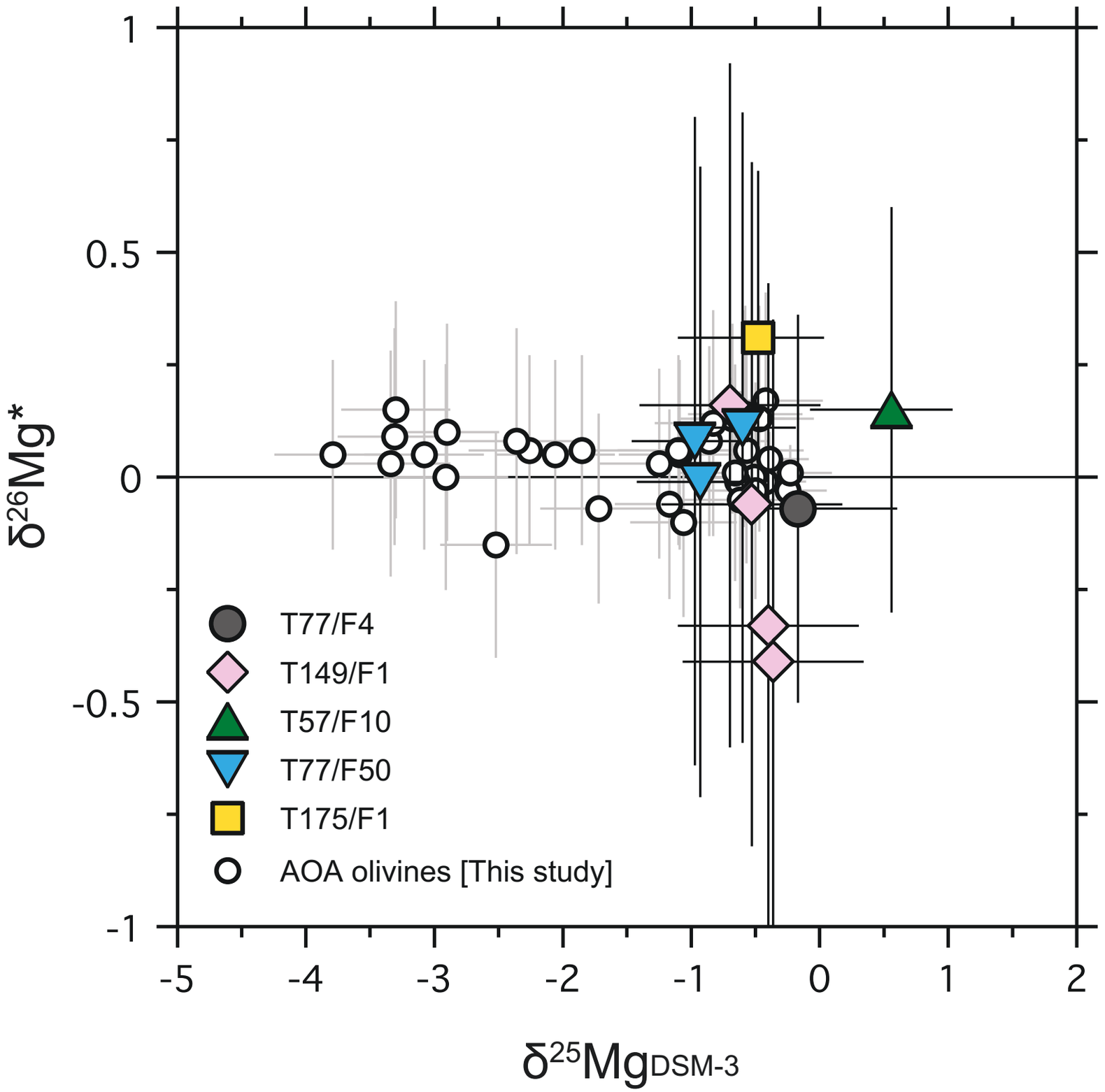
1
0.5
0
-0.5
-1
-5
-4
-3
-2
-1
0
1
2
δ26Mg*
δ25MgDSM-3
T77/F4
T149/F1
T57/F10
T77/F50
T175/F1
AOA olivines [This study]

Fig. 11

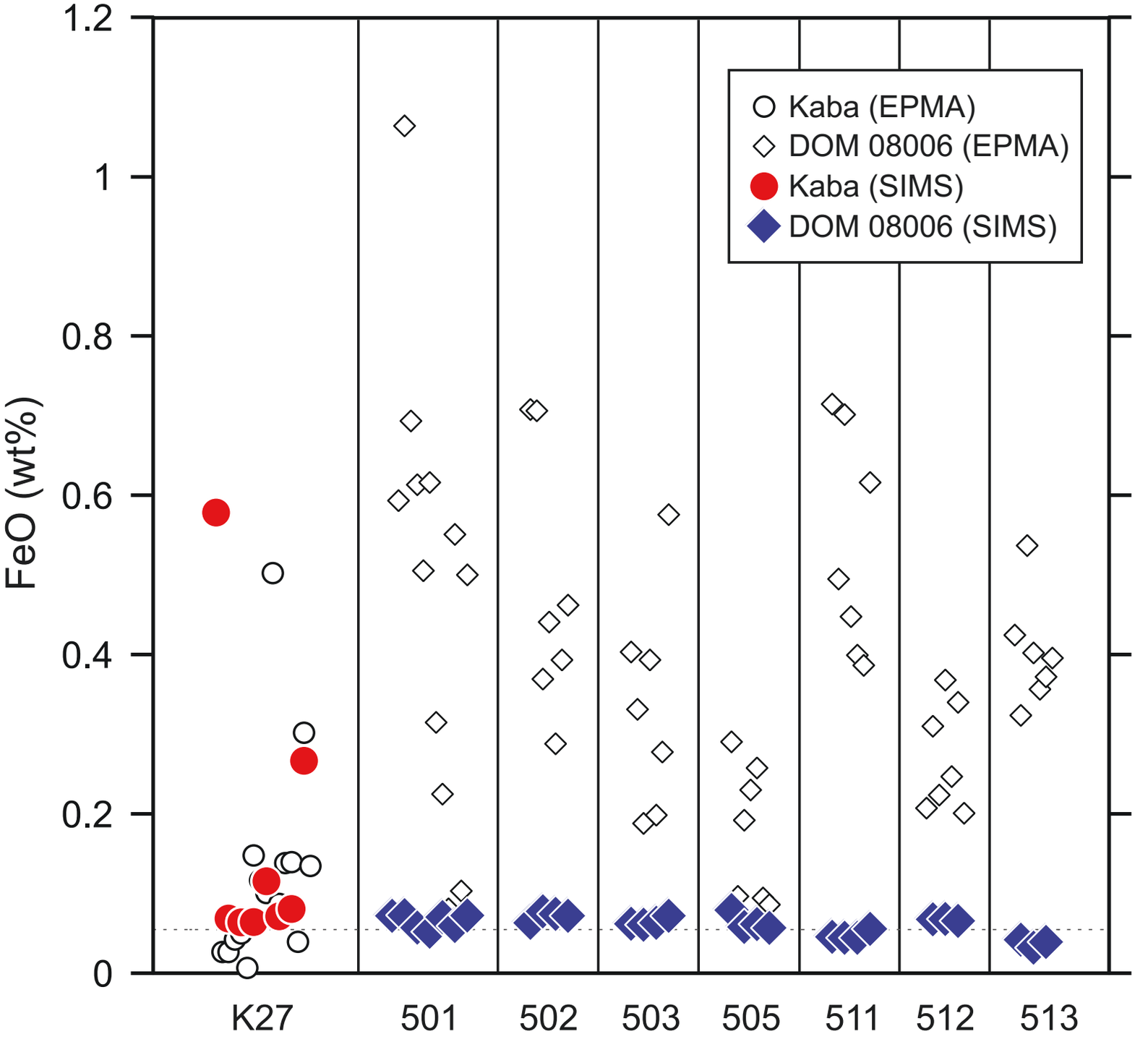
1.2
1
0.8
0.6
0.4
0.2
0
FeO (wt%)
Kaba (EPMA)
DOM 08006 (EPMA)
Kaba (SIMS)
DOM 08006 (SIMS)
K27
501
502
503
505
511
512
513

Fig. 12

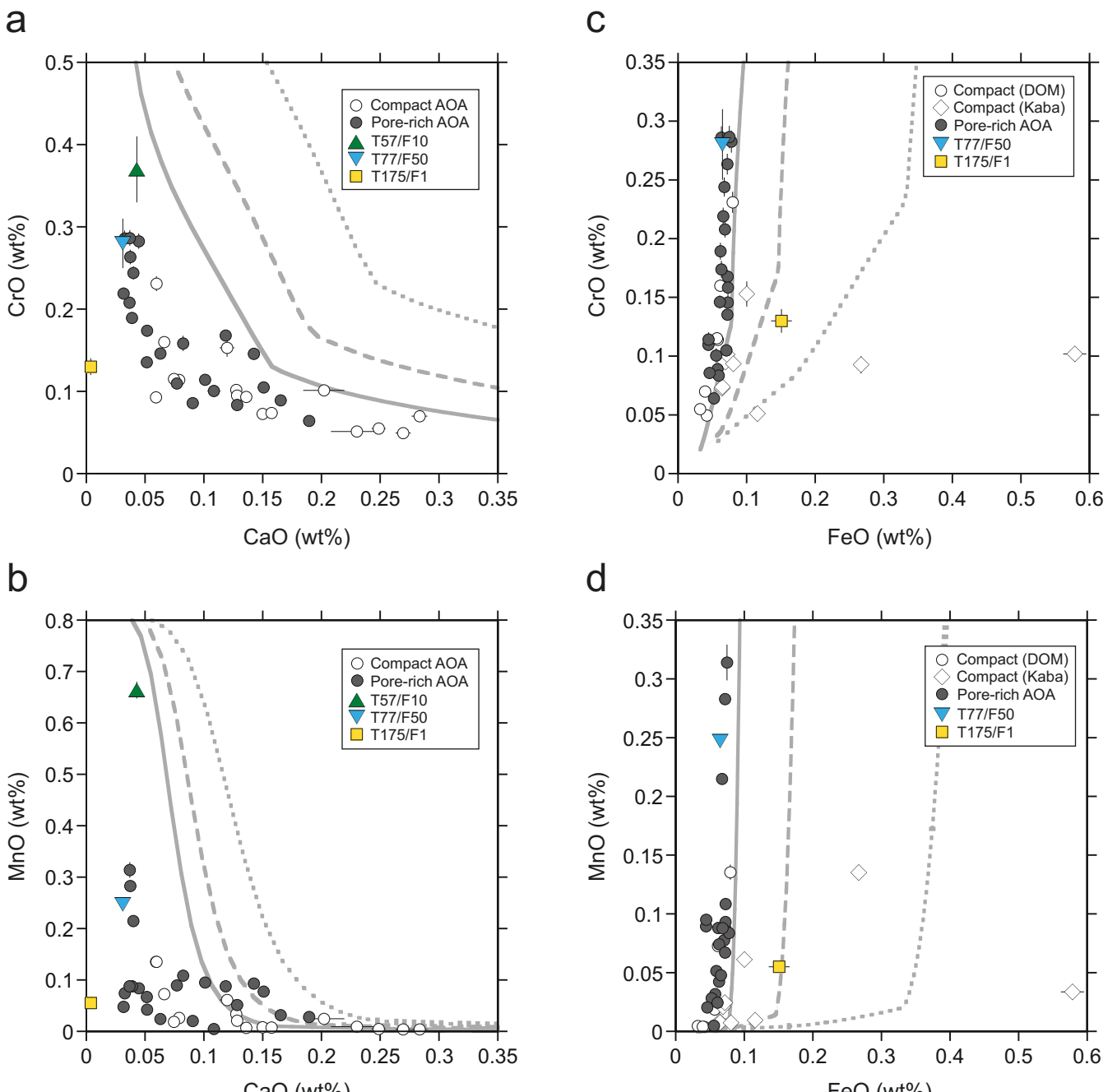
a
c
b
d
Compact AOA
Pore-rich AOA
T57/F10
T77/F50
T175/F1
Compact (DOM)
Compact (Kaba)
CrO (wt%)
MnO (wt%)
CaO (wt%)
FeO (wt%)

Fig. 13

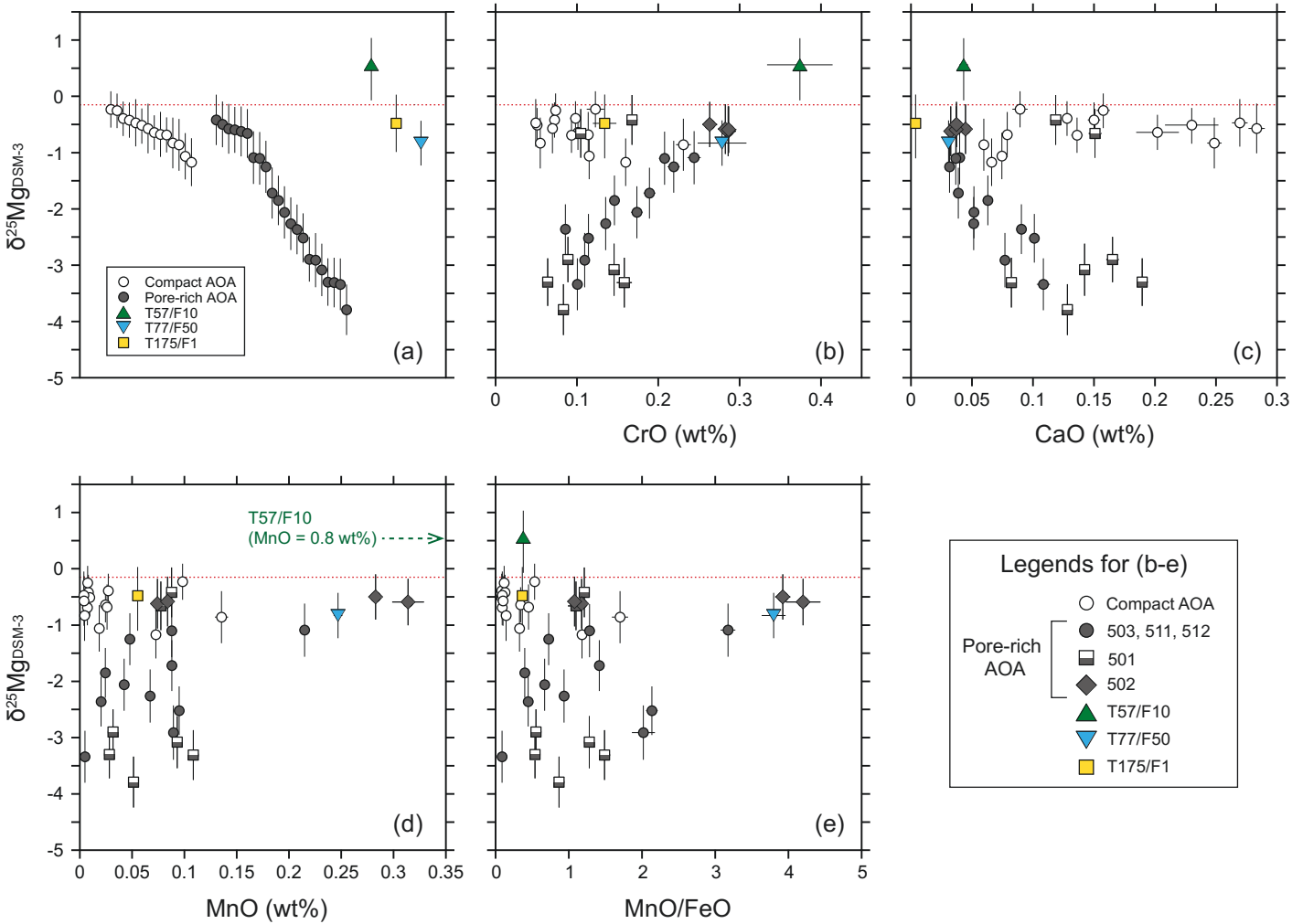
δ25MgDSM-3
Compact AOA
Pore-rich AOA
T57/F10
T77/F50
T175/F1
(a)
(b)
(c)
CrO (wt%)
CaO (wt%)
T57/F10
(MnO = 0.8 wt%)
(d)
(e)
MnO (wt%)
MnO/FeO
Legends for (b-e)
Pore-rich AOA
503, 511, 512
501
502

Fig. 14

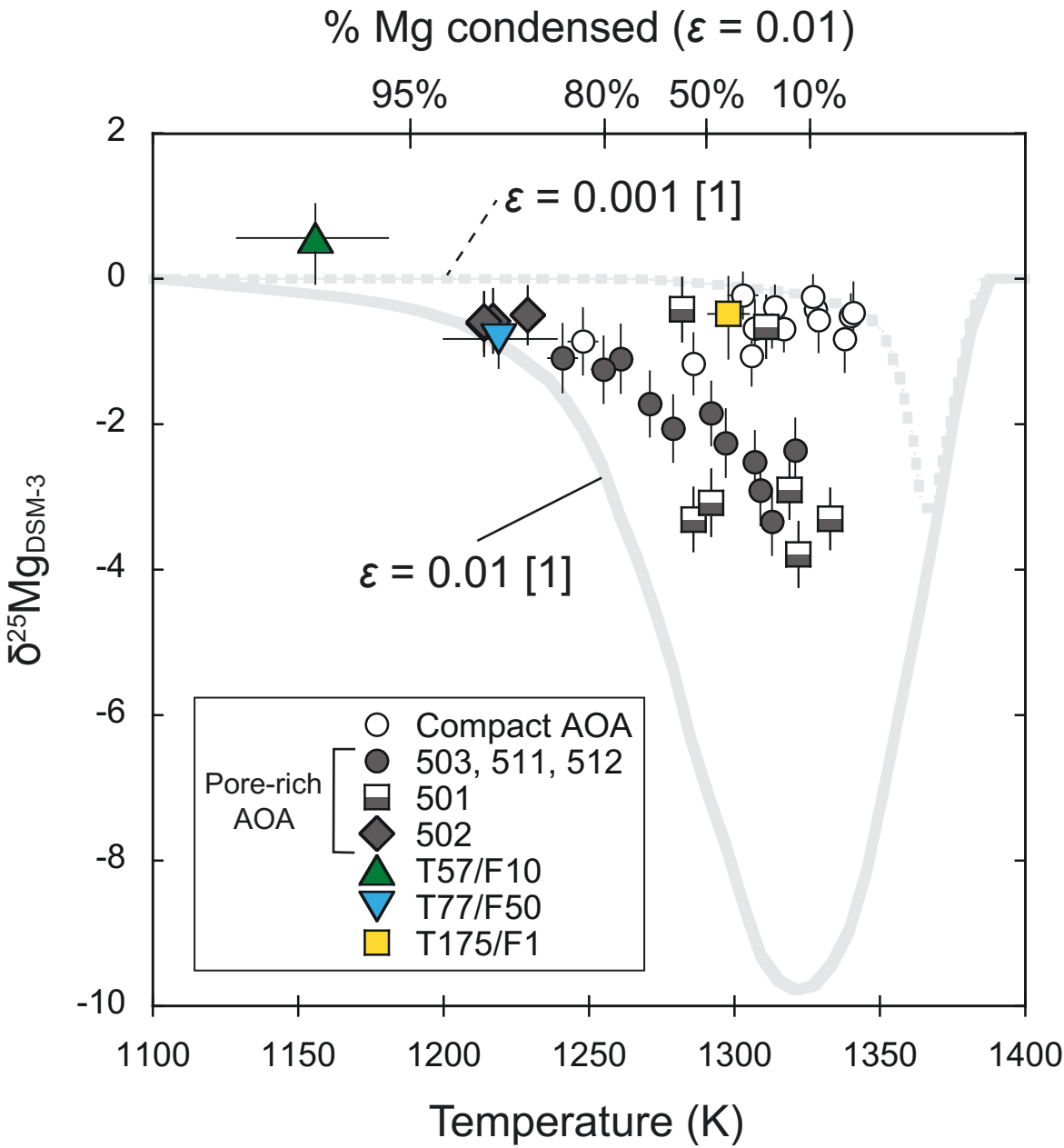
% Mg condensed (ε = 0.01)
95%
80%
50%
10%
ε = 0.001 [1]
ε = 0.01 [1]
δ25MgDSM-3
2
0
-2
-4
-6
-8
-10
1100
1150
1200
1250
1300
1350
1400
Temperature (K)
Pore-rich AOA
Compact AOA
503, 511, 512
501
502
T57/F10
T77/F50
T175/F1